The central parsec of the Milky Way at 3.8 μm

INAUGURAL-DISSERTATION

zur
Erlangung des Doktorgrades
der Mathematisch-Naturwissenschaftlichen Fakultät
der Universität zu Köln

vorgelegt von

Koraljka Mužić
aus Split, Kroatien

Köln 2008

Berichterstatter: Prof. Dr. Andreas Eckart
Prof. Dr. J. Anton Zensus

Tag der letzten mündlichen Prüfung: 23. Juni 2008

Abstract

The central part of the Milky Way is a unique environment where an interplay of different astrophysical phenomena can be studied, starting from the physics of the interstellar medium, stellar physics and star formation, to high energetic processes associated with the accretion onto the supermassive black hole Sgr A*.

In this thesis I focus onto the central parsec of the Milky Way, observed at $\lambda = 3.8\,\mu$m (L'-band) during several epochs from 2002 to 2007. This particular wavelength is interesting because one can observe the (very dense) Galactic stellar nuclear cluster, as well as the thermal component of the interstellar medium which is not visible at shorter near-infrared wavelengths. Our images revealed a high number of very narrow filamentary structures associated with the streamers of gas and dust (called mini-spiral), and sometimes also with stars. We also detected several stellar sources that are barely observable at shorter wavelengths, but well defined in the dust-dominated L'-band. The goal of this thesis was to use multi-epoch observations in order to measure motions of filamentary structures, as well as of those very red stars. The proper motion analysis allows us to come a step further in understanding the real nature of these enigmatic sources. The high-resolution observations were obtained with the NAOS/CONICA Adaptive Optics system at the ESO Very Large Telescope at Paranal, Chile.

The first part of the thesis deals with the narrow dust filaments. The analysis of their morphology and proper motions shows that they are (*i*) probably not due to a projectional effect and (*ii*) are influenced by other forces than just the gravitational force of the central black hole. A possible answer to the question of their nature is that they could be the consequence of an interaction between a fast wind (or an outflow) and the local ISM. I present the best candidates for such an outflow and also discuss the possibility that the outflow is in fact collimated.

In the second part I investigate a small compact cluster of infrared-excess sources IRS 13N located ∼3.5" from Sgr A*, previously proposed to contain young stellar objects. Our proper motion analysis results in the discovery of a new co-moving group at the Galactic Center (GC). Six sources are showing the

same proper motion, meaning that the system is dynamically young. Furthermore, our orbital analysis results in the conclusion that the IRS 13N cluster could not survive a single orbit around Sgr A* without being disrupted. These results speak in favor of IRS 13N stars being the youngest stars ever observed in this environment. The existence of objects younger than 1 Myr would imply that in-situ star formation in the GC and near massive black holes in general is possible. Furthermore, this would also mean that there may exist a mode of star formation in the GC that must not necessarily be related to a star burst and may supply young stars in a more continuous mode.

Zusammenfassung

Das Zentrum der Milchstraße ist eine einzigartige Region, in der das Zusammenspiel verschiedener astrophysikalischer Phänomene untersucht werden kann. Dazu gehören die Physik und Chemie des interstellaren Mediums (ISM), die Physik der Sterne und Sternentstehung sowie die Hochenergieprozesse im Akkretionsfluss auf das supermassive Schwarze Loch Sgr A*.

Der Schwerpunkt dieser Arbeit liegt auf den Beobachtungen des zentralen Parsecs der Milchstraße, die bei $\lambda = 3.8\,\mu$m (L'-band) in den Jahren 2002 bis 2007 durchgeführt wurden. Diese besondere Wellenlänge ist interessant, weil man mit ihr nicht nur den (sehr dichten) zentralen Sternhaufen beobachten kann, sondern auch die thermische Komponente des interstellaren Mediums, die bei kürzeren Nahinfrarot-Wellenlängen nicht sichtbar ist. Unsere Beobachtungen zeigen eine große Anzahl von sehr schmalen Filamenten, die mit Gas- und Staubströmungen (der sogenannten Minispirale) und manchmal mit Sternen assoziiert werden können. Außerdem haben wir einige stellare Quellen detektiert, die kaum bei höheren Frequenzen aber deutlich im staubdominierten L'-band zu sehen sind. Das Ziel dieser Arbeit war es, die Beobachtungen der verschiedenen Jahre zu nutzen, um Eigenbewegungen der Filamente und der sehr roten Sterne zu bestimmen. Die Analyse der Eigenbewegungen erlaubt es uns, die wahre Natur dieser rätselhaften Quellen besser zu verstehen. Die hochaufgelösten Beobachtungen wurden mit dem System für adaptive Optik NAOS/CONICA an ESOs Very Large Telescope in Paranal, Chile, durchgeführt.

Der erste Teil dieser Arbeit beschäftigt sich mit den schmalen Staubfilamenten. Die Analyse ihrer Morphologie und Eigenbewegungen zeigt, dass sie (*i*) wahrscheinlich nicht auf ein Projektionseffekt zurückzuführen sind und dass sie (*ii*) auch von anderen Kräften außer der Gravitationskraft des zentralen Schwarzen Loches beeinflusst werden. Eine mögliche Antwort auf die Frage ihrer Natur könnte sein, dass sie eine Folge einer Wechselwirkung zwischen einem schnellen Wind und des lokalen ISM sind. Ich zeige die besten Kandidaten für solch einen Ausfluss auf und diskutiere die Möglichkeit, dass dieser Ausfluss in Wirklichkeit kollimiert ist.

Im zweiten Teil untersuche ich einen kleinen, kompakten Haufen von

Quellen IRS 13N. Er ist übermäßig hell im Infraroten, in einer Entfernung von ∼3.5" von Sgr A* und soll junge stellare Objekte enthalten. Unsere Analyse der Eigenbewegungen resultierte in der Entdeckung einer neuen sich gemeinsam bewegenden Gruppe im galaktischen Zentrum (GZ). Sechs Quellen zeigen dieselbe Eigenbewegung, was bedeutet, dass das System dynamisch jung ist. Außerdem zeigt unsere Analyse der Orbits, dass IRS 13N keinen einzigen Orbit um Sgr A* überleben könnte ohne auseinandergerissen zu werden. Dies spricht für die Interpretation, dass die IRS 13N Sterne die jüngsten Sterne sind, die jemals in dieser Umgebung beobachtet wurden. Die Existenz von Objekten jünger als 1 Millionen Jahre würde bedeuten, dass in-situ Sternentstehung im GZ und in der Nähe von massiven Schwarzen Löchern möglich ist. Zusätzlich würde dies auch heissen, dass ein Sternentstehungsmodus im GZ existieren könnte, der nicht notwendigerweise mit einem plötzlichen Ausbruch von Sternenstehung in Verbindung steht, sonder junge Sterne in einem kontinuierlichen Modus erzeugt.

Contents

Chapter 1

Astrophysical background

1.1 Introduction to infrared astronomy

The infrared domain in whole is often conventionally divided into three subdomains: near- (0.75 – 5 μm), mid- (5 – 25 μm) and far-infrared (25 – 350 μm). Technologically speaking, the proper infrared starts at about 1 μm, where most of the detectors used in the optical cease to be useful. At wavelengths longer than 350 μm radio techniques, such as superheterodyne receivers become preferred to the infrared approach, and the region from 0.35 mm to 1 is referred to as the sub-millimeter region.

Radiation from an astronomical source can be approximated by a blackbody distribution. From the Wien's displacement law

$$\lambda_{max} T = 0.29 cmK \tag{1.1}$$

one can see that by observing at longer and longer wavelengths the most prominent observed objects generally have lower and lower temperatures. The continuous spectrum of the Sun peaks at $\lambda \approx 5800$ K, corresponding to ~ 0.5 μm, close to the human eye's maximum sensitivity in bright sunlight. The coolest normal stars (~ 3000 K) peak at about 1 μm. Warm dust, with typical temperatures of few hundred Kelvins peaks in the mid-infrared, at about 10 μm. Also, at this wavelength the blackbody radiation from ~ 300 K terrestrial sources

reaches its maximum. Detectors at these wavelengths quickly become saturated with background photons and therefore must often be read out several tens of times per second. However, as we will see in chapter 3 the influence of the background already becomes important in the near-infrared, longwards of $\lambda \sim 3\,\mu$m.

Infrared astronomy from ground-based sites is confined to several atmospheric windows of good transmission. At several wavelengths between 1 and $25\,\mu$m, the atmosphere is opaque, with the most transparent atmospheric windows being near $2.2\,\mu$m, $3.7\,\mu$m and $10.5\,\mu$m. Between 30 and $400\,\mu$m the atmosphere is almost completely opaque, making the far-infrared domain one of the most challenging observational domains. FIR infrared measurements are mostly carried out from airborne telescopes or satellites.

1.2 Interstellar dust - an infrared view

Dust plays an important role in observational astronomy. Dust particles influence the thermal, dynamical, chemical and ionization states of the interstellar and intergalactic medium. A significant fraction of the interstellar heavy elements is in the form of dust so that the dust ties up most of the important atomic species that provide cooling. In addition to cooling, dust provides the heating through electrons ejected photoelectrically from grains. Therefore, the temperature and the dynamical evolution of the gas component of the interstellar medium (ISM) is directly dependent on dust properties in all kinds of astrophysical environments. Chemical composition of dust particles in our Galaxy has been deduced from various types of observations: extinction, polarization and scattering of starlight, infrared continuum emission, different spectral features attributed to dust, interstellar depletion of elements etc. The studies have been carried out on different kinds of objects, such as star forming regions, HII regions, diffuse and dense clouds, circumstellar shells of stars, meteorites etc. All these studies have shown that dust particles are mainly made of crystalline and amorphous silicates and of carbonaceous material in some form.

The absorption characteristics of dust grains are very wavelength dependent, so that blue or ultraviolet photons are blocked and scattered much more

easily than longer wavelength photons. This gives rise to extinction and reddening of sources that are behind a dust clump or intrinsically dust-embedded. As we will see, the effects of extinction are much less severe in the infrared than in the optical, and this fact makes infrared observations extremely important in the Galactic Center science. Clouds of gas and dust that lie between us and the center of our Galaxy cause the extinction in the optical of $A_V \approx 30$ mag, making it impossible to conduct any observations in this wavelength regime. However, the extinction in the NIR K-band is dramatically lower - A_K is about 3 mag.

This section will deal with some important properties of interstellar dust grains. However, the topics concerning the chemical composition of grains, dust formation and destruction, and polarization of light by dust are not of the direct concern for this thesis and therefore will be omitted. I will discuss some important observational properties of dust, with the bias toward the infrared wavelength regime. Most of the following text has been compiled from various sources in the literature: Mathis (1990); Glass (1999); Tielens (2005); Dopita & Sutherland (2003); Draine (2003); Krishna Swamy (2005).

1.2.1 Extinction by dust and infrared extinction law

Much of our knowledge of interstellar dust is based on studies of the wavelength-dependence of the extinction (often referred to as reddening). The wavelength-dependence strongly constrains the grain size distribution, and spectral features reveal the chemical composition. The dimensionless quantity

$$R_V \equiv \frac{A_V}{A_B - A_V} \tag{1.2}$$

is a common measure of the slope of the extinction curve in the optical region. $A_B - A_V$ is the color excess in the UBV photometric system. Very large grains would produce gray extinction with $R_V \to \infty$. Rayleigh scattering ($A_\lambda \propto \lambda^{-4}$) would produce very steep extinction with $R_V \approx 1.2$. R_V is known to vary from one line of sight to another, from lower values of about 2.1 to values as large as 5.8. In practice, for the diffuse ISM, R_V is assumed to be constant with a value around 3.1.
In the infrared, the normalized extinction curve $A_\lambda / A_{\lambda 0}$ (using the extinction

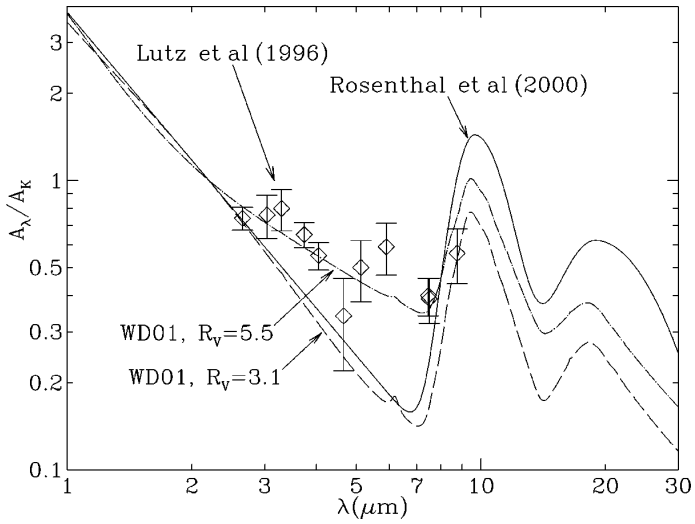

Figure 1.1: *Infrared extinction, relative to extinction in the K-band, inferred by Rosenthal et al. (2000) for dust in the OMC-1 molecular cloud and by Lutz et al. (1996) for dust towards Sgr A*, and as calculated for the Weingartner & Draine (2001) grain models for $R_V = 3.1$ and $R_V = 5.5$. The 6.2 μm absorption feature in the WD01 grain models is due to PAHs. Figure from Draine (2003).*

in some band centered at $\lambda 0$ for normalization) depends only on λ and R_V. At shorter wavelengths, namely in the optical and the UV, this dependence is more complicated. Furthermore, empirical infrared extinction curves in Milky Way diffuse clouds show relatively little variation, and for wavelengths between 0.7 μm and 8 μm the normalized extinction curve is almost independent of R_V. Between $\sim$0.9 μm and $\sim$5 μm the continuous extinction curve can be approximated by a power-law $A_\lambda \propto \lambda^{-\beta}$, with $\beta \approx 1.61 - 1.80$ (e.g. Rieke & Lebofsky 1985; Draine 1989; Whittet et al. 1993). Draine (1989), in the review on extinction by interstellar dust at infrared wavelengths, give a power-law $A_\lambda \propto \lambda^{-1.75}$ valid up to $\lambda \approx 6\mu$m. In the region 5 – 8 μm , however, there is no common agreement in the extinction law (see Fig. 1.1). Using ISO observations of hydrogen recombination lines, Lutz et al. (1996) find that the extinction towards Sgr A* does not decline with increasing the wavelength in the 4 – 8 μm region. This is confirmed by Viehmann et al. (2005): based on $L - M$ colors of a large sample of stars in the central 70"×70" they found that $A_L \approx A_M$. On the other hand, studies of the H_2 ro-vibrational lines in the OMC show that the extinction declines with increasing λ to a minimum at $\sim$6.5 μm (Rosenthal et al. 2000).

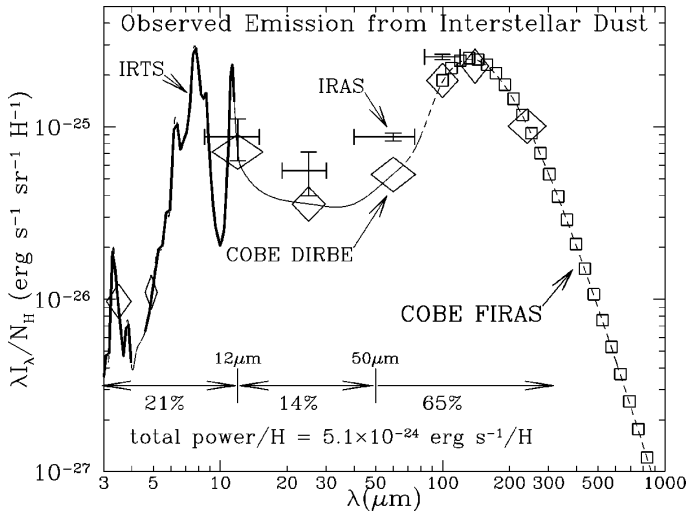

Figure 1.2: *Observed emissivity of diffuse interstellar dust per H nucleon (Draine 2003).*

1.2.2 Infrared emission by dust

Dust grains absorb the incident visible and UV radiation and re-emit the energy in the infrared. The intensity of the emitted radiation provides clues to the nature, temperature and distribution of the dust. However, the analysis of the observational data is fairly complicated, mainly because of large variations of grain size and its composition. The heating of dust grains by starlight photons is quantized and stochastic and thus the temperature of dust is time dependent. As can be seen in Fig. 1.3, for large grains ($a \gtrsim 200\,\text{Å}$; where a denotes the size of a grain) the temperature can be approximated as being steady. Small grains ($a \lesssim 50\,\text{Å}$), however, undergo very large temperature excursions. A small grain will heat up after the absorption of a photon, and then quickly cool. Most of the infrared power radiated occurs during brief intervals following photon arrivals. In order to calculate the time-averaged spectrum for small grains, one must calculate the energy distribution function dP/dE for grains of a particular size, where dP is the probability that a grain will have a vibrational energy in interval (E, $E + dE$). One of the methods used to obtain dP/dE is by means of Monte-Carlo simulations.

The infrared emission from interstellar dust can be measured, and then used

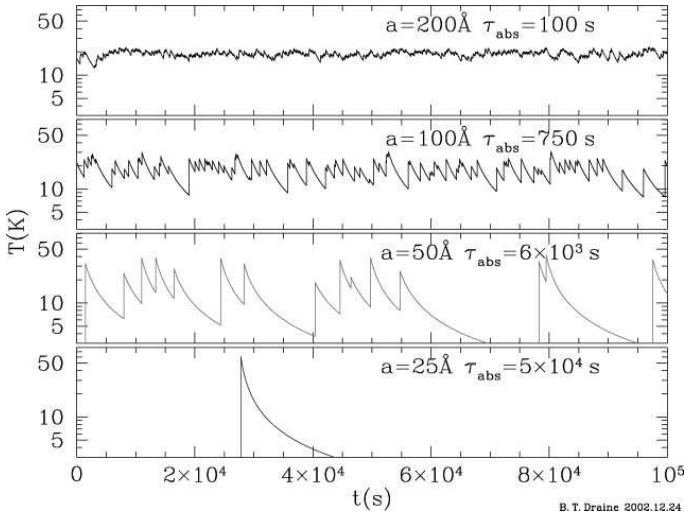

Figure 1.3: *A day in the life of four carbonaceous grains, heated by the local interstellar radiation field. τ_{abs} is the mean time between photon absorptions (Draine 2003).*

for fitting an appropriate dust model that is able to reproduce the observed intensity and spectrum. The galactic latitudes $|b| \gtrsim 20^o$ are particulary suitable for such observations since there we have good estimates for the intensity of the starlight heating the dust, and the 21 cm emission provides accurate gas column densities. The latter gives, for an assumed dust-to-gas ratio, the column density of dust. Although the surface brightness of the infrared emission is low, it has been detected by IRAS and COBE after averaging over large areas of sky (Fig. 1.2). The emission in range $3.0-4.6\,\mu$m and $4.5-11.3\,\mu$m was measured by IRTS satellite at $b \approx 0$ and normalized to agree with COBE DIRBE photometry. In the dust model (Draine 2003) shown in Fig. 1.2 approximately 20% of the absorbed energy is re-radiated at $\lambda < 12\,\mu$m by polycyclic aromatic hydrocarbon (PAH) molecules. The emission at $\lambda > 50\,\mu$m is an emission from $a \gtrsim 0.01\,\mu$m grains that are maintained at a nearly steady temperature $\sim$15–20K. These grains account for approximately two thirds of the radiated infrared power and therefore it is evident that the far-infrared emission is an excellent tracer of interstellar dust. The emission in the NIR/MIR tells us that grain population must contain enough small-size grains in order to account for approximately one third of the overall dust emission. Also, the dust grains that give rise to NIR and MIR emission must be warm - peak wavelength of the

Planck function shows that this radiation must come from grains with temperatures of hundreds of Kelvin. If a dust grain is large enough to have an almost continuous density of energy states, it will radiate a continuum rather than emission bands. This again puts some constraints on the grain size to 5 – 50 Åand represents the main contribution to the $3-30\,\mu$m continuum emission.

Continuum radiation from dust arises from two mechanisms: (*i*) fluorescence, giving rise to a red continuum; and (*ii*) thermal radiation (Mathis 1990). The simplest interpretation of the red fluorescent emission is that it is excited by by a strong UV flux incident upon hydrogenated carbon particles (amorphous or PAHs), thereby producing both the fluorescent red emission and the H_2 fluorescence. In presence of a strong radiation field the carbon particles can be altered and H_2 dissociated. As already mentioned above, thermal radiation is observed in following wavelength regimes: (1) 1–60 μm, following the transient heating of a small grain by a single UV photon, (2) $\lambda > 100\,\mu$m, where the energy is reprocessed by steady-state emission of larger grains, and (3) between these ranges, where a contribution from both processes is present.

Apart from the continuum emission, diffuse dust produces strong unidentified infrared emission bands (UIBs) in the 3.3 – 11.3 m range. The strongest UIBs are at 3.3, 6.2, 7.7, 8.6 and 11.3 μm. These wavelengths all closely correspond to the C-H or C-C bond vibrations in aromatic (benzene-ring) structures. The simplest substances that can produce UIBs are PAHs, but also some less ordered configurations of carbon and hydrogen are also able to account for these emission features.

1.2.3 Dust emission associated with young stars

Conditions for dust grain formation are realized in a variety of astronomical environments: in the wind around cool giant stars, either on Giant Branch or on the Asymptotic Giant Branch (AGB) phase, in supermassive stars undergoing massive mass-loss episodes (such as η Car), in nova envelopes and supernova ejecta. However, circumstellar emission is not limited only to highly evolved stars. It has also been observed in various kinds of young stellar objects (YSOs), pre-main sequence objects as Herbig Ae/Be and T-Tauri stars and main sequence stars such as Vega etc. The pronounced infrared excess of spectra of young star arises from dust grains relatively close to the stellar surface, rather than from the reddening due to grains along the line sight. According to the Wien's displacement law (Eq. 1.1), thermal radiation that peaks near 10 μm has an associate temperature near 300 K. The typical infrared excess does not display a pure blackbody spectrum, indicating a significant range in temperatures (Stahler & Palla 2004). Moreover, these temperatures are high enough that the dust must be relatively close to the star. Young stellar objects (YSO) are usually classified using criteria based on the slope of their SED. The infrared spectral index α_{IR} is defined as:

$$\alpha_{IR} \equiv \frac{dlog(\lambda F_\lambda)}{dlog\lambda} \tag{1.3}$$

The derivative is conventionally evaluated by numerically differencing the flux between 2.2 μm and 10 μm. The classification is the following (Stahler & Palla 2004):

- $\alpha_{IR} > 0$ Class I objects; objects generally associated with dense cores (as seen by NH_3 emission)
- -1.5 $< \alpha_{IR} <$ 0 Class II objects
- $\alpha_{IR} <$ -1.5 Class III objects

Finally, a Class 0 has been added to incorporate sources so deeply embedded in the dust that can only be detected at far-infrared and millimeter wavelengths. This classification schema roughly reflects evolutionary sequence. It is believed that most deeply embedded Class 0 sources evolve towards Class I stage dissipating their circumstellar envelopes.

1.3 Interstellar shocks

In this section I present basic physical processes that lead to formation of interstellar shocks and discuss the possibilities to observe them in the infrared. More detailed approach to the topic can be found in review articles by Draine & McKee (1993) and McKee & Hollenbach (1980), as well as in the books on interstellar medium by Tielens (2005) and Dopita & Sutherland (2003). This section is mainly based on the above mentioned literature.

A shock wave is an irreversible, pressure driven fluid-dynamical disturbance. It occurs whenever material moves at supersonic velocities in the surrounding medium. Since a disturbance propagates faster than the characteristic signal velocity, the medium upstream of the shock cannot dynamically respond to the incoming material until it arrives. The shock will then compress, heat and accelerate the medium. Shocks are an ubiquitous feature in the ISM: they can be driven by supernova explosions, stellar winds, the pressure of photo-ionized gas and collisions between fast-moving clumps of interstellar gas.

Shock structure
An interstellar shock can be approximately divided in three regions:
(*i*) the radiative precursor which may heat, ionize and dissociate the upstream gas;
(*ii*) the shock front in which elastic collisions or plasma instabilities excite the translational degrees of freedom in the gas and produce the increase in the temperature, density and entropy of the gas; and
(*iii*) the post-shock relaxation layer in which the gas cools and relaxes to its final composition. The precursor and the post-shock relaxation layer have nearly Maxwellian particle distribution and are described by the usual hydrodynamic equations.

Types of shocks
Two types of shocks occur in the interstellar medium: (1) J-shocks - fast shocks (J is for jump), where gas is so suddenly stopped and heated that radiative and non-radiative relaxation is insignificant. The shock front is much thinner than the post-shock relaxation layer and the pre- and post-shock conditions (density, temperature and velocity) change abruptly (Fig. 1.4). (2) C-shocks (C for continuous) - weak shocks in a magnetized medium with a low degree of

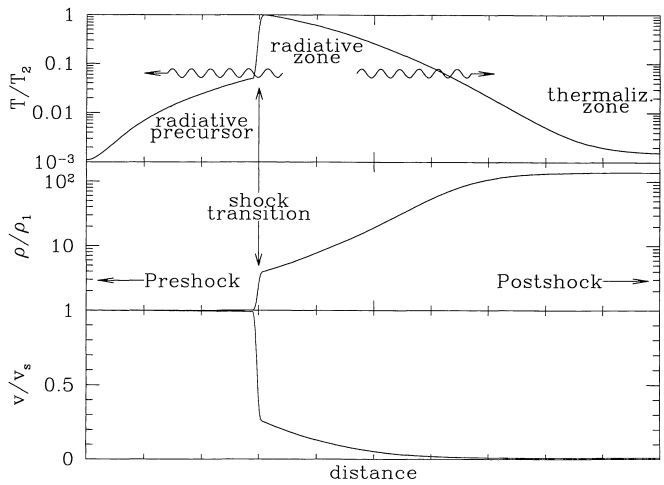

Figure 1.4: *Schematic structure of a J-shock showing temperature, density and velocity normalized to the maximum temperature reached just behind the shock (T_m), the pre-shock density (ρ_0), and the shock velocity (v_s) (Draine & McKee 1993).*

ionization. The shock work is done by trace ions drifting through the predominantly neutral medium. The shock front in this case is much thicker than the cooling length scale and the temperature is set by the balance between heating and cooling. Under these conditions, the hydrodynamic flow variables change continuously.

The shock can be either J- or C-shock, depending on the gas density, the ionization fraction, the chemical composition, the magnetic field strength and the shock velocity. In general, C-shocks are occur in gas with a low degree of ionization, a high density and molecular fraction, at least a moderate magnetic field, and low shock velocties.

1.3.1 Fast shock physics

The fluid motion is governed by the conservation of mass, momentum and energy, together with Maxwell's equations. First we assume the case of the single fluid, meaning that all the components in a flow (e.g. atoms, ions and

electrons) move at the common velocity. Since the thickness of the shock front is generally small compared to hydrodynamic length scales, the hydrodynamic equations in the vicinity of the shock front reduce to their one-dimensional, steady-state form in a coordinate system moving together with the shock. For example, the continuity equation (which describes the conservation of mass), written in its original form

$$\frac{\partial \rho}{\partial t} + \bigtriangledown \cdot (\rho \mathbf{v}) = 0, \tag{1.4}$$

reduces to

$$\frac{d}{dz}(\rho v_{\parallel}) = 0 \tag{1.5}$$

where z is the distance normal to the shock front and $v_{\parallel} \equiv v_z$.

Integration of the hydrodynamical equations across the shock front gives the *Rankine-Hugoniot relations*, or jump conditions. For a hydromagnetic shock, Maxwell's equations are needed as well. The jump conditions can be written in a form sufficiently general so that they apply inside the shock as well as across it. However, when applied outside the shock front where viscous effects, relative drifts between different particle species and heat conduction are negligible, the jump conditions are further simplified.
The Rankine-Hugoniot relations are the following:

$$\left[\rho v_{\parallel}\right] = 0 \tag{1.6}$$

$$\left[\rho v_{\parallel}^2 + P + \frac{1}{8\pi} B_{\perp}^2\right] = 0 \tag{1.7}$$

$$\left[\rho v_{\parallel} \mathbf{v}_{\perp} - \frac{1}{4\pi} B_{\parallel} \mathbf{B}_{\perp}\right] = 0 \tag{1.8}$$

$$\left[v_{\parallel}\left(\frac{1}{2}\rho v^2 + P + u\right) + \frac{1}{4\pi} B_{\perp}^2 v_{\parallel} - B_{\parallel} \mathbf{B}_{\perp} \cdot \mathbf{v}_{\perp}) + F_{\parallel}\right] = 0 \tag{1.9}$$

$$\left[v_{\parallel} \mathbf{B}_{\perp} - B_{\parallel} \mathbf{v}_{\perp}\right] = 0 \tag{1.10}$$

$$\left[B_{\parallel}\right] = 0 \tag{1.11}$$

The notation $[f] \equiv f(x_2)$–$f(x_1)$, where subscripts 1 and 2 denote points upstream and downstream the shock transition. The coordinate system is such

that the shock velocity is normal to the shock front. F is the flux of electromagnetic wave energy, and u is the internal energy density. The jump conditions simplify considerably if $B = 0$ and if the internal energy is related to the pressure by $u = \mathrm{p}/(\gamma$ - 1), where γ is the adiabatic index assumed to be constant across the shock. The first equation is the mass conservation, the second and third are momentum conservation, the fourth is energy conservation, and the last two follow from Maxwell's equations and the flux-freezing condition

$$\mathbf{E} + \mathbf{v}_c \times \mathbf{B}/c = 0 \tag{1.12}$$

Here $\mathbf{v}_c$ represents the mean velocity of the charged component of the plasma. The latter condition is applied only *outside* the shock front, but it ensures that flux is conserved *across* the shock irrespective of the processes that occur in the front itself.

The Rankine-Hugoniot equations are generalized to include chemical and radiative processes in the shock. Unfortunately, they do not form a closed set of equations: the net amount of energy radiated in the shock front F is undetermined, and the jump in u depends on jumps in concentrations, which is also undetermined (Hollenbach & McKee 1979). If a significant number of molecules survives the shock, then the change in ratio of specific heats, γ, is also unknown. Therefore some simplifying assumptions must be made in order to obtain a solution. For fast shocks (i.e. the one where flow variables change suddenly), the suitable approximation is that no inelastic processes (radiation, ionization, etc.) occur in the shock front itself, so that $[F]_s = [\gamma]_s = 0$, where the subscript s implies that the jump is to be evaluated from just ahead of to just behind the shock front. This approximation is reasonably good in most astrophysical applications.

In presence of the magnetic field $\mathbf{B}$, the angle characterizing the shock is that between the magnetic field and the shock normal, $\theta = \tan^{-1}(B_\perp/B_\parallel)$. For a general case where $0 < \theta < \pi/2$ and $\gamma = 5/3$, the magnetic field becomes unimportant for sufficiently fast shocks: For $M_A > 6$ all the terms in jump conditions involving the magnetic field can be omitted without affecting the values of the downstream density and temperature by more than 30% (Draine & McKee 1993). M_A is the Alfvén Mach number, the ratio between the shock velocity and the Alfvén speed $v_A \equiv \mathrm{B}/(4\pi\rho)^{1/2}$, while M is the ordinary Mach number. For $\gamma > 1$, the compression ratio and post-shock temperature have

limiting values which are independent of the field:

$$\lim_{M,M_A\to\infty} \frac{\rho_2}{\rho_1} = \frac{\gamma+1}{\gamma-1} \tag{1.13}$$

$$\lim_{M,M_A\to\infty} T_2 = \frac{2(\gamma-1}{(\gamma+1)^2}\frac{\mu v_s^2}{k}, \tag{1.14}$$

where μ is the mean mass per particle just behind the shock front. Since the shock is stationary in the frame of reference used here, $v_0 \equiv v_s$. For $\gamma = 5/3$, the full solution for the post-shock flow variables in the strong shock limit is:

$$\begin{aligned} v_2 &= v_s/4 \\ \rho_2 &= 4\rho_1 \\ P_2 &= 3\rho_1 v_s^2/4 \\ T_2 &= \frac{3}{16}\frac{\mu v_s^2}{k} \\ &\sim 1.38\times10^5 v_{100}^2 K \text{ (fully ionized gas)} \\ &\sim 2.90\times10^5 v_{100}^2 K \text{ (neutral atomic gas)} \\ &\sim 5.30\times10^5 v_{100}^2 K \text{ (molecular gas),} \end{aligned} \tag{1.15}$$

where v_{100} is the shock velocity normalized to $100\,\mathrm{km\,s^{-1}}$.

Shocks that are not strong exhibit more complex behaviour. In contrast to fast shocks, the role of the magnetic field is crucial and therefore a full magnetohydrodynamic treatment of C-shocks is essential.

1.3.2 The shock spectrum and shock diagnostics

In contrast to the shock front, the post-shock relaxation layer is dominated by inelastic collisions and by the emission and absorption of radiation. In many cases – especially for very fast shocks – the cooling time behind the shock exceeds the age of the shock. The radiation emitted from the shocked gas does not affect the dynamics and therefore such shocks are called non-radiative. In non-radiative shocks there is no clear distinction between the relaxation layer and the overall flow behind the shock. On the other hand, in radiative shocks

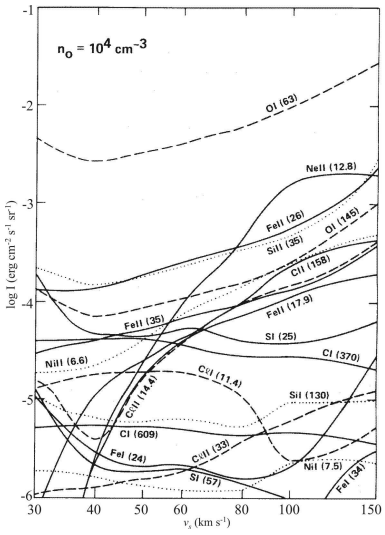

Figure 1.5: *Atomic fine-structure infrared line intensities emergent normal to the J-shock as a function of shock velocity, for a pre-shock density n_0=10^4 cm^{-3}. Figure from Hollenbach & McKee (1989).*

the relaxation layer is well defined. The criterion separating radiative from non-radiative shocks can be expressed in terms of the cooling column density $N_{cool} = n_0 v_s t_{cool}$, where t_{cool} is the cooling time behind the shock front. A radiative shock is the one in which the column density of the shocked gas N_{tot} is greater than N_{cool}. Shocks are non-radiative because v_s is large or t_{cool} is small (as in young supernova remnants), n_0 is low (as in stellar winds in early type stars) or the shocked gas is convected away (as in the case of the shocks associated with the interaction between the solar wind and the ISM). Since non-radiative shocks lack cooling zones, the optical and UV line emission is excited close to the shock front. The visible spectrum of a non-radiative shock will be dominated by hydrogen emission lines. On the other hand, the low temperatures in radiative shocks favour the emission of strong forbidden lines such as [OI], [OII], [OIII], [NI], [NII], and [SII]. Most of these transitions occur in the optical; shock-ionized regions can then be distinguished from photo-ionized gas (HII regions) through the ratio of forbidden lines to Hβ. In the UV, radiative shocks produce strong resonance lines of neutral and ionized C, N and O.

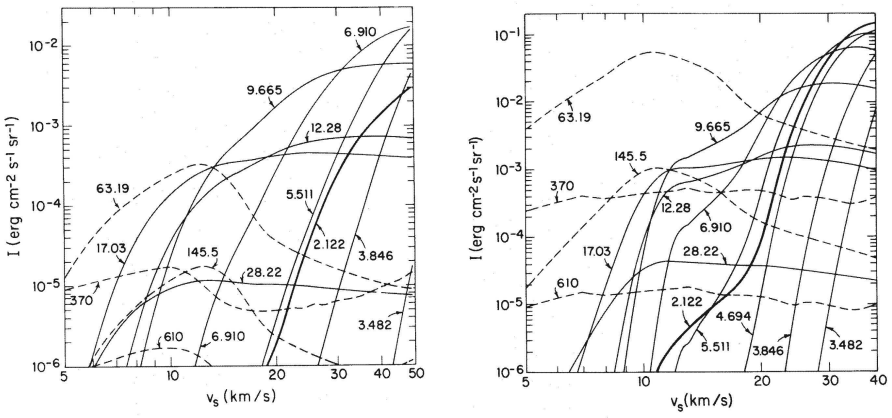

Figure 1.6: *Line intensities calculated for C-shocks propagating into molecular gas. Left: $n_H = 10^4\ cm^{-3}$, $B = 10\,\mu G$ and ionization fraction $x_e = 10^{-7}$. Right: $n_H = 10^6\ cm^{-3}$, $B = 1\,mG$ and $x_e = 10^{-8}$. The atomic fine-structure lines of [OII] (63 and 146 μm) and [CII] (370 and 610 μm) are indicated by dashed lines. The solid lines are the pure rotational lines of H_2 and the ro-vibrational transition 1-0 S(1) (2.12 μm). Figure from Draine et al. (1983).*

Infrared emission

In the near-infrared, shocked gas can be distinguished from PDRs through the presence of a strong [SI] 25μm line and the absence of PAH emission characteristic of gas illuminated by FUV photons. Another good discriminant for shocked vs photo-heated gas is the [OI] 63 μm to [CII] 158 μm ratio. Furthermore, a high [FeII] 1.644 μm to Br γ ratio is a good indicator of shocks, because most of the Fe in photoionized regions is FeIII and FeIV, whereas FeII is an important coolant for shock heated gas as it cools below 10^4 K.

Another very important tracer of shocked gas in the infrared is molecular hydrogen. H_2 can be observed through its ro-vibrational levels, both in J- and C-shocks. J-type shock will completely dissociate the molecules so that the H_2 emission is coming from the warm recombination plateau in the post-shock region (Lee et al. 2005). In a C-type shock, because of the influence of the magnetic field, the H_2 dissociation speed limit is much higher. However, H_2 line emission can also be produced in PDRs. Here the ratios between different H_2 emission lines can help in distinguishing between two excitation mechanisms. For example, a good tracer of shocks is a 2-1 S(1)(2.2477 μm)/1-

0 S(1)(2.1218 μm) ratio, observed within a K-band window. Another information on the nature of the NIR hydrogen lines can be obtained by investigation of their line widths (Lee et al. 2005): in PDRs the line profiles are very narrow; in J-type shocks lines are still narrow, but the peak is shifted from the velocity of the pre-shock gas to that of the shock; C-type shock will produce broader lines which peak at the velocity of the pre-shock gas and extend up to the shock velocity. The dominant infrared emission lines of J- and C-shocks are shown in figures 1.5 and 1.6, respectively. The relative intensities of the rotational lines of molecular hydrogen (e.g. 0-0 S(1) and S(9) at 17.03 and 4.694 μm) are good velocity indicators for moderately fast shocks.

Chapter 2

Introduction to the Galactic Center

At a distance of $\sim 8\,\mathrm{kpc}$ (Reid 1993; Eisenhauer et al. 2003, 2005) the center of the Milky Way shows a broad variety of structures. It is an unique environment where an interplay of different astrophysical phenomena can be studied, starting from the physics of the interstellar medium, stellar physics and star formation, to high energetic processes associated with the accretion onto the super-massive black hole Sgr A*. An extensive work of several groups over the past 10 years has resulted in convincing evidence for a $3.6\times10^{6}\mathrm{M}_{\odot}$black hole at the position of Sgr A* (Eckart & Genzel 1996; Genzel et al. 1997; Ghez et al. 1998; Genzel et al. 2000, 2003; Ghez et al. 2000; Eckart et al. 2002; Schödel et al. 2003; Ghez et al. 2005). The super-massive black hole (SMBH) is not the object of the direct concern of this thesis. However, all the processes that take place in the cental parsecs of the Galaxy are directly or indirectly connected to the central object and thus Sgr A* plays a crucial role while trying to understand the physics of this rather complicated region.

The radius of influence r_h of the black hole is defined as a radius within which a mass contained in stars is two times the mass of the black hole. This radius determines the region where the black hole dominates the dynamics. For Sgr A* nuclear stellar cluster, Schödel et al. (2007) estimate $r_h \approx (1.1\text{-}2.2)\,\mathrm{pc} \approx (30\text{-}60)$".

I this section I give an overview of the structures observed within central few parsecs of the Galaxy, that are relevant for this thesis. A schematic overview of the entire region is given in Fig. 2.5. The spatial orientations of various planar structures at the GC are shown in Fig. 2.2.

2.1 Galactic Center interstellar medium

The central parsec of the Galaxy is surrounded by a dense disk or torus-like structure, the so-called circum nuclear disk (CND). The CND is consisted of molecular gas (Güsten et al. 1987; Jackson et al. 1993; Wright et al. 2001; Hernstein & Ho 2002) and warm dust (Zylka et al. 1995) that orbits the center. The molecular medium is extremely clumpy, with a volume filling factor of ∼10%. From a comparison of different gas tracers Jackson et al. (1993) deduce a range of gas densities present in the CND from 10^4 to $\geq 10^6\,\mathrm{cm}^{-3}$. A large interclump velocity dispersion ($\geq 40\,\mathrm{km\,s}^{-1}$) indicates frequent interclump collisions and shocks and reflects importance of tidal disruption and turbulence in the overall dynamics of the disk. The CND exhibits a sharp inner edge at ∼1.5 – 3.0 pc from the center within which we find a short-lived central cavity of much lower mean gas density. The interstellar medium (ISM) component in the central cavity is represented by the so-called mini-spiral, mainly composed of ionized gas and dust. The name mini-spiral reflects the projected appearance, rather than a real spiral structure of the gas streamers. Vollmer & Duschl (2000) have re-examined the mini-spiral gas dynamics traced by the [Ne II] line emission (λ=12.8μm; Lacy et al. 1991) and the H92α radio emission data (Roberts & Goss 1993) and discuss the kinematic structure of the inner ∼ 3×4 pc of the Galaxy. They derive a three-dimensional kinematic model of gas streams that describes the bulk gas motion in three different planes. Most of the material is located in a main plane which is connected to the inner edge of the CND. Paumard et al. (2004) observed the mini-spiral with integral field spectroscopy at 2.06μm (He I) and 2.16μm (Br γ) covering roughly 40"× 40" around Sgr A*. They analyze the kinematics of the mini-spiral and describe nine distinguishable structures. Of the special importance for this work are streamers called Northern Arm and Bar, both indicated in Fig. 2.5.

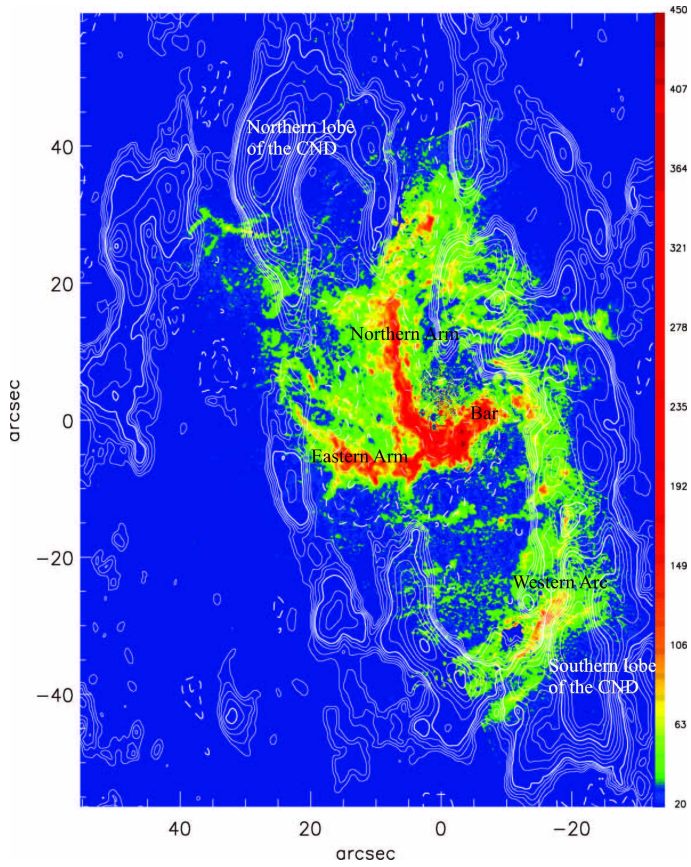

Figure 2.1: *Integrated HCN emission map in contours overlaid upon the color-scale HST NICMOS image of extinction-corrected Paα emission in the Galactic Center region. HCN emission is coming primarily from the CND and Paα from the ionized mini-spiral. Coordinates show the offset from Sgr A*. Emission contours (solid lines) are at (0.2, 0.4, 0.6, 0.8, 1.0, 1.5, 2.0, 2.5, 3.0, 3.5, 4.0, 4.5, 5.0, 6.0)$\times 6.765\,Jy\,beam^{-1}\,km\,s^{-1}$, while the absorption contours (dashed lines) are at (-0.5, -1.0, -2.5, -5.0, -10.0)$\times 6.765\,Jy\,beam^{-1}\,km\,s^{-1}$. The color-scale units, indicated on the right, are $10^{-16}\,ergs\,cm^{-2}s^{-1}pixel^{-1}$. Image adopted from Christopher et al. (2005).*

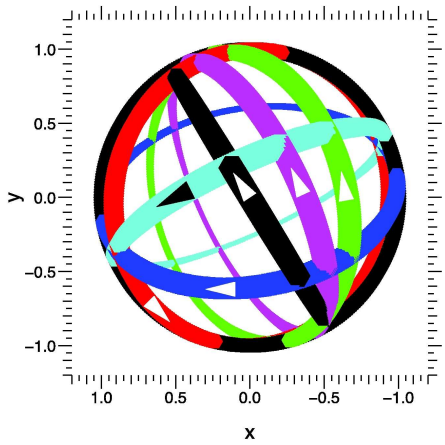

Figure 2.2: *Various planar structures in the GC: the Galaxy and sky (black), the clockwise (blue) and counterclockwise (red) stellar systems, the Northern Arm (green) and the Bar (cyan) of the mini-spiral and the CND (magenta). Each plane is represented by one ring. The thickness of the ring figures the proximity to the observer. Arrows indicate the direction of rotation. Figure from Paumard et al. (2006).*

2.2 Stellar populations

Outside the central 0.5 pc the stars at the center of the Milky Way are distributed according to a near-isothermal cluster. From the projected radius of 100" to approximately 10" (~ 0.4 pc) the stellar volume density follows the power law of $\propto r^{-2}$. The stellar population is a mixture of the old bulge population and intermediate-age and young stars from more recent star formation epochs.

Inside the central 10" the number density flattens to $\propto r^{-1.4}$ and the luminosity of the region becomes dominated by the cluster of massive young stars (Blum et al. 1995; Krabbe et al. 1995; Genzel et al. 1996, 2000; Eckart et al. 1999; Clénet et al. 2001; Paumard et al. 2006). This population consists of blue supergiants, identified as OB stars, Wolf-Rayet (WR) stars and luminous blue variables (LBV). This population is often referred to as helium stars, because of the strong and broad helium emission lines observed in their spectra. Najarro et al. (1997) performed infrared spectroscopy of the brightest members of this

population and showed that the width of emission lines and their clear P-Cygni profiles are caused by extremely strong stellar winds characterized by the mass loss rate of $\dot{M} \sim 5$ – $80 \times 10^{-5} \mathrm{M}_{\odot}\,\mathrm{yr}^{-1}$ and velocities $\mathrm{v}_{\infty} \sim 300$ – $1000\,\mathrm{kms}^{-1}$. For a comparison, the mass loss rate of our Sun is only $10^{-14} \mathrm{M}_{\odot}\,\mathrm{yr}^{-1}$. In total, the He-stars supply $\sim 3 \times 10^{-3} \mathrm{M}_{\odot}\,\mathrm{yr}^{-1}$ of gas in the form of stellar winds to the center.

Young stars in the central 0.4 pc exhibit another interesting property: they are dynamically unrelaxed. The stars are organized in one or two disk-like structures (Genzel et al. 2003; Levin & Beloborodov 2003; Paumard et al. 2006). There is a strong evidence for the existence of the disk of the clockwise-rotating stars (CWS), populated by 36 – 40 bright young stars. The orbital parameters of this disk[1] are $i = 127^{o} \pm 2^{o}$ and $\Omega = 99 \pm 2^{o}$, as given by Paumard et al. (2006). The second disk (CCWS) is thought to contain stars rotating in the counter-clockwise direction, but its existence is still a matter of debate. This disk is not that well defined as the first one and is less populated (12 – 17 stars), with the larger opening angle than the CWS disk. With the orbital parameters $i = 24^{o} \pm 4^{o}$ and $\Omega = 167 \pm 7^{o}$, CCWS lies at large angle with respect to CWS. See Fig. 2.2 for the spatial orientation of the two disks.

Inside ~ 0.04 pc the stellar population changes again. A cluster of faint blue B-type stars, known as the "S-cluster", is observed there. They orbit around Sgr A* on randomly distributed orbits, with no correlation to the orientation of either of the two disks. Proper motions of the S-stars are high, some of them higher than $1000\,\mathrm{kms}^{-1}$. Thanks to intensive observational campaigns during the last 15 years, significant parts of their orbits have been mapped. In case of the star S2, with the orbital period of ~ 15 yr, the full orbit has been covered. It is the analysis of these orbits that gave the most convincing evidence that the central object is extremely compact and indeed a black hole (Schödel et al. 2002, 2003; Ghez et al. 2005; Eisenhauer et al. 2005). At the same time, it provided a precise determination of the Sgr A* mass and distance.

[1] for more detailed explanation of the orbital parameters see section 5.2.2

2.2.1 IRS 13

IRS 13 is located ∼3.5" south-west from Sgr A*, at the edge of the mini-cavity. It was observed as a bright single spot in the early works of Rieke et al. (1989) and Allen & Sanders (1986). Already at that time, from analyzing the SEDs of several GC objects, Rieke et al. (1989) note that there are separate luminosity sources in the core of IRS 13. A year later, Simon et al. (1990) resolve IRS 13 into two sources separated by ∼1.2", named 13E and 13W. These observations, based on lunar occultation of the GC, achieved for the first time a sub-arcsecond resolution in the K-band. Afterwards, the advance of speckle interferometry and imaging in the second half of the nineties brought extremely important improvements in the near-infrared observations of the GC and allowed Ott et al. (1999) to resolve IRS 13E into two components. With the start of the era of Adaptive Optics (AO) at largest ground-based telescopes present, the source was further resolved into more and more components (Paumard et al. 2001; Clénet et al. 2001). Maillard et al. (2004), based on HST/NICMOS data report seven sources within a projected diameter of ∼0.5". All stars were identified as massive stars of different types, including Wolf-Rayet (WR) and O-type stars. At the same time, based on L-band data of the GC Eckart et al. (2004) report the existence of another group of sources located only half an arcsecond north from IRS 13E. These sources, named IRS 13N, are very red and barely visible in the K-band. An important and puzzling property of both IRS 13E and IRS 13N is that they contain co-moving stars; however, as we will show later in this work, the two clusters move at almost 90^o with respect to eachother. Both IRS 13E and IRS 13N clusters (or associations of sources) will be further discussed in chapter 5. This introduction is given in order to better understand the issues of star formation scenarios at the GC.

2.3 Star formation at the GC

As we have already seen, a central parsec of the Galaxy is a host to a surprisingly high number of young stars. The He I stars are, according to different authors, classified as post-main-sequence OB stars, Wolf-Rayet (WR), Ofpe/WN9 and luminous blue variables (LBV). All these types of stars are massive and short-lived. S-stars are less massive, but still quite young B-type

stars (Eisenhauer et al. 2005; Ghez et al. 2005). Observations show that massive star formation has occurred at or close to the GC within the last few million years, interpreted as a modest starburst that took place 3-7 Myr ago (Krabbe et al. 1995). The same authors point out that the presence of about 10 intermediate-mass AGB stars means that at least one other star formation event took place within the past 100 Myr.

Which physical process is responsible for the observed young population in the central parsec of the Galaxy? The standard picture of star formation via the cloud collapse is not applicable in this special environment: the minimal proto-stellar cloud density that can resist the SMBH strong tide is extremely high compared to typical values encountered in star forming molecular clouds elsewhere in the Galaxy ($n \lesssim 10^4 cm^{-3}$). For $r \lesssim 1$ pc,

$$n_{min} \sim 10^8 \Big(\frac{m}{3 \times 10^6 M\odot}\Big)\Big(\frac{r}{1pc}\Big)^{-3} cm^{-3}, \tag{2.1}$$

where the gravitational potential of extended stellar mass is ignored (Alexander 2005). In addition, the Galactic Center molecular clouds have large turbulent velocities ($\sim$10 km s^{-1}) and the entire region is a subject to unusually strong magnetic field ($\sim$1 mG, Aitken et al. 1998), both factors that can further inhibit star formation. Thus, star formation at the GC must be unique to this unusual environment. There are several scenarios that tried to offer a solution for this issue, and here we present two of them that are considered the most promising.

2.3.1 Star formation in a gaseous disk around Sgr A*

This scenario seems to be widely preferred at this point of time. The scenario proposes that the stars were form $in-situ$, by the fragmentation of a gaseous disk that gradually grew in mass to the point it became self-gravitating (Levin & Beloborodov 2003; Nayakshin et al. 2006a, 2007). Nayakshin et al. (2007) discussed numerical simulations of star formation both in a circular and eccentric disk around Sgr A*. They indicate that star formation in marginally self-gravitating disks results in top-heavy IMF and that, without feedback, it represents a very rapid process. The disk also exhibits an inner radius of $\sim$1", similar to what is observed. However, the simulations fail to produce stellar groups like IRS 13 clusters. The binaries of massive stars were produced in simulations by Nayakshin et al. (2007), but the disk fragments too fast to produce

the groups with higher multiplicity than that. Goodman & Tan (2004) propose that very massive objects (stars) can be formed in AGN accretion disks. The authors argue that the most massive objects formed in accretion disks will continue accreting matter until they grow to the isolation mass, approximately given by

$$M_{iso} \approx \frac{4\pi}{3} M_{disk}^{3/2} M_{BH}^{-1/2}, \tag{2.2}$$

(Lissauer 1987) or, in terms of the GC disk ($\sim 10^4\,\mathrm{M}_\odot$; Nayakshin 2006b) and BH mass,

$$M_{iso} \approx 530 M_\odot \Big(\frac{M_{disk}}{10^4 M_\odot}\Big)^{3/2} \Big(\frac{3.6 \times 10^6 M_\odot}{M_{BH}}\Big)^{1/2} \tag{2.3}$$

In AGN disks, M_{iso} would comprise a significant fraction of M_{disk} (Goodman & Tan 2004). Such a supermassive star would grow by accretion from a disk formed around it. The size of a disk would be of the order of the Hill radius (see equation 5.2) of the star. Milosavljević & Loeb (2004) find that this disk is also susceptible to fragmentation, and consequently separates into multiple clumps. Therefore a group of protostars shares the same Hill sphere. If the group contains more than three stars its spatial extent will increase beyond the original Hill sphere because of the strong two-body encounters. The final group then does not share the initial Hill sphere even if the initial group did, and it is tidally stretched. Milosavljević & Loeb (2004) propose that compact groups IRS 13E and 13N were formed this way.

2.3.2 Star formation in an in-falling stellar cluster

In order to circumvent the problem of the tidal field of the SMBH, another star formation scenario was proposed: The stars have been formed in a compact massive cluster at the safe distance 5-30 pc from the center (Gerhard 2001; McMillan & Portegies Zwart 2003; Kim et al. 2004; Portegies Zwart et al. 2006). Such a cluster would then undergo the dynamical friction and consequently spiral down to the center. A compact massive cluster of $\sim 10^4 \mathrm{M}_\odot$could sink from the distance of ~ 5 pc within the lifetime of its most massive stars. However, only the in-fall of a cluster with the extremely high central density ($\rho \sim 10^8 \mathrm{M}_\odot\ \mathrm{pc}^{-3}$) could actually result in the observed population in the central parsec (Kim & Morris 2003). Presently two massive clusters containing the young population similar to that at the center are observed at ~ 20 pc from

Sgr A*, named Quintuplet and Arches. However, neither of two is close to be massive enough to spiral-in and deposit young stars to the central parsec. Also, recent results by Stolte et al. (2007) on proper motion of Arches definitively ruled out the possibility that the Arches cluster could migrate inwards.

Considering the extreme densities of a putative massive cluster, an alternative was proposed by means of an intermediate-mass black hole (IMBH) in the center of a cluster (Hansen & Milosavljević 2003), possibly formed by runaway mergers in the cluster core (Portegies Zwart et al. 2004). This way the process of dynamical friction becomes more efficient and the stars most tightly bound to the IMBH will not be stripped until they reach the central 0.5 pc where they can be deposited in a disk-like structure. Maillard et al. (2004) proposed that such a IMBH could reside in the center of the IRS 13E cluster and help explaining its apparent boundness.

However, there are several issues with the massive-cluster-plus-IMBH scenario. Kim et al. (2004) find that the presence of an IMBH does lower the minimum initial core density required to transport young stars down to the central parsec, but only when the mass of the IMBH is at least 10% of the total cluster mass. This fraction is significantly higher than that estimated by Portegies Zwart & McMillan (2002) with numerical simulations of IMBH formation by successive merging of stars in the cluster core, so it does not appear that a realistic IMBH can help transport young stars into the central parsec. Another point is the lack of young stars at the radii >0.5 pc – the in-spiraling cluster would deposit stars all the way from its initial position towards the center, which is not observed. However, the one could argue that a initially mass-segregated cluster could account for this, but no quantitative analysis has been done so far.

Concerning IRS 13E, Schödel et al. (2005) have performed a proper motion analysis (see Fig. 5.1) and found that an IMBH in the center of the cluster must have a minimum mass of 10^4 $M_\odot$, in order to bind the source complex gravitationally. The authors note that this high-mass limit in combination with the absence of compelling evidence for a nonthermal radio and X-ray source in IRS 13E make the existence of an IMBH in its center appear unlikely. In addition, the proper motion of Sgr A* is inconsistent with the existence of a second object with a mass in excess of 10^4 $M_\odot$(Reid & Brunthaler 2004).

Paumard et al. (2006) note that the membership in the cluster is not completely clear and that any mass estimate relying on proper motions should be taken cautiously. The authors infer the lower limit on the stellar mass of the cluster to be $\sim$350 $M_\odot$and argue that, depending on the real 3-dimensional position of IRS 13E with respect to Sgr A*, may be stable against tidal forces, or at least long lived.

2.4 Dust emission from the Galactic Center

The 30 magnitudes of visual absorption towards the GC combined with presence of bright infrared sources in the region have lead to studies of dust grains along the line of sight. ISO-SWS spectrum (Lutz et al. 1996) of the GC in the 2.4 - 45 μm region is shown in Fig. 2.3. The aperture was centered on Sgr A*. For the short wavelengths the aperture was 14" $\times$ 20", and for long ones 20" $\times$ 33". Based on the ISO spectrum towards the GC Gibb et al. (2004) identified all the strong and weak features (see Fig. 2.3). The column densities of the species are derived from the model fit to the observed spectrum based on laboratory studies of analogue material. The spectrum shows a strong absorption feature at 2.96 μm, suggestive of the $N-H$ stretch feature in NH_3, but whose true nature is unknown (Gibb et al. 2004) Other features include prominent H_2O, CO_2, and CH_4-ice absorption, and hydrocarbon absorption features at 3.4, 6.2, 6.8, and 7.25 μm (Chiar et al. 2000).

The gas streamers at central parsec of the Galaxy contain a significant quantity of dust. This is evident from the NIR/MIR continuum emission. In Fig. 2.4 we show images of the central parsec of the Galactic Center at three different wavelengths. At short NIR wavelengths ($\sim$2 μm) the observed light is dominated by stellar emission from the central stellar cluster. At slightly longer wavelengths, the dust component becomes detectable so that already in the L-band ($\sim$ 3.5 μm) the dust significantly contributes to the overall flux of the region. The stellar component, however, is still very important (see the middle panel of Fig. 2.4). In the MIR only few stars are observed (Fig. 2.4, right). Some of these stars were suggested to be young stars still embedded in their dust cocoons, which was later discarded: they are rather luminous stars with strong stellar winds plowing through the local ISM (Tanner et al. 2005).

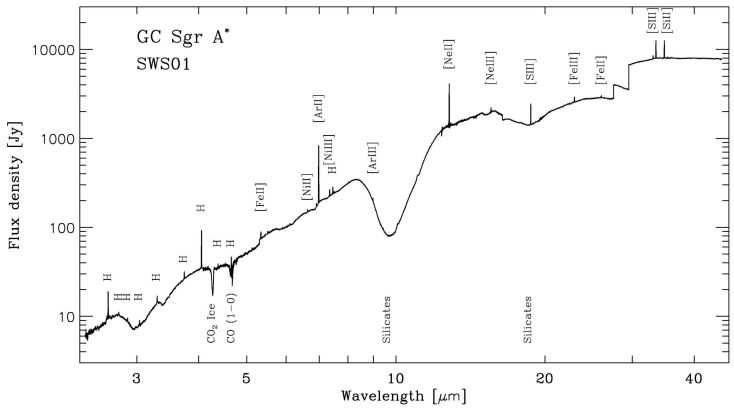

λ (μm)	FWHM (cm^{-1})	τ	Species	N (10^{17} cm^{-2})	N/N(H_2O) *100	Reference
3.0	335	0.50(0.01)	H_2O	12.4(2.5)	100	1
3.28		<0.02	C-H stretch	...	...	1
3.46	80	0.21(0.01)	HAC	...	...	1
3.54	30	<0.01	CH_3OH	<0.5	<4	1
3.95	115.3	<0.001	CH_3OH	<0.4	<3	1
4.27	16.7	0.70(0.01)	CO_2	1.7(0.2)	13.7(1.6)	2
4.38	7.2	<0.07	$^{13}CO_2$	<0.12	<1	3
4.5[a]	700	[0.017]	H_2O	[12.4]	[100]	3
4.62	29	∼0.14	XCN	∼0.83	∼6.7	4
4.67	7.64		CO	<1.5	<12	1
4.91	20	<0.03	OCS	<0.04	<0.3	3
5.81	21		H_2CO	<0.3	<2.4	1
6.02[a]	185	[0.07]	H_2O	[12.4]	[100]	3
6.0		<0.03	Organic residue	...	...	3
6.2	60	0.05(0.01)	?	...	...	1
6.85	88	0.05(0.01)	OrganicsNH_4^+	...	...	1
7.243	19	0.03(0.01)	HCOOH	0.8(0.2)	6.5(1.6)	1
7.676	10.4	0.017(0.003)	CH_4	0.30(0.07)	2.4(0.56)	1
9.0	68	<0.012	NH_3	<0.61	<4.9	5
9.7	176	2.31(0.02)	Silicate	...	...	3
13.3[a]	240	[0.11]	H_2O	[12.4]	[100]	3
15.2	20.3	0.077(0.005)	CO_2	1.7(0.2)	13.7(1.6)	2
			(Polar)	1.7	13.7	2
			(Nonpolar)	<0.1	<0.8	2
18	140	0.57(0.01)	Silicate	...	...	3

NOTE.—There are emission features at 2.62 μm (Brβ), 2.75 μm (Pfη), 2.87 μm (Pfζ), 3.03 μm (Pfε), 3.30 μm (Pfδ), 3.73 μm (Pfγ), 4.05 μm (Brα), 4.65 μm (Pfβ), 5.34 μm (Fe II, $^4F_{9/2}$–$^6D_{9/2}$?), 5.51 μm (H_2?), 5.91 μm (H I 9–6), 6.64 μm (Ni II $^2D_{3/2}$–$^2D_{5/2}$), 6.91 μm (H_2?), 6.98 μm (Ar II $^2P_{1/2}$–$^2P_{3/2}$), 7.35 μm (?), 7.46 μm (Pfα), 7.50 μm (Ni I $^3F_3$–$^3F_4$?), 12.81 μm (Ne II $^2P_{1/2}$–$^2P_{3/2}$), 15.56 μm (Ne III $^3P_1$–$^3P_2$), 18.71 μm (S III $^3P_2$–$^3P_1$), 22.93 μm (Fe III $^5D_3$–$^5D_4$), 25.91 μm (O IV $^2P_{3/2}$–$^2P_{1/2}$), 33.04 μm (Fe III $^5D_2$–$^5D_3$), 33.48 μm (S III $^3P_1$–$^3P_0$), 34.81 μm (Si II $^2P_{3/2}$–$^2P_{1/2}$), 35.35 μm ($^6D_{5/2}$–$^6D_{7/2}$), and 36.01 μm (Ne III $^3P_1$–$^3P_0$).

[a] Calculated from 3 μm feature.

REFERENCES.—(1) Chiar et al. 2000; (2) Gerakines et al. 1999; (3) this work; (4) Moneti et al. 2001; (5) Gibb et al. 2001.

Figure 2.3: Upper panel: *ISO-SWS spectrum of the Galactic Center from (Lutz et al. 1996).* ***Lower panel:*** *Table showing the spectral features present towards the GC (Gibb et al. 2004).*

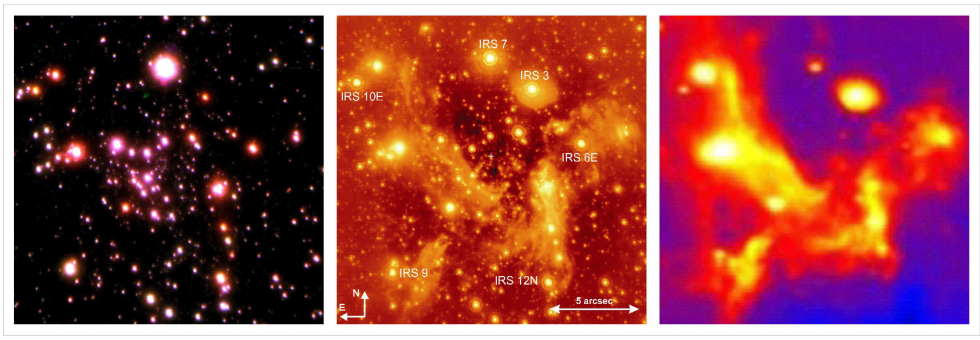

Figure 2.4: *The central parsec of the Galaxy at three different infrared wavelengths:* ***Left:*** *NACO K_S-band (2.2 μm) - the flux is predominantly coming from stars.* ***Middle:*** *NACO L'-band (3.8 μm) - stars contribute significantly to the total luminosity of the region; however, the local ISM is also observable. The emission is primarily coming from the warm dust.* ***Right:*** *VISIR N-band (8.6 μm) - the luminosity in the MIR is dominated by thermal dust emission.*

During the passage through the material of the mini-spiral their strong winds generate bow shocks. For several of these sources there is an agreement in the position angle of the source asymmetry and that of the inferred relative velocity vector of the NIR source with respect to the Northern Arm gas. The featureless 2.2 μm spectrum of IRS 21 suggests that the central source is an optically thick dust shell surrounding a mass-losing source, such as dusty WC9 Wolf-Rayet star (Tanner et al. 2002). The NIR light is scattered and extincted light, probably originated in a dusty photosphere overlying the central star. The MIR light is thermally re-radiated dust emission from the optically thin shell.

2.5 This work

This thesis is based on multi-epoch imaging of the central parsec of the Milky Way, observed with a broad band filter centered at 3.8 μm (L'-band). The observations and data reduction are presented in Chapter 3. There are several advantages of observing in the long-wavelength end of the NIR regime: the ISM component, mainly due to dust emission, becomes visible while the resolution achieved at the 8-m telescope is still relatively high, especially when

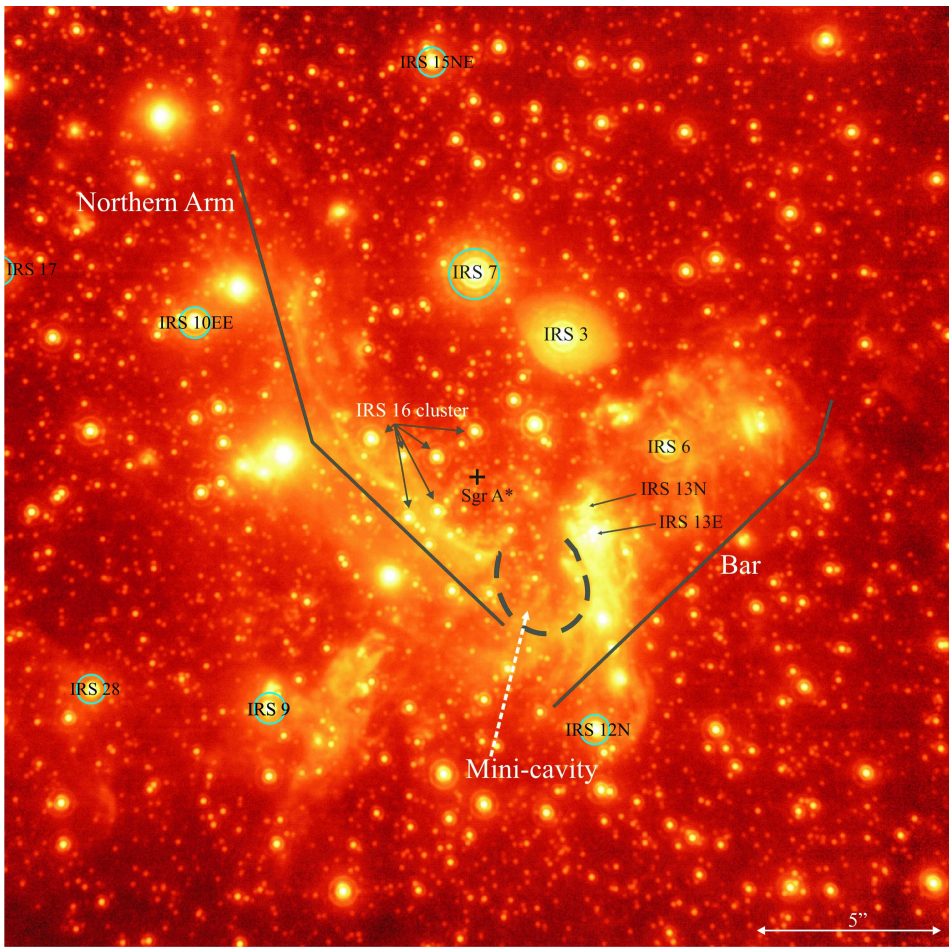

Figure 2.5: *NACO VLT L'-band (3.8 μm) image of the central 1pc$\times$1pc. Apart from the stellar sources, the ISM component becomes prominent at these wavelengths. The mini-spiral streamers (the Northern Arm and the Bar) reveal the narrow filaments in much higher number than in any of the previous datasets (compare to Fig. 4.1). Blue circles mark the SiO masers (Reid et al. 2003) used for astrometric calibration of our images (see section 3.4). The maser IRS 17 is located just outside this FOV, so that its bright halo can still be seen.*

compared to the resolution achieved in the MIR. The filaments of the mini-spiral (Chapter 4), with a width comparable to the resolution of the images, arise in much higher number than in any other dataset and allow us for the first time to measure their motions. Also, the stars observed at lower wavelengths are still bright in the L'-band, and additionally, several new infrared-excess sources were discovered, revealing the connection between stars and dust. One example of this kind of sources are the members of IRS 13N group, first reported by Eckart et al. (2004) and in detail discussed in Chapter 5.

Fig. 2.5 shows one of the L'-band images from our dataset. The stellar sources and gas streamers important for this thesis are highlighted. In the following section we shortly discuss physical mechanisms responsible for the observed emission.

2.5.1 The nature of the 3.8 μm emission

The L'-band flux from the mini-spiral is primarily coming from the thermal dust emission, which is confirmed by the observations at mid-infrared wavelengths (Viehmann et al. 2006). The detection of some of the narrow filaments in Pa α and Br γ tells us that the emission is as well associated with the ionized gas component of the ISM. In the L'-band, there is probably no significant contribution of the emission from the light scattered by dust grains. In this case one would expect to observe a significant amount of the polarized emission also at the shorter wavelength K-band - which is not observed (Eckart et al. 1995; Ott et al. 1999). Furthermore, there is no bright NIR source at the Galactic Center that could be identified as the source of large amounts of scattered light. Polarized emission from the mini-spiral observed at longer infrared wavelengths is due to thermal emission from elongated dust grains (Aitken et al. 1991, 1998).

Chapter 3

Observations and Data Reduction

All the observations used in this work have been obtained at the ESO Very Large Telescope (VLT), 8.2 m telescope with an Adaptive Optics (AO) system. The instrument used is NAOS/CONICA AO assisted imager/spectrometer (Lenzen et al. 1998; Rousset et al. 1998; Brandner et al. 2002) at the UT4 (Yepun). In this chapter I give a brief overview of limits in the optical/near-infrared imaging and the technology that provides diffraction limited images on the 8 m-class telescope in the near-infrared regime. Afterwards I describe the dataset used in this work, compare different deconvolution techniques and prove the reliability of the proper motion measurements in the lower resolution L'-band by comparison of stellar proper motions obtained from the L- and K-band images.

3.1 NIR imaging

3.1.1 Degradation effects and correction techniques

The images of the ground-based optical/near-infrared large telescopes are severely limited by the quasi-static errors in the telescope itself and the very

dynamic atmospheric turbulence inside and over the telescope. For a perfect telescope, the angular resolution is directly proportional to the inverse of the telescope diameter D:

$$\theta_0 = 1.22\frac{\lambda}{D} \tag{3.1}$$

The resulting image of an point source is the familiar Airy function, due to diffraction of light on the telescope aperture:

$$I(\theta) = I_0\Big(\frac{2J_1(\pi D sin\theta/\lambda)}{\pi D sin\theta/\lambda}\Big)^2 \tag{3.2}$$

where I_0 is the intensity in the center of the diffraction pattern and J_1 is the Bessel function of the first kind. In practice, however, a number of degradation factors originating in the atmosphere and within the telescope will distort the wavefront and degrade the image quality. Prior to 1980s, different mechanical improvements have been introduced in order to achieve better quality images. Improvements were made in mirror and other structure quality - stiffer structures were used to minimize gravitationally-induced deformations, and mirror polishing was improved. Local temperature effects were reduced by minimizing heat dissipation from electronics and the dome was cooled during the day. However, with the plans to build telescopes with diameters larger than 4 m it has become clear that new technologies have to be introduced. Very important role in this process had the advance of computer-controlled hardware that allows real-time corrections.

Sources of image quality degradation within the telescope include the residual errors of the telescope control system, deflection of the telescope structure induced by gravity, thermal expansion and wind buffeting. Slowly varying errors, for example those due to gravitational flexure and thermal effects, are corrected by the **Active Optics** system. The corrections are performed by means of mechanical control behind the mirror and are mainly deduced from real time analysis of the image of a star. The adjustments are done at fairly low temporal frequency ($\sim$0.05 Hz or less) and therefore the transient errors cannot be corrected using this technique. For correcting fast-changing wavefront aberrations, with speeds up to several tens of Hz, the principle of **Adaptive Optics** (AO) was invented. Using the AO systems, most of the distortions originating in the atmosphere can be accounted for. In short, the principle of work of AO is the following: incoming light is sent to a beam-splitter or a dichroic mirror that splits the light toward a wavefront sensor (WFS). The

WFS measures the distortions of the wavefront and sends this information to a correction device (deformable mirror and tip-tilt assembly). This way the wavefront is corrected and the final image is diffraction-limited[1]. For example, the VLT has a diffraction-limited resolution of $\lambda/\mathrm{D} = 0.057''$ at $\lambda = 2.2\,\mu$m. But, the resolution is severely limited by atmospheric turbulence to $\lambda/r_0 \approx 0.7''$, where r_0 is the Fried parameter:

$$r_0(\lambda) = 0.185\lambda^{6/5}\Big[\int_0^\infty C_n^2(z)dz\Big]^{-3/5} \tag{3.3}$$

C_n^2 is the *structure constant* for the refractive index and the value of the integral on the right side is found from the vertical distribution of the turbulence (Léna et al. 1998). From the Eq. 3.3 we see that the Fried parameter is directly linked to the strength of the turbulence and is highly chromatic. For example, $r_0(0.5\,\mu\mathrm{m}) = 10\,\mathrm{cm}$ implies $r_0(10\,\mu\mathrm{m}) = 3.6\,\mathrm{m}$. This means that a telescope with a given diameter will give images closer to the diffraction limit in the infrared than in the optical.
Another parameter characterizing the turbulence is the correlation time of the turbulence, τ_0, which is related to r_0 and the speed at which the turbulent air travels. For a wind speed of 10 m/s the correlation time is of the order of 60 ms at 2.2 μm. Both τ_0 and r_0 are critical parameters: The larger they are, the more stable the atmosphere is and the better the performance of the instrument will be.

Wavefront sensing is done using a bright and close star for guiding. "Close" here means within the *isoplanatic patch* - the region on the sky over which the distribution of the seeing cells over the aperture does not change significantly. It is characterized by the angle θ_0 that is directly proportional to r_0 and with the typical value of 20" the infrared, but less than 5" in the optical. Therefore the probability for finding a suitable star for guiding can be fairly low already in the infrared, and making it hopeless in the optical. A suitable star for guiding in the infrared in our case is the bright supergiant IRS 7, a member of the nuclear star cluster located ∼5.5" from Sgr A*.

Since it is often difficult to find an appropriate source for guiding, an alter-

[1]More about the principle of work and other useful information on adaptive optics systems can be found in e.g. *Adaptive Optics Tutorial at CTIO* by A. Tokovinin (http://www.ctio.noao.edu/ atokovin/tutorial/intro.html) or Claire Max lectures on adaptive optics (http://www.ucolick.org/%7Emax/289C/)

native technique had to be developed. This is the laser guide star (LGS) technique often done in the way that a sodium laser is focussed at 90 km altitude in the mesosphere. An atomic sodium layer present at that height backscatters the spot image and produces an artificial star to guide the AO servo-loop. Such an artificial reference star can be created as close to the astronomical target as desired.

The performance of an AO system is directly linked to the observing conditions. As we have seen, the most important parameters are the seeing (τ_0 and r_0), the brightness of the reference source used for WFS and the distance between the reference source and the object of interest. In case of good conditions and a bright, nearby reference source, the correction is good and the resulting PSF[2] is very close to the diffraction limit. A good correction in the K-band typically corresponds to a Strehl ratio larger than 30%. At shorter wavelengths (particularly in the J-band) or in the case of poor conditions or a faint, distant reference source, the correction is only partial - the Strehl ratio may only be a few percent.

3.1.2 Sky subtraction in the NIR

Longwards of 2.2 μm the background emission is dominated by the thermal emission. The thermal background consists from atmospheric and telescope emission. For instance, an overall telescope emissivity of $\sim$17% has been measured for the VLT. The influence of the thermal background is more important towards longer wavelengths and can often be brighter than the object we are observing. The Earth's atmosphere can be considered as a gas in LTE up to an altitude of 40 to 60 km (Léna et al. 1998). The intensity received at altitude z and at zenith distance θ can be approximated as:

$$I_\lambda(z) = \tau_\lambda B_\lambda(\bar{T}) \frac{1}{cos\theta} \tag{3.4}$$

where $B_\lambda(\bar{T})$ is the Planck function at the mean temperature $\bar{T}$ of the atmosphere. This simple approximation is valid for $\tau_\lambda \ll 1$, corresponding to an atmosphere which is transparent at the wavelength considered. This is the case

[2] *Point Spread Function* (PSF) is the response function of an imaging system to a point source

for NIR and mm atmospheric windows. In the L-band (3.4 μm), the mean value of the sky is L $\sim$ 8 mag and in M-band (5 μm) it is M $\sim$ 2 mag (Léna et al. 1998). We see that detectable astronomical sources can be several magnitudes fainter then the sky emission. Sky is also highly variable in the IR and therefore it is clear that the accurate sky subtraction is essential in this wavelength regime. It requires special attention and procedures.

Standard and very efficient procedure is to use a *jitter* technique (also called shift-and-add). The object is observed with small offsets from the central position and the sky background variation is deduced by filtering the images, and this way separating astronomical from the sky signal. Typical jitter mode acquisition is consisted of 10 – 100 frames. For a non-crowded field sky frames can be estimated from the object frames themselves. Several frames taken immediately before and after the frame from which we want to subtract the background. The main assumption here is that most of the observed signal is indeed sky background. For a crowded field or an extended object it is better to sample the sky at some dark region away from the object. The immediate drawback in this case is the loss of the observing time. The jittering technique can also take care of the detector cosmetics and instabilities.

The jittering technique was applied for all the Galactic Center observations presented in this theses.

3.2 Dataset

The Very Large Telescope (VLT) is consisted of four 8.2-m telescopes operated by Europen Southern Observatory (ESO), located at Paranal, Chile. Currently, the observatory hosts 11 instruments operating in the optical, near- and mid-infrared. The AO system using both NGS and LGS are offered for some of the NIR instruments. The Nasmyth Adaptive Optics System (NAOS) and the high-resolution NIR Camera (CONICA) are installed at the Nasmyth B focus of UT4. NAOS-CONICA provides multimode (imaging, spectroscopy, polarimetry and coronography), adaptive optics corrected observations in the range 1–5 μm.

Our main data set includes NACO broad-band L' ($\lambda = 3.8\,\mu$m,

$\Delta\lambda = 0.62\,\mu$m) images from 6 epochs (2002.66, 2003.36, 2004.32, 2005.36, 2006.41 and 2007.39) with a resolution of ∼100 mas and a pixel scale of 27 mas/pixel. The K_S-band ($\lambda = 2.18\,\mu$m, $\Delta\lambda = 0.35\,\mu$m) data set includes the images from epochs 2002.339, 2003.356, 2004.512, 2004.521 and 2006.413 with a resolution of ∼56 mas. Standard data reduction (bad pixel correction, sky subtraction, flat field correction) and formation of final mosaics was performed using the DPUSER software for astronomical image analysis (T. Ott; see also Eckart & Duhoux 1990). In case of deriving the IRS 13N proper motions, the images were deconvolved using the linear Wiener filter. The reason for this choice is described in section 3.3.

3.3 Comparison of deconvolution techniques

As we have seen above, any image obtained at a telescope will be influenced by several degradation factors. Therefore an image of a point source (a star) will be represented by some characteristic function, so-called PSF. For a ground-based telescope, the major source of image degradation is caused by the turbulence in the Earth's atmosphere, which can be accounted for by the AO system. Another solution is to launch a telescope into an orbit around the Earth to completely avoid this problem. However, even for a perfect optical system, i.e. the one without any atmospheric influence or other degrading factors, the image of the point source will be represented by an Airy function, a consequence of the diffraction of light on the aperture of the telescope (see Eq. 3.2). In case of a circular aperture, a star will appear as a central bright spot surrounded by concentric rings.

Generally, the observed image of an object I(x,y) can be described by the convolution of the real object O(x,y) and a PSF(x,y), plus and an additional noise term N(x,y) describing detector noise, anisoplanicity and other non-linear terms:

$$I(x,y) = PSF(x,y) \odot O(x,y) + N(x,y) \tag{3.5}$$

with $\odot$ sign representing convolution, i.e. multiplication in Fourier space. In Fourier space we have:

$$\hat{I} = P\hat{S}F \cdot \hat{O} + \hat{N}. \tag{3.6}$$

We want to determine $O(x, y)$ knowing PSF and I. This process is known as deconvolution and is in general an ill-posed problem, meaning that there is no unique solution for it. The main difficulties are: (i) a cutoff frequency to the PSF, and (ii) the additive noise term.

3.3.1 Estimating the PSF

For most of the deconvolution algorithms one needs to determine the PSF before starting the deconvolution. PSF can be obtained either by observing a PSF reference source (an isolated stars close to the observed object), or by extracting from individual point sources in the observed image. The latter method was used in case of the Galactic Center, using the software package *StarFinder* (Diolaiti et al. 2000). *StarFinder* is an IDL program for stellar field analysis, designed for AO data and intended as a tool to obtain high precision astrometry and photometry of point sources in adequately sampled high-resolution images of crowded fields. In practice, however, it can also be used in low-Strehl ration images with or without AO. *StarFinder* creates an initial estimate of the PSF from the median of several bright and isolated stars chosen by the user. The PSF estimate can be further improved by identifying stars in the image and taking them into account during the repeated extraction of the PSF. This way the contaminating sources close to chosen PSF stars can be subtracted in order to enhance the quality of the final PSF.

In the following I briefly describe deconvolution techniques used in the case of the Galactic Center, compare them and explain the final choice in case of determining proper motions. For more details see e.g. Eckart et al. (2005) and Starck & Murtagh (2006).

3.3.2 Linear deconvolution

This method computes the Fourier transform of the deconvolved object by simple division between the image $\hat{I}$ and the point spread function $\hat{PSF}$:

$$\hat{\tilde{O}} = \frac{\hat{I}}{\hat{PSF}} = \hat{O} + \frac{\hat{N}}{\hat{PSF}} \tag{3.7}$$

For frequencies close to the cutoff frequency, where PSF $\rightarrow 0$, the noise term becomes important, and the noise is amplified. One way to solve this problem is to introduce a filter that suppresses high spatial frequencies. Commonly used filter is the so-called Wiener filter defined as:

$$\hat{W} = \frac{|\hat{S}|^2}{|\hat{S}|^2 + |\hat{N}|^2}, \tag{3.8}$$

where $|\hat{S}|^2$ and $|\hat{N}|^2$ represent spectral density of the signal and the noise. In practice, $|\hat{N}|^2$ can be approximated by the Fourier transform of a delta function.

The main advantage of using linear deconvolution is that the algorithm is very fast. Serious drawback is the artefact creation: characteristic rings appear around point sources in the reconstructed image.

3.3.3 Lucy-Richardson deconvolution

The Lucy-Richardson (LR) algorithm (Richardson 1992; Lucy 1974) is based on Bayes' theorem on conditional probabilities. It is an iterative method that can be mathematically described by:

$$O^{n+1} = O^n[\frac{I}{I^n} \odot PSF^*] \tag{3.9}$$

$$I^n = PSF \odot O^n.$$

The current estimate of an object is convolved with the PSF and then compared with the observed image in order to obtain a new estimate. Because of the convolution with the PSF in first equation of 3.9, high spatial frequencies will be suppressed and the amplification of noise therefore avoided. Consequently, details of the image related to high frequencies will be resolved only after a sufficient number of iterations. On the other hand, LR deconvolution tends to resolve a diffuse background into point sources when running a high number of iterations. Thus, a number of iterations has to be carefully chosen in order to achieve a compromise. In LR deconvolution the flux is preserved. The disadvantages of LR algorithm are the high demand on computer time and dark areas around bright stars that can be minimized by an accurate PSF determination.

3.3.4 Multiresolution support for deconvolution

Another method we tested is the wavelet-based deconvolution using the Multiresolution Analysis Software developed by CEA (Saclay, France) and Nice Observatory. The detailed description of applications contained in the software[3] can be found in Starck & Murtagh (2006). The basic difference from the previously described deconvolution techniques is the choice of wavelets as basis functions, instead of Fourier functions. The multiresolution regularization can be applied on different well known deconvolution algorithms; our choice was Lucy-Richardson method. The noise is suppressed in the following manner (see Starck & Murtagh 2006 and references therein): In the LR iterative algorithm, the residual at iteration n is defined as:

$$R^n(x,y) = I(x,y) - (PSF \odot O^n)(x,y) \tag{3.10}$$

By using á trous wavelet transform algorithm , R^n can be defined as the sum of its J wavelet scales and the last smooth array:

$$R^n(x,y) = c_{J,x,y} + \sum_{j=1}^{J} w_{j,x,y} \tag{3.11}$$

where the first term on the right is the last smoothed array and w denotes a wavelet scale. The wavelet coefficients provide a mechanism to extract only the significant structures from the residuals at each iteration. Normally, a large part of these residuals is statistically non-significant. The significant residual is then

$$\bar{R}^n(x,y) = c_{J,x,y} + \sum_{j=1}^{J} M(j,x,y) w_{j,x,y} \tag{3.12}$$

where M(j,x,y) is the multiresolution support, and is defined by:

$$M(j,x,y) = \begin{cases} 1 & \text{if } w_{j,x,y} \text{ is significant} \\ 0 & \text{if } w_{j,x,y} \text{ is non-significant} \end{cases} \tag{3.13}$$

Assuming that noise follows a certain distribution, one can define a threshold for (non) significance of the signal. From the equation 3.5, we have $I^n(x,y) =$

[3] see http://www.multiresolution.com/ for detail description of the software itself and the supporting documentation.

$(PSF \odot O^n(x,y)$. Then we have $R^n(x,y) = I(x,y) - I^n(x,y)$. The LR equation becomes

$$O^{n+1}(x,y) = O^n(x,y)\Big[\frac{I^n(x,y) + \bar{R}^n(x,y)}{I^n(x,y)} \odot PSF^*(x,y)\Big] \tag{3.14}$$

The standard deviation of the residual decreases until no more significant structures are found. The algorithm stops when a user-specified threshold is reached:

$$\frac{\sigma_{R^{n-1}} - \sigma_{R^n}}{\sigma_{R^n}} < \epsilon. \tag{3.15}$$

The deconvolution algorithms discussed above were applied on the GC L'-band data (Fig. 3.1). Fourier-based LR (Fig. 3.1 bottom left) and wavelet-based LR (bottom right) look fairly similar. The differences can be seen on the frame edges and in the diffuse background: after the same number of iterations, the latter technique gives a smoother background and, in contrast to "normal" LR, do not tend to resolve it into point sources.

3.3.5 Application of deconvolution techniques to our data

After discussing several deconvolution techniques, the next step is to choose one to be finally used for proper motion measurements. In order to compare them we distributed 25 faint artificial stars with known proper motions across the field. Then we performed proper motion measurements from the frames previously deconvolved by methods described above, as well as from the original, non-deconvolved frames. The results are shown in Fig. 3.2. We see that proper motions from the linearly deconvolved data give the best match with the real proper motions. Thus, our final choice was the linear deconvolution using Wiener filter.

It is important to note that deconvolved images were constructed only to determine positions of stellar sources, finally used for obtaining proper motions of IRS 13 stars (Chapter 5). Because of the influence of the deconvolution techniques on the background (i.e. the extended sources), we preferred not to deconvolve the images used for proper motions of narrow extended filaments (Chapter 4).

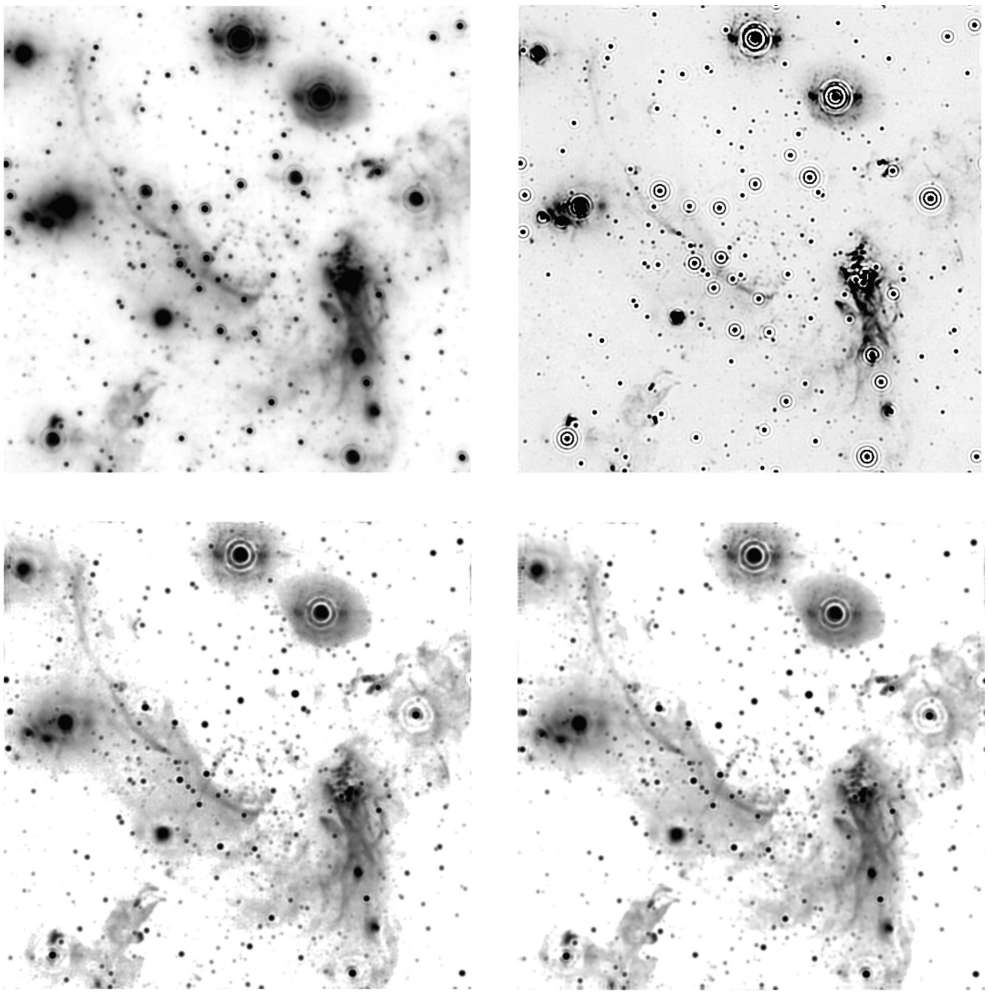

Figure 3.1: *Top left: L'-band image of the GC central parsec from the epoch 2003.36. This image was deconvolved using (i) Wiener linear deconvolution (top right), (ii) Lucy-Richardson (bottom left) and (iii) wavelet-based Lucy-Richardson (bottom right) algorithm. LR image was smoothed with the Gaussian of FWHM* $\approx$ *resolution of the data.*

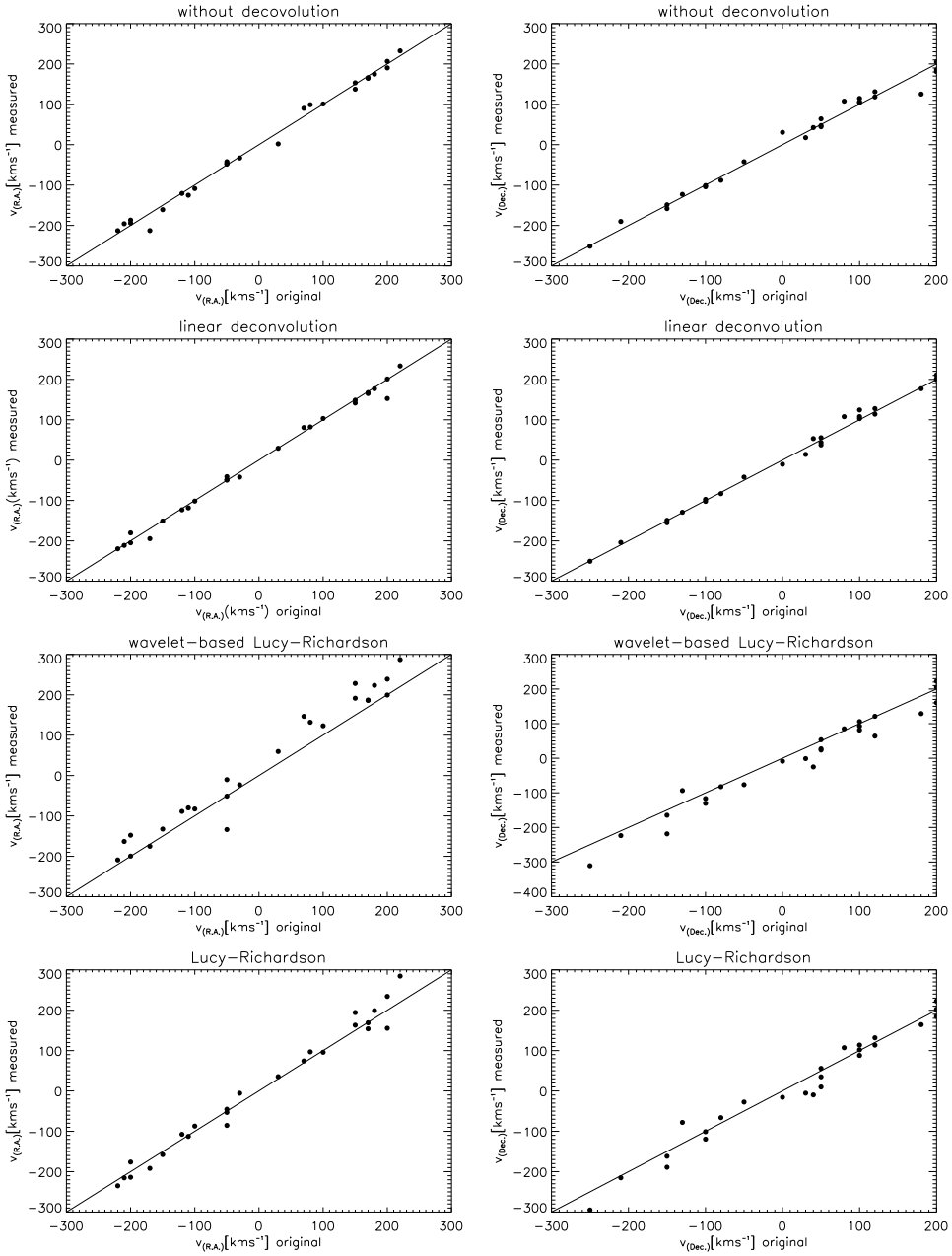

Figure 3.2: *Comparison of different deconvolution techniques. The x-axes show the real proper motions of stars and y-axes show measured ones. Solid lines in all diagrams represent the function $y = x$.*

3.4 Absolute astrometric frame

In contrast to radio wavelengths, Sgr A* is very dim in the infrared and therefore difficult to identify. Fortunately, there are several red giants in the GC stellar cluster that are both strong radio and bright infrared sources. The radio luminosity of these sources is due to silicon monoxide (SiO) maser emission in the innermost regions of their circumstellar envelopes (Menten et al. 1997; Reid et al. 2003). Reid et al. (2003) calculated the precise positions and proper motions of several SiO maser within 15" from Sgr A*, combining VLA and VLBA observations. The absolute positions of sources in this work (always expressed as offsets from Sgr A*) were determined by comparison of IRS 10EE, 28, 9, 12N, 17, 7 and 15NE positions in our frames to their positions as given by Reid et al. (2003). SiO masers are marked in Fig. 2.5.

3.5 Proper motion measurements

Stellar sources

When measuring proper motions of stellar sources in the L'-band, the following procedure is used: First, the stellar position in different frames are extracted via the PSF fitting, using *StarFinder*. We note that the PSF was extracted from the sufficiently small FOV within which the PSF can be considered stable. Next step is to perform the transformation of the stellar positions to a reference system. Here we chose one of our images (one from the year 2003), in order not to introduce the error of the transformation to the absolute astrometric system. The transformation of the second order was performed with the aid of 19 reference stars evenly distributed across the field, with the positions previously corrected for proper motions obtained in the K-band. Proper motions were derived by linear fitting of positions as a function of time, weighted by the positional uncertainties. Both the error of the transformation to the reference frame and the error of the stellar position fitting contribute to the uncertainties.

Extended sources

Extended features require a different approach when measuring their motions. For measuring the proper motions of narrow filaments, we used the cross-correlation technique. In this case, entire images have to be transformed to

a common coordinate system. This was done using IDL image transformation routines POLYWARP and POLY_2D. Transformation to second order was performed providing correction of all translations, rotations and possible distortions between two images. All the frames were transformed to the coordinate system of the 2003.356 epoch using a total of 34 stars to calculate the transformation matrix. The stars used for the transformation were chosen to be uniformly distributed across the field. The positions were corrected for the stellar proper motions as derived from the K_S-band images.

While further details on the method for offset determination will be given in Section 4.2, here we want to validate our transformation method and to demonstrate that reliable proper motions can be obtained from the lower resolution L'-band data. Thus we compared K_S-band and L'-band stellar proper motions in the following section.

Table 3.1: *Comparison of stellar proper motions in K_S- and L'-band. All velocities are in $km\,s^{-1}$.*

				K_S		L'		$G00$ [a]		K_S		L'		$G00$ [a]	
name	r [b] (arcsec)	$\Delta\alpha$ [b] (arcsec)	$\Delta\delta$ [b] (arcsec)	v_α	Δv_α	v_α	Δv_α	v_α	Δv_α	v_δ	Δv_δ	v_δ	Δv_δ	v_δ	Δv_δ
	1.05	0.80	-0.68	426	14	431	31	410	80	23	12	9	11	50	100
IRS 16C	1.21	1.10	0.50	-285	9	-336	22	-330	39	268	11	222	6	353	34
	1.45	-1.35	0.52	-52	9	-53	37	-58	95	-181	10	-212	29	-116	62
	2.07	1.90	-0.82	228	14	218	38	154	84	100	13	62	24	13	44
IRS 16CC	2.07	1.99	0.55	-48	9	-55	22	-58	35	183	10	174	7	234	27
	2.18	1.85	-1.15	254	9	248	23	255	28	20	10	47	8	113	23
IRS 33N	2.20	-0.05	-2.20	103	9	131	31	70	48	-309	10	-339	14	-243	28
	2.66	-2.63	0.42	-326	14	-285	62			-178	15	-149	44		
	3.17	2.94	-1.19	139	10	121	27	147	51	87	11	85	15	111	55
	3.20	0.66	-3.13	230	7	262	25			-154	9	-147	14		
	3.22	3.22	-0.01	75	10	53	27			-352	11	-372	23		
	3.39	1.66	-2.96	0	10	-27	31			58	11	52	6		
	3.47	3.24	-1.25	-11	17	-11	27			-178	13	-175	16		
	3.84	-1.26	3.63	204	11	206	46			148	12	124	18		
	4.15	-3.34	2.46	-123	12	-102	39			402	12	405	16		
	4.19	4.19	0.11	181	12	177	29			-13	11	-26	25		
	4.55	2.95	3.46	237	10	247	25			-52	10	-46	5		
	4.99	2.20	4.48	248	12	248	22			-120	12	-118	6		
IRS 2L	5.95	-3.68	-4.67	-118	11	-89	22			-252	12	-288	14		
	6.30	2.85	-5.62	229	12	239	32			4	11	26	30		
	6.62	0.94	-6.55	-55	11	-57	39			-48	11	-59	18		
	6.90	5.09	4.66	102	18	108	37			-154	15	-148	20		
IRS 1NE	7.26	7.02	1.84	209	9	187	18			-45	10	-12	7		
IRS 1SE	7.51	7.50	-0.45	150	9	110	17			-80	10	-85	25		
	7.84	-5.51	-5.57	-32	10	-59	20			198	11	193	21		
IRS 30E	8.00	-5.69	5.62	87	10	117	31	60	60	149	10	105	19	75	30
	8.30	3.95	-7.30	98	10	108	32			-374	11	-337	30		

[a] data from Genzel et al. (2000)

[b] relative to Sgr A*; position in the 2003.356 epoch

3.6 L'- and K_S-band stellar proper motion comparison

L'-band image frames from different epochs have been transformed to the coordinate system of a reference frame using IDL image transformation routines. In order to validate our method and to demonstrate that (*i*) reliable proper motions can be obtained from the lower resolution L'-band data and (*ii*) that the resulting transformed images therefore are indeed astrometric and suitable for the measurements conducted in this work, we compare K_S-band and L'-band stellar proper motions. The PSF fitting was done using the StarFinder code (Diolaiti et al. 2000). While the L'-band positions were obtained from transformed images we derived the K_S-band positions from the original image frames and applied the corresponding transformation to the resulting lists. So the basic difference between two sets of proper motions is in the transformation of data to the reference coordinate system.

As can be seen from Fig. 3.4, 97% of our K_S- and L'-band stellar proper motion results are in agreement to within 3σ. Also, there is no systematic offset between proper motion difference when projected in R. A. and Dec. (see histograms in Fig. 3.5). This demonstrates that the L'-band image transformation we used produces astrometric frames. As an example, we list in Table 3.1 proper motions for some of the sources in the central parsec obtained in our study (K_S- and L'). We also add the values published in Genzel et al. (2000). The uncertainties of the proper motions represent the 1σ deviation of the linear fit.

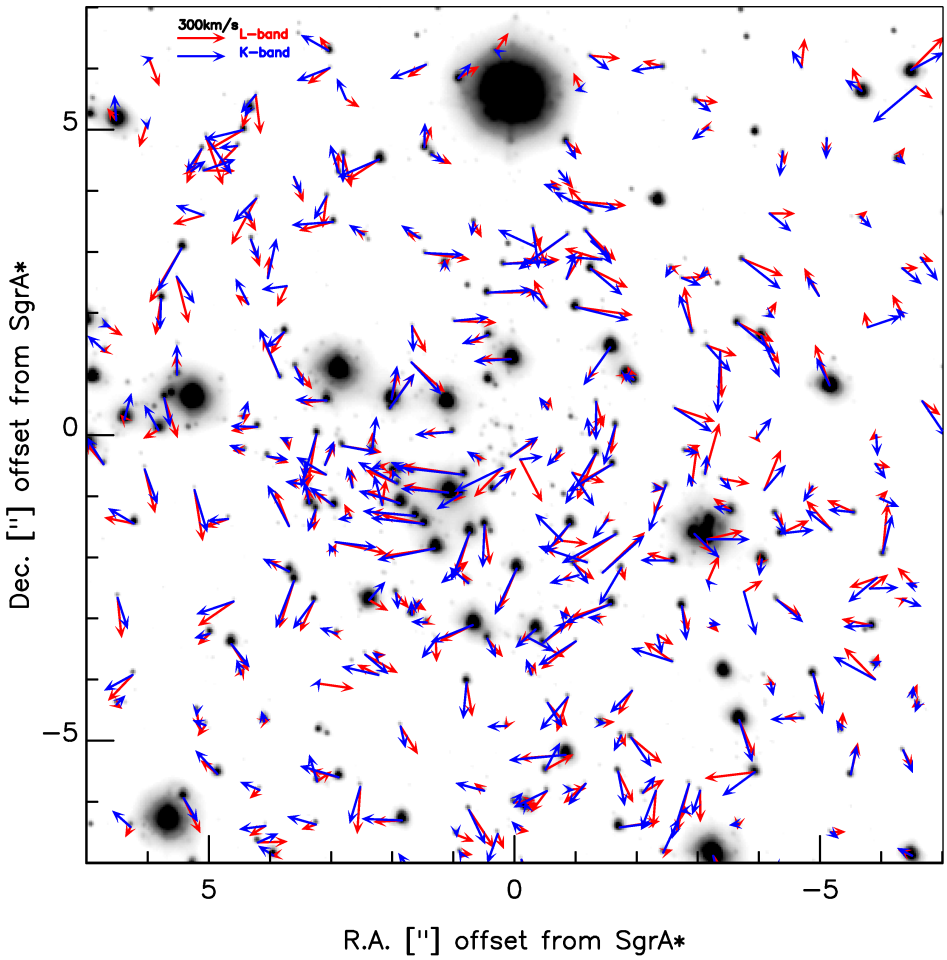

Figure 3.3: *Comparison between the proper motions obtained in the K- and the L-band. Here we show only the central 14"× 14", but the comparison has originaly been performed for stars in a larger FOV.*

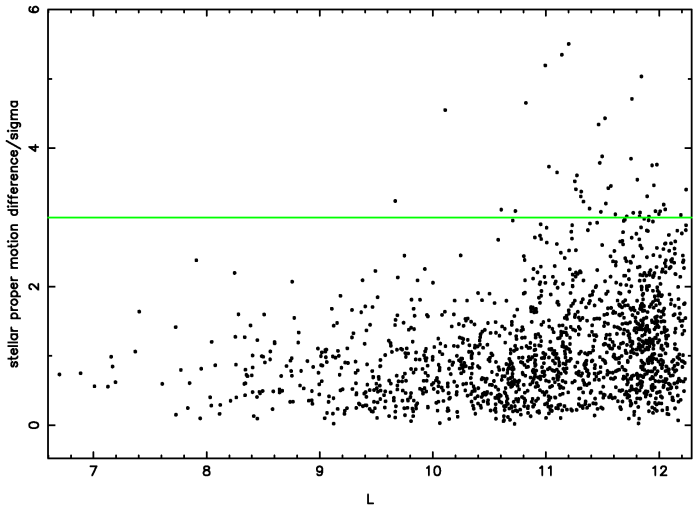

Figure 3.4: *L'- and K_S-band stellar proper motion difference vs. L' magnitude. The y-axis labels are calculated via $|\vec{v_K}\text{-}\vec{v_L}|/\ \sigma(|\vec{v_K}\text{-}\vec{v_L}|)$, where $\vec{v_K}$ and $\vec{v_L}$ represent the proper motion of a star as measured from K_S- and L'-band frames, respectively, and $\sigma(|\vec{v_K}\text{-}\vec{v_L}|)$ represents the standard deviation of the difference between two measurements. We find that 97 % of all the sources lie below the 3 σ line.*

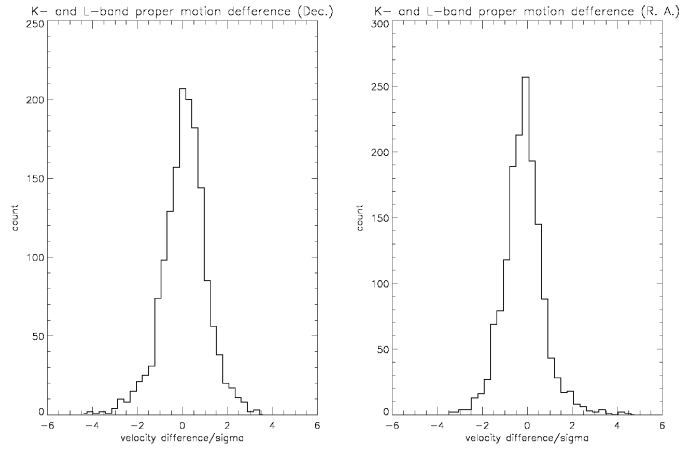

Figure 3.5: *K_S- and L'-band proper motion difference projected in R. A. and Dec.*

Chapter 4

Proper motions of narrow filaments

In the previously published observations of the mini-spiral, a number of narrow, filamentary structures have been reported. The observations include high-resolution radio data (Zhao & Goss 1998; Yusef-Zadeh et al. 1998) and NIR Pa α (Scoville et al. 2003), Br γ (Morris 2000) and He I (Paumard et al. 2001) emission line maps. As an example, in Fig. 4.1 we show the radio continuum and Pa α images, indicating several of the resolved filamentary structures. Observations in the L'-band (3.8 μm; see Fig. 2.5) performed with the NACO adaptive optics system at the ESO VLT revealed the filaments in much larger number than in any previous dataset. The features in our images are narrow, with the width of $\sim$100 mas which corresponds to the angular resolution of the images. Another important property of the high-resolution and high-sensitivity AO observations in the L'-band is that for the first time we were actually able to measure the filaments with high precision. In this chapter we present the first proper motions of the narrow filaments associated with the mini-spiral, and that of several bow-shocks associated with stars in the central parsec.

The NACO L'-band observations performed during the science verification of the instrument (in 2002) have been published by Clénet et al. (2004). The authors report the existence of some of the filaments, particularly those associated with the Northern Arm (NA) and one detected stellar bow shock. Based

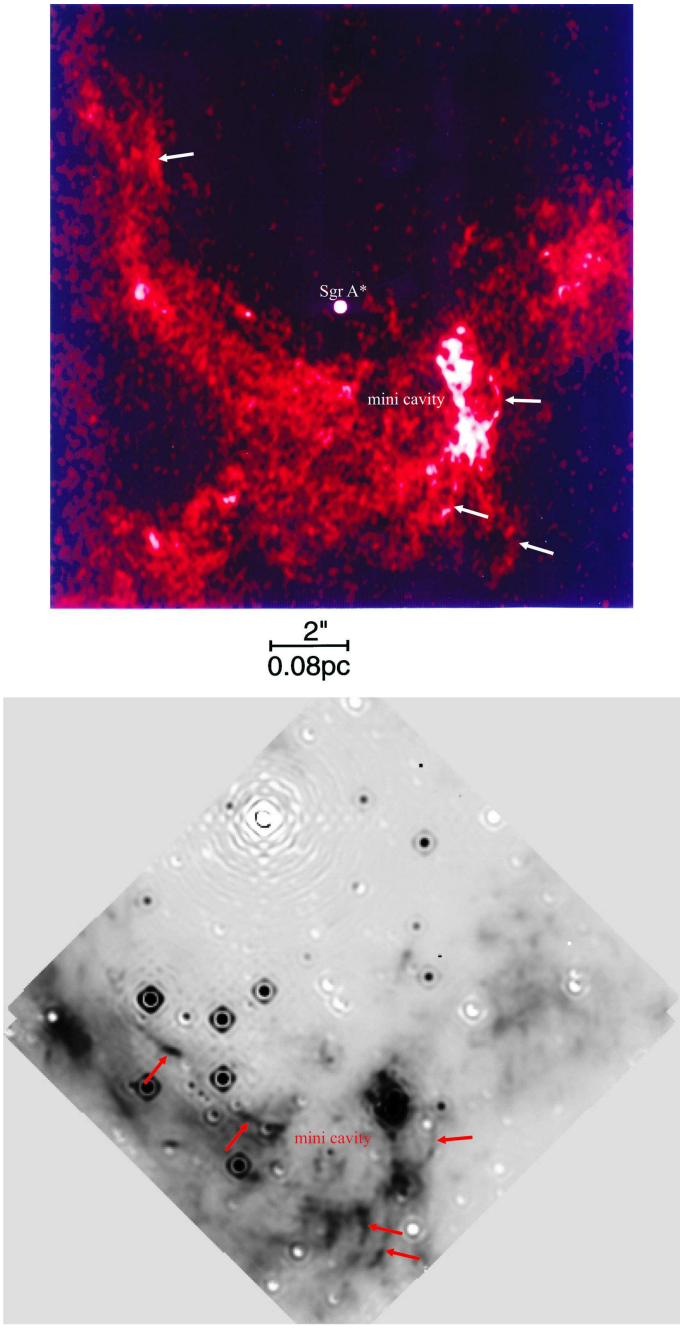

Figure 4.1: *Top: 13 mm radio continuum image of central $\sim 0.6 \times 0.5\,pc^2$ of the Galaxy (Zhao & Goss 1998). Bottom: HST NICMOS Paα image (F. Yusef-Zadeh, private communication). The arrows in both images are indicating the narrow filaments.*

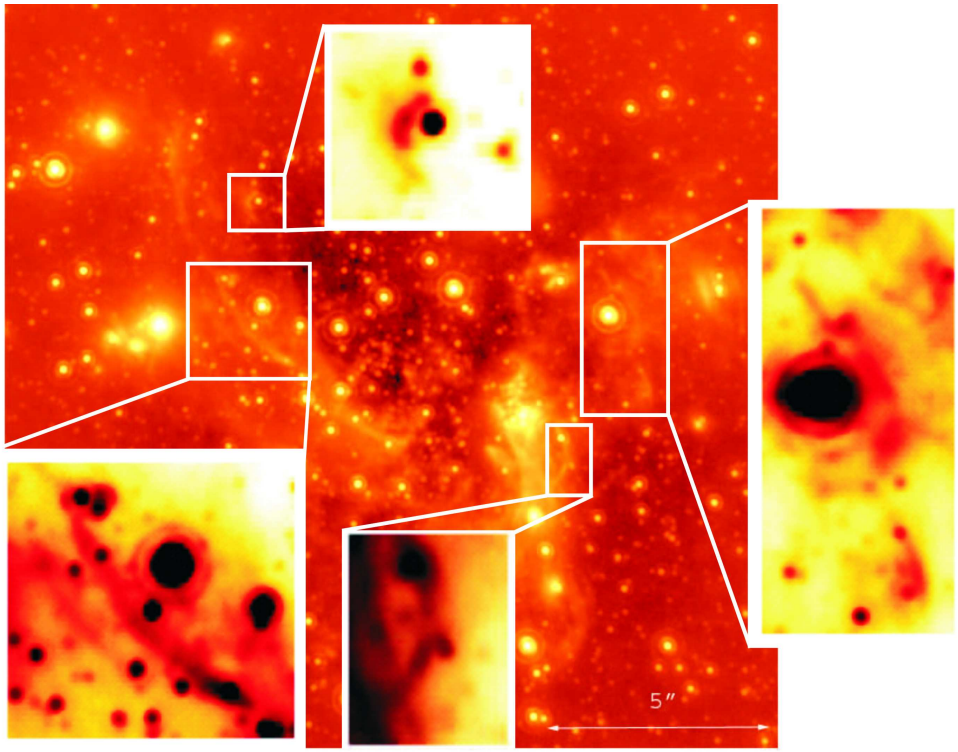

Figure 4.2: *Zoom into some of the regions containing the narrow filaments. The scale in insets is changed for display purposes.*

only on the morphology and the brightness of the NA filaments, the author suggest that they might trace dust heated by shock compression and therefore make some precedent interpretations of the NA structure invalid. Based on filaments kinematics, we will give more evidence that this is indeed true.

The results presented in this chapter have fully been published in Mužić et al. (2007).

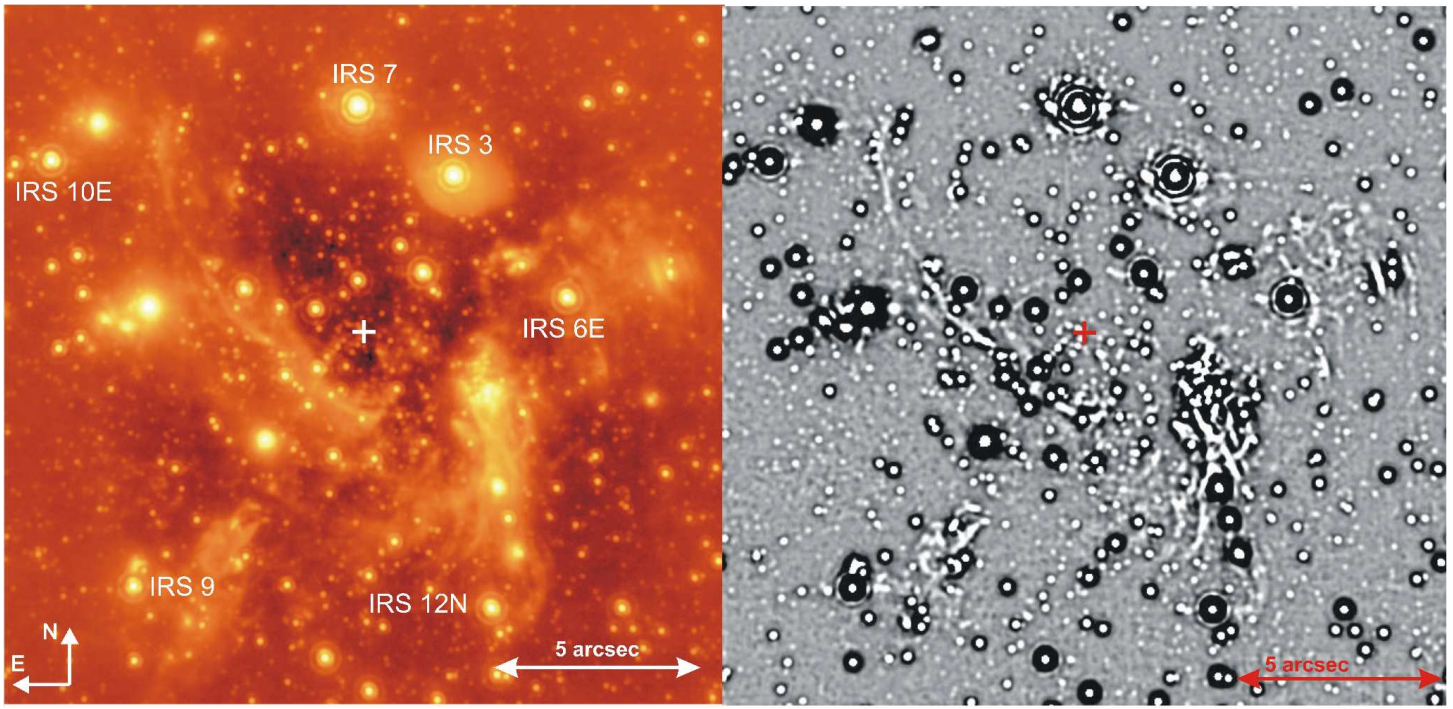

Figure 4.3: Left: *L'-band image of the central part of the Milky Way ($\sim 18 \times 18\,\mathrm{arcsec}^2$). The image contains a large number of dust embedded stellar sources, mini-spiral emission and several previously unknown thin filaments. The image has a pixel scale of 27 mas/pixel and resolution ~ 100 mas.* ***Right:*** *High-pass filtered (smooth-subtracted) version of the image shown on the left. Here all compact features are enhanced. Cross in both images marks the position of Sgr A*.*

4.1 Identification of the thin filaments

The L'-band images (left panel in Fig. 4.3) clearly show stars, bright dust embedded sources as well as the emission of the mini-spiral. In addition, one can distinguish a number of previously unknown thin filaments. In order to highlight these structures we produced high-pass filtered maps (Fig. 4.3, right) by subtracting a smoothed version of the images from themselves, and then smoothing the final images. As a smoothing function in both cases we used a 4 pixel Gaussian (1 pixel corresponds to 0.027"). This procedure enhances all structures that have significant power at spatial frequencies that correspond to the diffraction limited beam size.

The thin filaments that are apparent in the L'-band maps are located close to the mini-cavity, along the inner edge of the Northern Arm and, in some cases, in the vicinity of stars. The width of the filaments is $\lesssim 100$ mas, the diffraction limit of NACO L'-band images. Fig. 4.4 shows a schematic representation of the thin features in the central parsec of the Milky Way as derived from the data shown in the right panel of Fig. 4.3.

According to their appearance we can divide the filaments in two classes: the first class represents features most probably associated with stars (denominated with X); the second class features are more elongated and associated with the mini-spiral. Those located west and south from Sgr A* are denominated SW and those associated with the Northern Arm and located east from Sgr A* we label NE. They cannot be associated with stars in a straightforward way. We find that the second class of filaments to the east and northeast of Sgr A* are located at the inner side of the Northern Arm and curved with their convex sides eastward, whereas filaments to the west and southwest of Sgr A* are curved with their convex sides westward and elongated almost perpendicularly to the Bar. Several of the more luminous filaments to the west and southwest are located on the western side of the mini-cavity close (in projection) to the IRS13/IRS2 complex or just south of it (most prominent are SW5, SW6, SW7, SW8). One can also notice that some of these filaments are located up to about 5" SSW of Sgr A*, almost opposite to and approximately at the same distance as the most distant filament in the Northern Arm. Concerning the X features, we notice no preferred direction towards which they are curved. We discuss their possible nature in section 4.3.1.

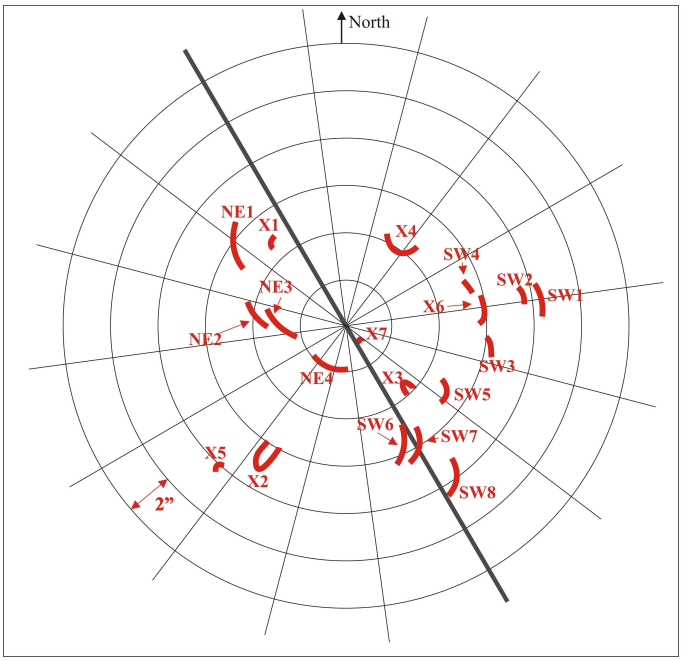

Figure 4.4: *Identification of the thin features observed in the the L'-band. Sgr A* is located at the center of the image. We have marked the line of nodes for disk (i) at a position angle of 28º on the sky (N to E) that contains the Northern Arm in the model by Vollmer & Duschl (2000).*

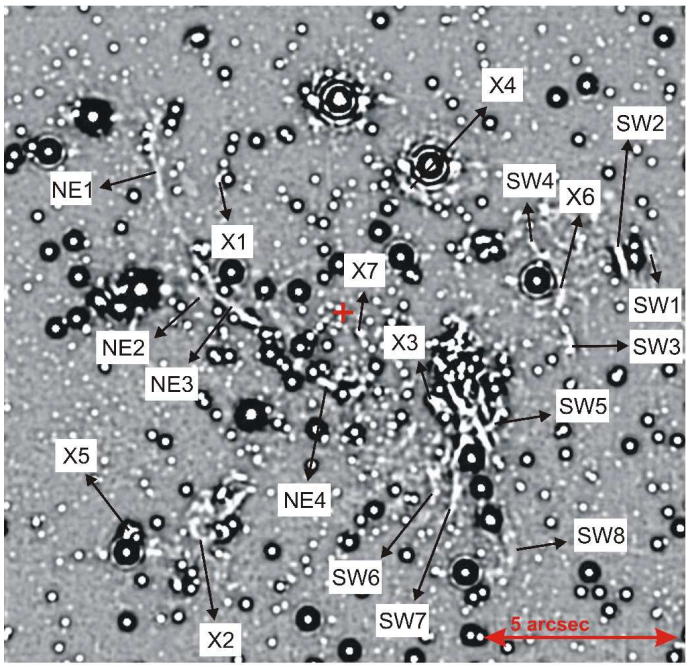

Figure 4.5: *High-pass filtered image with the narrow features labeled.*

4.2 Methods for proper motion measurements

In Section 3.5 we discussed the difference in proper motion determination for the point and extended sources, and the necessity for the full image transformation into the common coordinate system. Here we focus our attention onto the narrow filament offset determination.

4.2.1 Offset determination

In order to measure proper motions of the observed thin filaments we calculated offsets at all epochs with respect to the reference epoch (2003.356). First, we extracted an image section containing the entire feature, or the part of the feature that is not directly contaminated by stars. The position of the center and dimensions of the image sections are given in Table 4.3.2. Then we re-binned those image sections by a factor of 10 (since all the offsets are

on sub-pixel scale), masked residual stars if present in the frame, and finally subtracted the background. The resulting small frames were cross-correlated with a reference frame in order to calculate the offset of the feature with respect to the reference position. The principle of cross-correlation is fairly simple: the second image is shifted by number of offsets (i, j) with respect to the reference image. For each single offset we calculate a single value of the cross-correlation function:

$$cc(i,j) = \sum (p_1 \odot p_2)_{i,j} \tag{4.1}$$

where p_1 and p_2 are flux values (counts) of two pixels in two images found at the same position. The sum goes over all overlapping pixels in two images. $p_1 \odot p_2$ represent some mathematical operation performed on two overlapping pixels, usually chosen as:

$$(p_1 \odot p_2) = (p_1 \cdot p_2)^2 \quad \text{or} \quad (p_1 \odot p_2) = (p_1 - p_2)^2 \tag{4.2}$$

The second choice is often chosen when dealing with extended structures. Taking the inverse of $cc(i, j)$, results in a 2D cross-correlation function which can then be fitted with a 2D Gaussian to determine the exact position of the peak that represents the best overlap of two features. Using the described method, it is therefore possible to obtain the offset of an extended feature with respect to the reference one on a sub-pixel scale.

4.2.2 Uncertainties of our measurements

There are two main sources of error that occur during the determination of the offset. The first is caused by the uncertainties due to the cross-correlation method. In order to determine this uncertainty for each feature and epoch, we shift it by different known sub-pixel offsets in all directions, run the cross-correlation routine and then calculate the standard deviation obtained from the imposed and derived shifts. The second is resulting from the frame transformation procedure. From the initial sample of 34 stars we have randomly chosen 50 different sub-samples of 20 stars each. For all sub-samples we then repeated the transformation of all frames and calculated the positional uncertainty. The error bars in diagrams in Fig. 4.8 contain contributions of both sources of uncertainty.

4.2.3 Extraction of the extended features

It is important to note that the extraction of stars from our images via PSF fitting leaves significant residuals at the positions of the brightest stars. Thus, our approach was to extract sub-images containing the filaments from the original L'-band images if possible. Due to the presence of a large number of stars in L'-band images, some of the identified features could not be extracted at all to perform the cross-correlation (e. g. SW6, SW8, NE2). In some cases we were only able to extract one part of the filament, rather then the entire structure. Besides the proximity of stellar sources, there is another reason for this: Many of the filaments are parts of more extended structures and could not be completely isolated. This means that the positional data along the feature do not result in a measurable proper motion. Therefore, the velocities of all NE and SW features, except that of the compact features SW7 and NE4, are measured approximately perpendicular to their extent. Some of the features are very faint in the L'-band and therefore unsuitable for the extraction. They can be more clearly identified in the smooth-subtracted images (features SW7, SW1, X4 and X6). In this case, only the SW7 appearance is sharp enough to give reliable results. On the other hand, some of the features are very bright (X5 and SW2) and may be associated with embedded stellar sources.

Using the *StarFinder* code (Diolaiti et al. 2000) we also produced low-pass images containing the background emission. The result of the point source extraction largely depends on the size of the box (in units of a FWHM of the PSF) used for the background estimate. For small values of the box size (< 10), the background estimate is still contaminated by stars, and for values larger than 15 the compact features become diffuse. The brightest of the Northern Arm filaments, NE4, has a high enough S/N to be clearly detected in the background images. The background image is free from stars and therefore allows us to extract the NE4 feature without confusion. However, other NE and SW filaments cannot be clearly defined against the smooth background. Thus, only for the NE4 filament we additionally give the proper motion component along the extent of the feature. We performed the NE4 proper motion analysis for three different sizes of the box used for the background estimate (10, 13 and 15). The values given in Table 4.3.2 represent the average of the obtained results and the corresponding diagram in Fig 4.8 shows only the result for the box with a width of 13 PSF FWHM values. In Fig. 4.6 we show that the

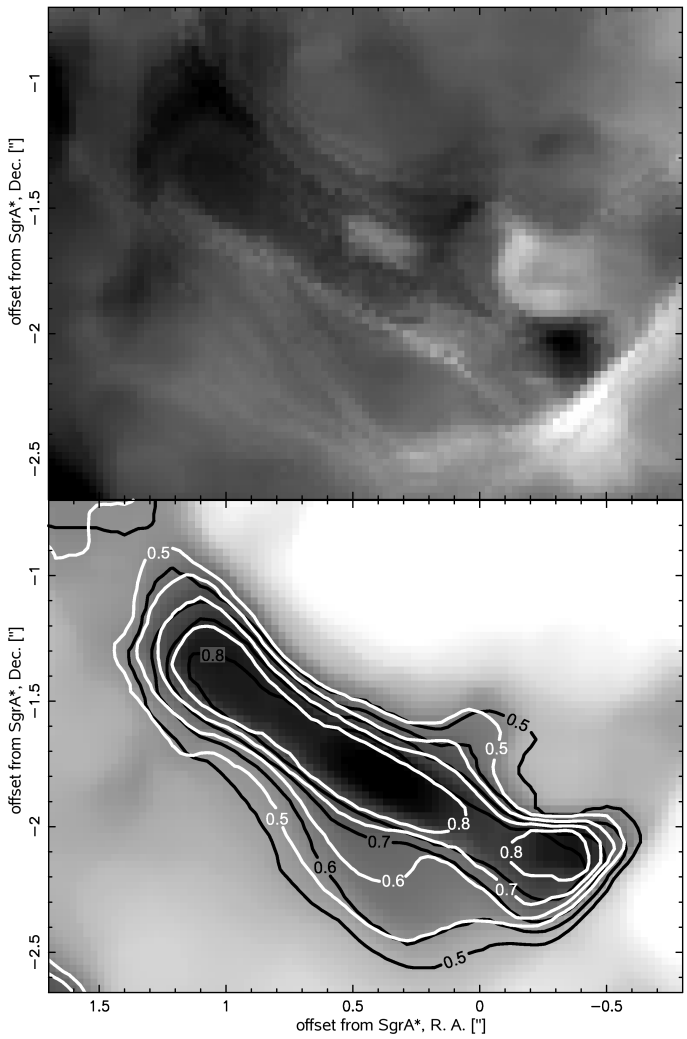

Figure 4.6: Top: *difference image of the area around the filament NE4, between the epochs 2006.408 and 2003.356. White pixels correspond to the later epoch, thus indicating the south-westward motion of the filament.*
Bottom: *gray-scale image of the same area (2003.356) with the contours corresponding to the 2006.408 (black) and 2003.356 epoch (white) overlayed. Contour levels correspond to the 50, 60, 70 and 80 % of the maximum intensity of the image (both images were previously scaled to have the same maximum intensity).*

motion towards the south west can already be seen but is hard to quantify from the difference image. From a comparison of contour plots the motion can be estimated to first order (Fig. 4.6). However, the actual value of the proper motion was derived using the cross-correlation method described above.

4.3 Results

4.3.1 Nature of the X features

The features denominated with X are most probably associated with stars. The images clearly show that the features X1, X5, and X6 are curved, with stars at the approximate centers of their curvature - this suggests that they are associated with these stars. X1, X5 and possibly X6 could be formed due to interaction between a stellar wind, probably in combination with the stellar motion, and the interstellar medium. They could be similar to the Northern Arm stellar bow-shocks discussed in Tanner et al. (2005), but associated with less massive sources. Feature X1 was already reported by Clénet et al. (2004). The authors interpret it as a bow-shock. For feature X5 no significant proper motion was detected, but taking into account the significantly higher brightness of this feature with respect to the other filamentary structures, we suppose that there is an embedded or background star at the same position. The feature X4 is associated with IRS 3, whose bow-shock appearance was discussed in Viehmann et al. (2005).

Along the line that connects Sgr A* and the feature X3 ($\sim$ 3.3" southwest from Sgr A*) at the position (-0.56", -0.55") from Sgr A*, one can notice feature X7, with a shape similar to that of X3. The faint star at this position in the K_S-band image is represented by a much more extended structure in the L'-band image (Fig. 4.7). Both X3 and X7 are approximately aligned (in projection) with Sgr A*. The line of symmetry of the X7 "V"-shape is oriented $\sim 40^o$ east of north and to within less than 5^o it is passing through the position of Sgr A*. The line of symmetry of X3 is slightly displaced from the line that connects it with Sgr A* ($\sim 5^o$) and is oriented $\sim 37^o$ east of north. The opening angle toward Sgr A* is $\sim 20^o$ for X7 and $\sim 10^o$ for X3. The orientation of both sources towards Sgr A* suggests an interaction with a possibly existing outflow from the central

region (see section 4.4.3). They may represent bow-shock-like features pointing back to the position of Sgr A* as a common origin of such an outflow.

4.3.2 Proper motions

Table 4.3.2 summarizes the proper motions of thin filaments obtained in our study. The proper motions have been successfully determined in 11 regions. In order to transform the angular motions into velocities we assume a distance to Sgr A* of 8 kpc. At this distance, 1 mas yr^{-1} is equivalent to 39 km s^{-1}.

Boxes in Fig. 4.9 mark the filaments that were analyzed. The directions of motion in the plane of the sky are represented by arrows. To emphasize that some of the motions shown in Fig. 4.9 do not contain the complete information about the motion in the plane of the sky, we represent them by different colors. The light blue arrows in Fig. 4.9 show the full proper motion of the corresponding feature, while the black ones represent only the component perpendicular to the feature of interest. A filled circle rather than an arrow at the position of the NE1 feature marks the insignificant motion of this feature. Note that for display purpose the dimensions of the boxes shown in Fig. 4.9 are different from those used for the extraction of the feature (as they are stated in Table 4.3.2). Diagrams in Fig. 4.8 contain detailed information about the results. The velocity difference Δv in Table 4.3.2 represents the 1σ uncertainty of the linear fit to the various epochs. Each offset is weighted by the corresponding uncertainty. The escape velocities were determined using the projected distance from Sgr A* with a mass of $3.6\times10^6 M_\odot$.

Feature X1 is associated with a star located (2.95", 3.46") from Sgr A*. The proper motion of the associated star is $v_{R.A.}$=(247±25) km s^{-1}, $v_{Dec.}$=(-46±5) km s^{-1} as derived from our L'-band data. We find that the feature is moving approximately in the same direction as the star apparently associated with it – this confirms the bow-shock interpretation of Clénet et al. (2004).

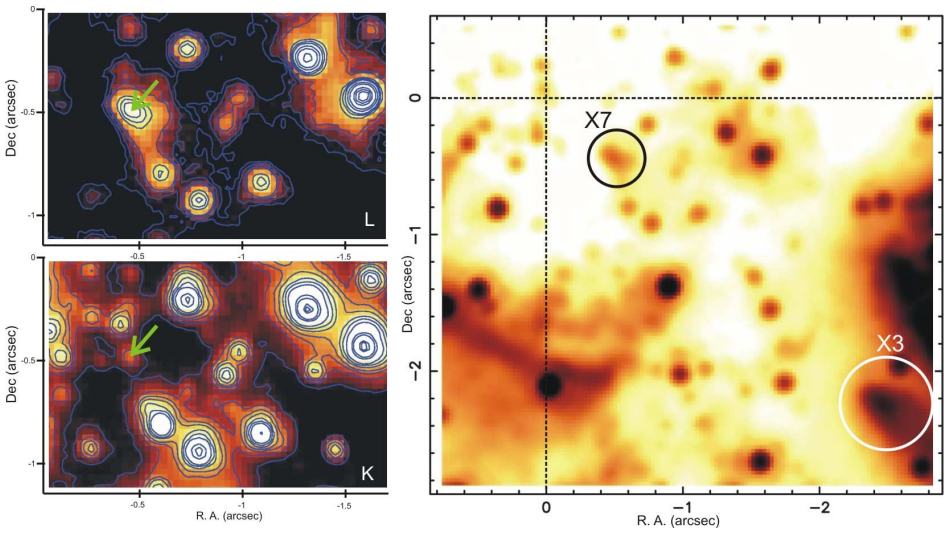

Figure 4.7: Left: *L'-band (top) and K_S-band (bottom) image of the small area southwest from Sgr A* that contains the feature X7 (axes show the offset from Sgr A*). Arrows mark X7 in the L'-band and a star at the same position in the K_S-band frame.* ***Right:*** *L'-band image containing X3, X7 and Sgr A*.*

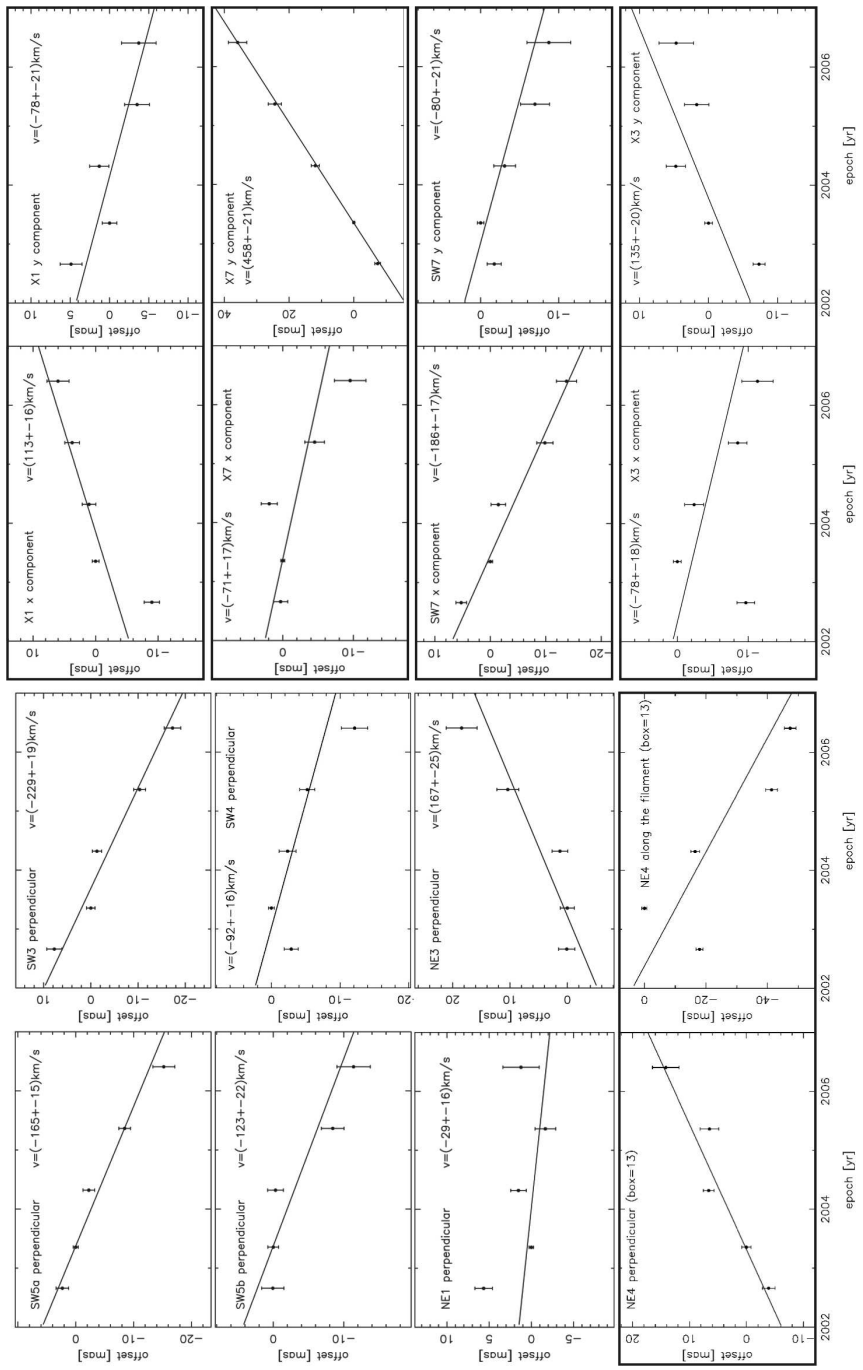

Figure 4.8: *Proper motions of thin filaments. The error bars show the 1 σ uncertainty of each measurement. The x and y components mentioned in graphs refer to R. A. and Dec., respectively.*

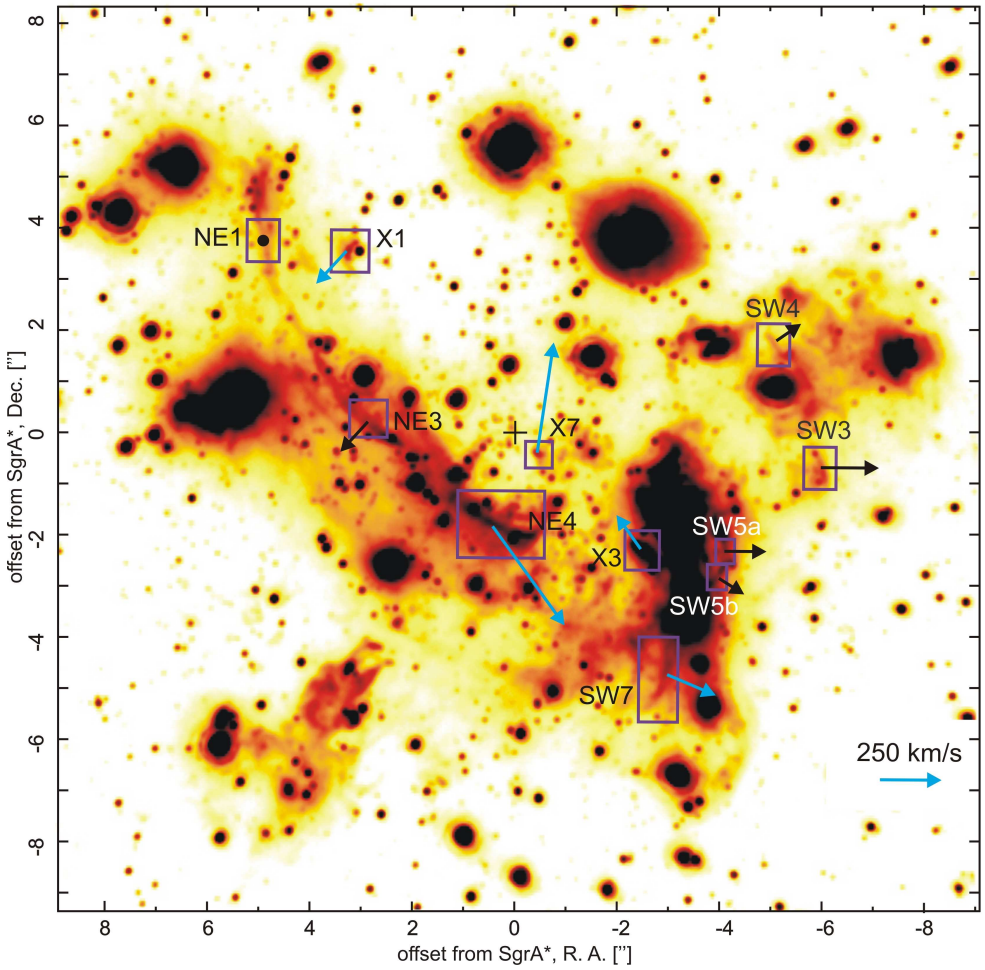

Figure 4.9: *L'-band image of the Galactic Center. Boxes mark thin filaments with measurable proper motions. Note that boxes in this image are different from those used for measurements (stated in Table 4.3.2). The arrows show proper motions of the thin filaments obtained in our study: light blue arrows stand for the features with measurable proper motion in both directions, while black arrows show only the proper motion component perpendicular to the feature (see the text for the explanation). The insignificant motion of the Northern Arm filament NE1 is marked with a circle rather than an arrow. The cross marks the position of Sgr A*.*

Table 4.1: *Proper motions of thin filaments*

feature	$\Delta\alpha$ [a] (arcsec)	$\Delta\delta$ [a] (arcsec)	$size(\Delta x \times \Delta y)$ [b] (arcsec×arcsec)	v [c] ($\mathrm{km\,s^{-1}}$)	Δv ($\mathrm{km\,s^{-1}}$)	ϕ [d] (°)	v_{esc} ($\mathrm{km\,s^{-1}}$)
NE1	4.76	3.42	0.32×0.46	-29	16	90	368
NE3	2.62	-0.09	0.38×0.41	167	25	140	550
SW3	-6.08	-0.77	0.35×0.35	-229	19	270	360
SW4	-5.07	1.76	0.43×0.38	-92	16	305	404
SW5a	-4.20	-2.31	0.35×0.11	-165	15	270	407
SW5b	-4.13	-2.75	0.16×0.24	-123	22	240	400
NE4 (R.A.)	0.50	-1.63	2.51×1.97	-386	76		682
NE4 (Dec.)				-280	55		
NE4 (along)				-436	103	240	
NE4 (perp.)				194	11	150	
SW7 (R.A.)	-3.07	-5.10	0.73×1.22	-186	17		365
SW7 (Dec.)				-80	21		
X1 (R.A.)	3.22	3.40	0.30×0.38	113	16		412
X1 (Dec.)				-78	21		
X7 (R.A.)	-0.56	-0.55	0.54×0.41	-71	17		1006
X7 (Dec.)				458	21		
X3 (R.A.)	-2.45	-2.37	0.46×0.43	-78	18		483
X3 (Dec.)				135	20		

[a] relative to Sgr A*; position of the center of the box

[b] size of the image section used for cross-correlation

[c] velocities of all NE and SW features, except that of SW7 and NE4, are in a direction approximately perpendicular to the feature. Other proper motions are given both in R. A. and Dec. direction. In case of NE4 we additionally give the velocity along the feature and perpendicular to it. The positive sign in the velocity refers to the eastward motion in R.A. and northward in Dec. For the perpendicular component the positive sign marks the predominant eastward motion. The negative sign for the motion of the NE4 along the filament marks the predominant southward component.

[d] the position angle of the velocity vector for the features with a proper motion measured in the direction perpendicular to the feature. The angle is measured east of north.

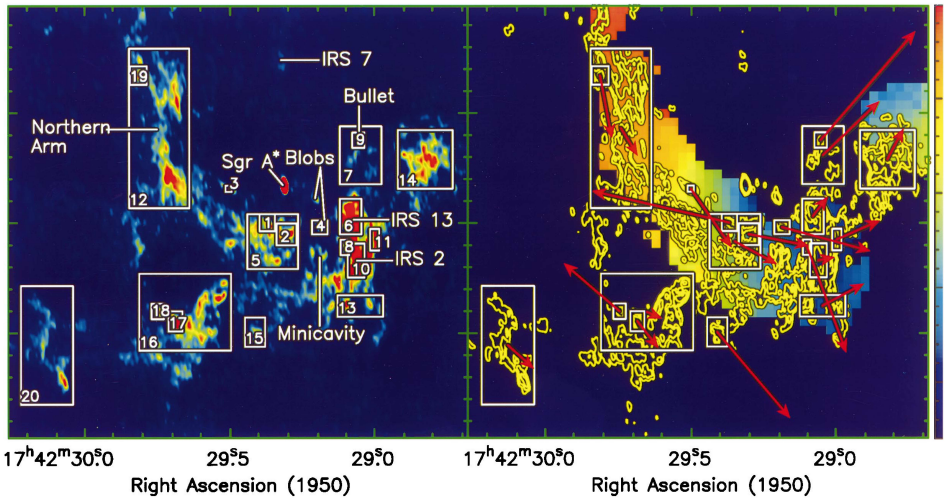

Figure 4.10: *Left: Pseudo-color image of the $\lambda = 2\,cm$ continuum from the 1990 epoch data with a resolution of $0.1'' \times 0.2''$ and a rms noise of $0.104\,mJy\,beam^{-1}$ (Yusef-Zadeh et al. 1998). The boxes, except box 21, are regions in which proper motion measurements have been carried out with a greater than 3σ level detection in at least one direction. Right: H92α velocity distribution with spectral and spatial resolutions of $14\,km\,s^{-1}$ and $0.75'' \times 1.2''$ presented in pseudo-color with contours of the $\lambda = 2\,cm$ continuum image superposed.*

4.3.3 Comparison to Radio Measurements

Yusef-Zadeh et al. (1998) presented radio continuum observations at $\lambda = 2\,cm$ (Fig. 4.10) and calculated proper motions of ionized gas at the Galactic Center. Although no thin filaments similar to those detected in NACO L'-band images are detected in the radio continuum images, some comparison can be done. The filamentary ionized structure connecting IRS 13 and IRS 2 (Box 11 in Yusef-Zadeh et al. 1998) coincides with the SW5 feature in our images (in this work divided in two parts, SW5a and SW5b, because of the presence of a star). A westward direction of motion is obtained from both measurements, but the value of this component obtained from the radio continuum is larger ($v_{R.A.}$=(-329±56) $km\,s^{-1}$). The reason for this discrepancy is not clear. It is possible that at different wavelengths we are actually probing different material. Zhao & Goss (1998) also performed radio continuum observations at 7

and 13 mm and calculated proper motions of 57 compact H II components. As in the previous case, the only comparable structure is SW5 ("loop" in their notation), but the results are not in good agreement with ours. This feature, in the measurements of Zhao & Goss (1998), is divided in several non-consistently moving components, which is probably consequence of the granular substructure seen in the radio image (probably due to a low signal to noise ratio). In our IR continuum images the structure is well defined.

Yusef-Zadeh et al. (1998) report an anomalous high-velocity feature, so-called "bullet", at the offset (-3.39", 2.065") from Sgr A* in the 1990 epoch. Approximately at this position in the L'-band images one can notice a dusty feature (see Fig. 4.9). However, given the high velocity quoted for the bullet it should have moved by $(\Delta\alpha, \Delta\delta) = (0.30", 0.34")$ to the northwest from 1990 to 2006, which is the epoch of the image in Fig. 4.9. No similar feature can be found at the corresponding position in the 2006 epoch, or close to it. Although the feature we see in the L'-band cannot be disentangled from the rest of the material and therefore we are not able to measure its proper motion, a simple inspection of images at different epochs shows that it does not seem to have a significant velocity compared to the bullet. Therefore, we cannot identify this feature as the bullet.

4.3.4 Orbits of the diffuse gas

The overall kinematic properties of the Northern Arm and Bar section can be modeled as a single gas streamer orbiting Sgr A*. Such a model can be constrained via the radial velocity information from the H92α (Roberts & Goss 1993) and [Ne II] line (Lacy et al. 1991; Vollmer & Duschl 2000) as well as the overall distribution of the gas and dust along these features. Proper motions of ionized gas were in detail studied by Yusef-Zadeh et al. (1998). They additionally give the radial velocities as measured by Roberts & Goss (1993) and Roberts et al. (1996). According to Yusef-Zadeh et al. (1998) the predominant component of the motion in the plane of the sky is from east to west. The flow of gas in the Northern Arm follows its elongated shape: from the north-east with slightly redshifted velocities it follows the orbital trajectory to the southwest as it crosses the plane of the sky. The ionized gas passes south of Sgr A* before it moves to the northwest. The complex velocity structure

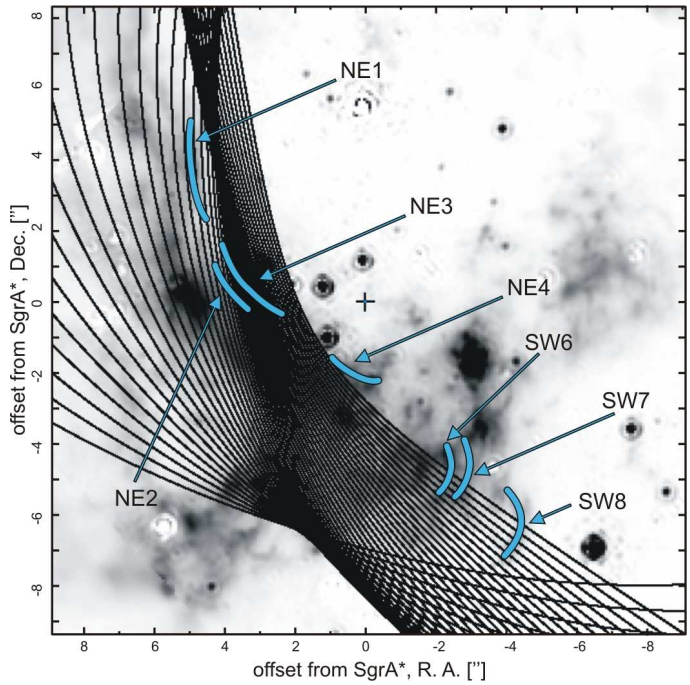

Figure 4.11: *The Paα map with the Keplerian orbits overplotted (Paumard et al. 2004). We additionally sketch some of the L'-band narrow filaments, showing that none of the orbits is aligned with the Northern Arm filaments.*

of the mini-cavity, however, fails to be explained by such a simple model. Similar results are reported by Paumard et al. (2004) based on He I and Br γ observations. At the position of the NE1 filament the line emission is slightly red shifted (40-60 $\mathrm{km\,s^{-1}}$) while at the positions of the other Northern Arm filaments the radial velocity becomes negative. At the position of NE3 the line emission is blue shifted by 40-60 $\mathrm{km\,s^{-1}}$ and close to NE4 by more than 130 $\mathrm{km\,s^{-1}}$. The Bar material at the position of Sgr A* and within few arcseconds south of it has radial velocities close to 0 $\mathrm{km\,s^{-1}}$. The emission becomes blue shifted as we move further to the west (where SW3 and SW4 are located).

Paumard et al. (2004) analyzed the Northern Arm as a Keplerian system in the gravitational field of Sgr A*. They fit a bundle of Keplerian orbits in order to model the full velocity field of the Northern Arm. The authors interpret the rim of the Northern Arm in terms of line-of-sight orbit crowding. The western edge facing Sgr A* is the region that shows the highest density of crowded orbits (see Fig. 8 in Paumard et al. 2004). In order to construct Fig. 4.11 we used the part of the Fig. 8 in Paumard et al. (2004) having the same field of view as the L'-band images presented in this work.

4.3.5 Stability of the filamentary structures

The nature of the observed thin features, especially the SW and NE filaments, is unclear. One possible interpretation is that they are the consequence of the interaction of a central wind originating from the hot stars and/or possibly from Sgr A*. While the origin and the mechanisms of such a wind will be discussed later in the text, here we concentrate on the effects it would have on the mini-spiral material in combination with the dominating gravitational potential of the central black hole.

We favor a scenario in which the proposed wind compresses gas and dust in the mini-spiral and forms the observed filaments. For the SW filaments this interaction could have taken place at the western edge of the mini-cavity. The thin Northern Arm filaments may have been generated by a wind in the opposite direction of the mini-cavity. For the mini-spiral Vollmer & Duschl (2001) quote a sound speed of v_s=7.6 $\mathrm{km\,s^{-1}}$. This velocity is very small in comparison with the overall motion of the Northern Arm (Paumard et al. 2004;

Yusef-Zadeh et al. 1998). Also, once formed, the filaments may still be influenced by wind from the central few arcseconds that may keep them confined. The magnetic field of the Northern Arm, as reported by Aitken et al. (1991) and Aitken et al. (1998), could also play a role in confining ionized gas and charged dust grains along the filaments.

If we assume a temperature of T = 7000K for the mini-spiral material (Roberts & Goss 1993) then the average velocity of a hydrogen atom associated with thermal energy is v=$(3kT/m)^{1/2} \approx 13\,km\,s^{-1}$. At some position in the Northern Arm it takes approximately 250 yr for it to cross the distance equivalent to the width of a filament that we can resolve (∼100 mas). During this time the filament can drift ∼2.5" southwards due to the motion of the mini-spiral material in the central gravitational potential. For dust particles it takes even longer to cross the equivalent width of a filament due to their thermal motion. This leads to the conclusion that a filament formed in the Northern Arm of the mini-spiral will have a lifetime that is long enough to drift to the southwest together with the gas stream. Once formed, the dominant source for their destruction will be the interaction with their surrounding turbulent medium. Judged from the line widths of the H92α emission (Roberts & Goss 1993) the velocity dispersion of the gas within the mini-spiral is of the order of 50 $km\,s^{-1}$. Vollmer & Duschl (2000) assume a maximum value for the velocity dispersion of 40 % of the Keplerian velocity.

In order to investigate the kinematic behaviour of linear features formed in a central potential we carried out orbit simulations. We assumed a dominating central potential from a $3.6 \times 10^6\,M_\odot$ black hole at the position of Sgr A*. Schödel et al. (2007) estimate that the gravitational field at the Galactic Center is dominated by the point mass of the black hole inside a projected radius of about 6". Since all of the measured filaments are either inside or just at the border of this circle, we do not take into account the possible contribution of the stellar cluster to the gravitational potential. In agreement to similar calculations by Vollmer & Duschl (2000) and Paumard et al. (2004) we chose 3 test particles with velocities of $v_{R.A.} = 20\,km\,s^{-1}$, $v_{Dec.}$ = -150 $km\,s^{-1}$ and v_{LOS} = -100 $km\,s^{-1}$ launched from locations around $\alpha_{relative}$ = 220 mpc =5.6", $\delta_{relative}$ = 250 mpc = 6.4" and z_{LOS} = 150 mpc (see Fig. 4.12). Here z is the distance behind the plane of the sky including Sgr A*. The corresponding orbits show that elongated thin features "imprinted" into the Northern Arm are subject to

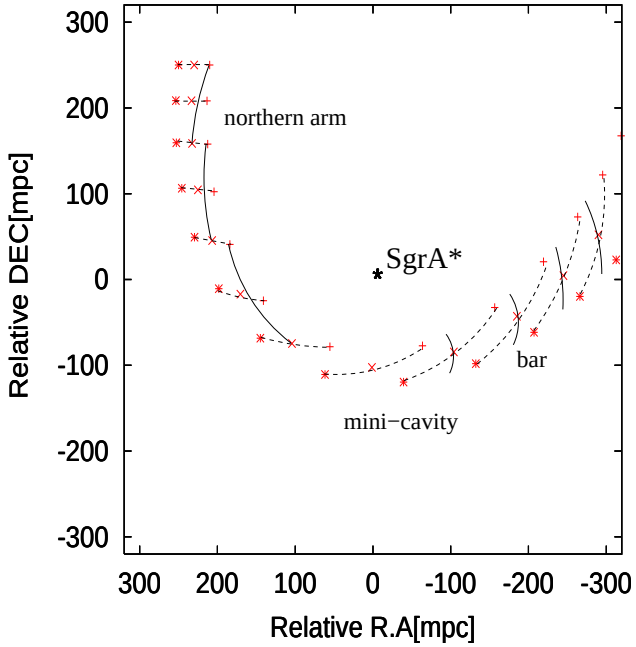

Figure 4.12: *Results of our 3D dynamical model calculation. Three particles (marked +, x and *) have been placed within the mini-spiral with locations and velocities consistent with our current knowledge. See text for further explanation. The dashed lines connect particles launched at equal times. The time between the sets of symbols is* $\sim 250\,yr$*. The solid lines represent the observed narrow features (i.e. shock fronts or contact surfaces) and how they evolve while traveling along the Northern Arm/Bar region. A filament formed at some position in the Northern Arm or Bar is slightly changing the shape while drifting with the rest of the material, but preserves its filamentary appearance.*

a weak shear but to first order keep their original structure while drifting to the south. In our current picture Northern Arm filaments drift south (while being stretched by less than a factor of 2 within the Northern Arm) until they reach the mini-cavity region where they may be destroyed. Filaments created at the western edge of the mini-spiral drift westward along the Bar.

From Fig. 4.11 one can clearly see that the Northern Arm filaments cannot be simply explained as the consequence of orbit-crowding as suggested by Paumard et al. (2004). A comparison with the velocity field obtained from their model shows a good agreement for the perpendicular velocity component of the filaments NE1 and NE3 (within a 1σ error for NE1 and 2σ for NE3). This supports the assumption that the observed filaments are really drifting southwards together with the Northern Arm material. However, none of the orbits actually follows the shape of the filaments and therefore the proper motions of the gas as stated in Paumard et al. (2004) are not aligned with the extent of the filaments. Thus one needs to include an additional force that could form the filaments, keep them confined and prevent them from being destroyed by the bulk gas flow. This is especially valid for the filament NE3. The exact position of the filament NE4 does not coincide with any of the Keplerian orbits fitted by Paumard et al. (2004). They find that the Northern Arm is split into two layers as it reaches the mini-cavity. The mini-cavity itself is a part of the first layer, while the second layer is deflected northward from it and seems to contain the filament NE4. Concerning the SW filaments, our study shows that the proper motion components perpendicular to their extent are consistent with the motion in the dominating central potential, but we are still facing the question of their formation. As proposed earlier in this section, they could have been formed by an interaction at the western edge of the mini-cavity, and then drift westwards together with the rest of the mini-spiral material.

Concerning the possibility that the filaments are the consequence of an interaction between a fast wind and the mini-spiral material, we can try to predict the width of a shock using formula for the shock front cooling distance (Hartigan et al. 1987):

$$d = 12\Big(\frac{v_s}{100kms^{-1}}\Big)^{4.67}\Big(\frac{100cm^{-3}}{\eta}\Big)AU \tag{4.3}$$

Assuming shock velocities $v_s \sim 100 - 200\,\mathrm{km\,s^{-1}}$ and a density of the pre-shock medium $\eta \sim 10^3\mathrm{cm}^{-3}$, we get the cooling distance of the shock to be

$\sim 30\,\mathrm{AU} \sim 4\,\mathrm{mas}$, much smaller then the resolution of the current observations.

Since the motions of the Northern Arm filaments fail to be completely explained simply by gravitational influence, one has to include additional forces that could drive the observed motions. In the next section we consider the winds at the Galactic Center as the main candidates.

4.4 Winds at the Galactic Center

4.4.1 Evidence for an outflow from the central parsec

As we have seen in Chapter 2, the He-stars supply $\sim 3{\times}10^{-3}\mathrm{M}_\odot\,\mathrm{yr}^{-1}$ of material to the center. The amount of gas available for accretion onto Sgr A* at the Bondi radius is estimated to be $\lesssim 10^{-5}\,\mathrm{M}_\odot\,\mathrm{yr}^{-1}$ (Quataert 2003; Baganoff et al. 2003). The actual mass accreted onto Sgr A* is up to 2 orders of magnitude lower, as determined by the linear polarization measurements at 230 GHz (Bower et al. 2003; Marrone et al. 2006). We can see that about 99 % of the material from stellar winds does not even get close to the Bondi radius and must therefore escape the central arcseconds in form of a wind. Blandford & Begelman (1999) point out that for accretion rates well below the Eddington rate most of the gas accretes with positive energy and may escape. Therefore they propose a solution (ADIOS; adiabatic inflow-outflow solution) in which most of the gas is lost through winds and only a small fraction of the gas is actually accreted onto the black hole. This is also in agreement with the RIAF theory (radiatively inefficient accretion flow; see e.g. Yuan 2006) that postulates strong outflows from Sgr A*. The outflow may be partially collimated in form of a jet. Jet and shock models (see Markoff & Falcke 2003; Melia & Falcke 2001) as well as accretion from an in-falling wind due to the surrounding cluster of mass-losing hot stars (e.g. Coker et al. 1999; Yuan et al. 2002) are discussed to explain the radio to X-ray properties of Sgr A*.

There is some observational evidence for outflows in the central parsec as well. The "mini-cavity" region 3.5" southwest of the compact radio source Sgr A* was first pointed out on cm-radio maps by Yusef-Zadeh et al. (1990). The strong Fe[III] line emission (see Fig. 4.13) seen toward that region (Eckart

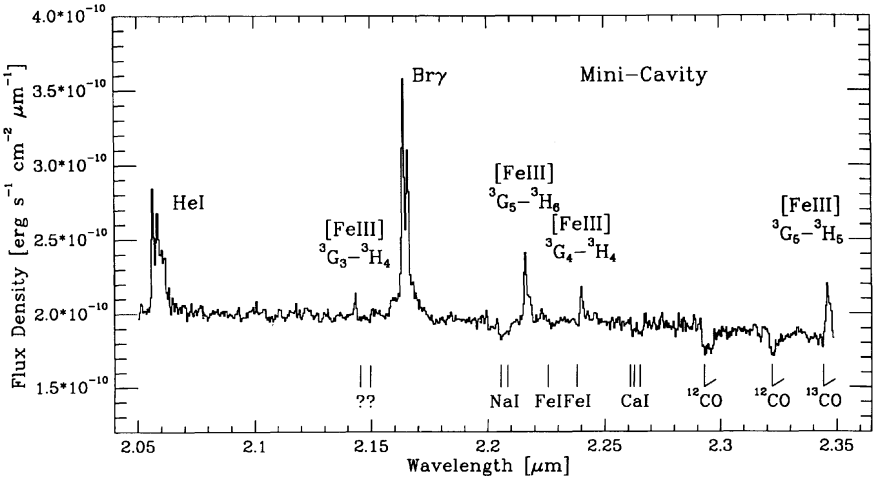

Figure 4.13: *K-band spectrum of the Galactic Center mini-cavity. The cavity is emitting strong narrow emission lines of H, He I, and Fe [III]. Broad components of He I 2.06 μm and Brγ originate in He I emission-line stars. A contribution of late-type stars to the observed continuum is indicated by characteristic absorption features. Image from Lutz et al. (1993).*

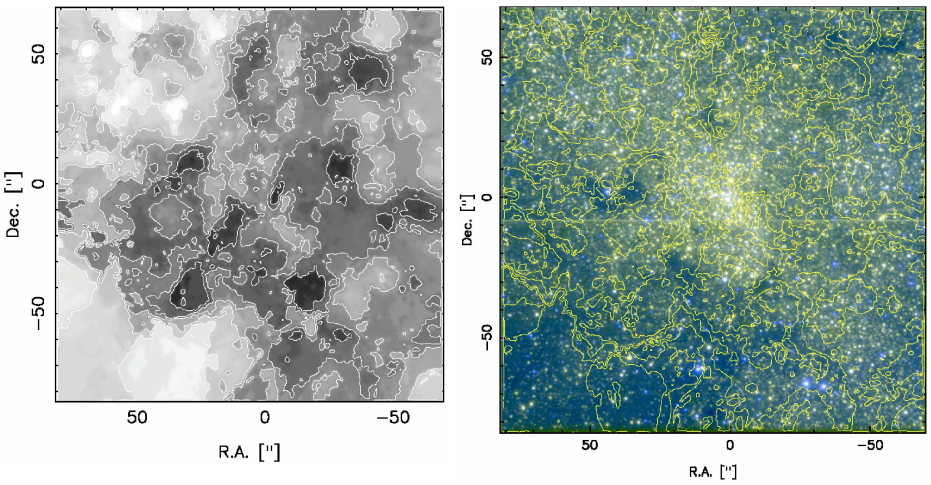

Figure 4.14: ***Left:*** *Extinction map derived from the H-band and 2.09 μm images of the central stellar cluster with ISAAC/VLT. Contours are plotted for $A_K = 1.8$ - 3.6 in steps of 0.3. Darker shades correspond to higher extinction.* ***Right:*** *The extinction contours from the left panel plotted over the combined J and K false colour image. Image from Schödel et al. (2007).*

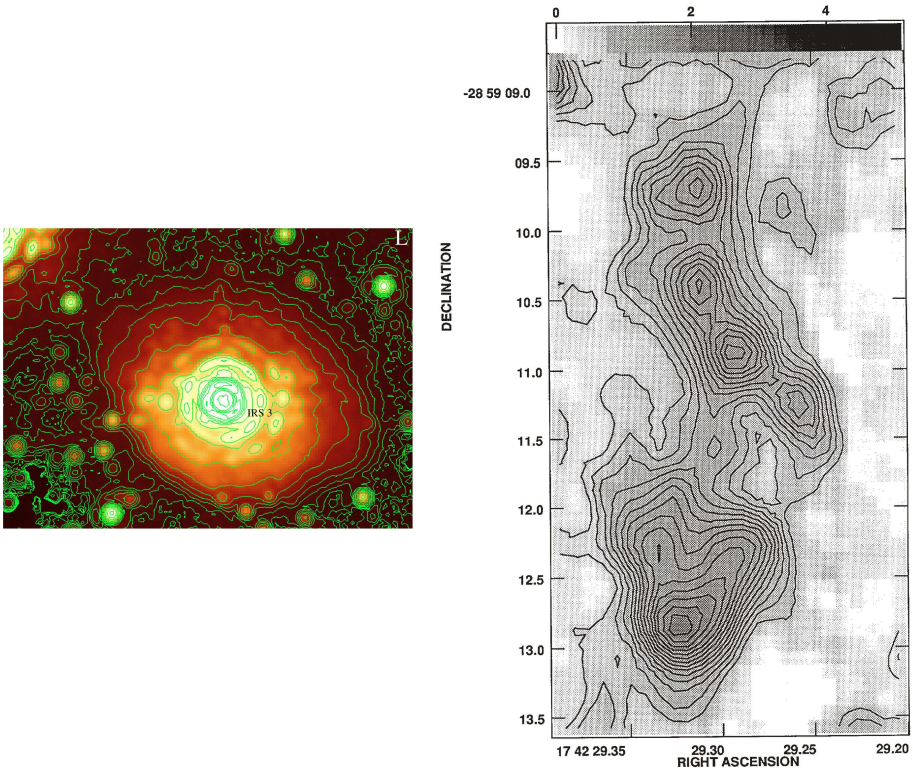

Figure 4.15: Left: *L'-band view of IRS 3 with NACO (Viehmann et al. 2005). The bow-shock shape is consistent with the stellar dust shell being pushed northwest by wind from the direction of the IRS 16 cluster and Sgr A*.* ***Right:*** *VLA image of IRS 7 (Yusef-Zadeh & Melia 1992). The apex of the bow-shock is facing toward the IRS 16 cluster. The authors conclude that the shape of the shock results from the collision between the wind from the direction of IRS 16 and the IRS 7 stellar wind, rather than from the motion of the star through the ISM.*

et al. 1992; Lutz et al. 1993) is consistent with gas excited by a collision with a fast ($\geq$1000 km s^{-1}) wind from a source within the central few arcseconds (Yusef-Zadeh & Wardle 1993; Yusef-Zadeh & Melia 1992). Most recently Schödel et al. (2007) present an extinction map of the central parsec. In this map (Fig. 4.14) an extended region of low extinction, centered on Sgr A* runs in NE-SW direction across Sgr A* and is continued in the mini-cavity. It supports the assumption of an outflow from the central arcseconds. For one of the most prominent dust embedded sources, IRS 3, Viehmann et al. (2005) find that the extended L- and M-band continuum emission has a characteristic bow-shock shape. A possible explanation for its asymmetric appearance is that IRS 3 consists of a mass-losing star surrounded by a very thick, extended dust shell, which is pushed northwest by a wind from the direction of the IRS 16 cluster and Sgr A* (Pott et al. 2008). Similarly to the north, the mass-losing envelope of IRS 7 appears to be influenced by a strong central wind (Yusef-Zadeh & Melia 1992).

There is a body of observational evidence that supports the interaction of a wind with the local ISM as well as with stars in the central parsec. Some of those were already presented in the introduction (mini-cavity, IRS 3, IRS 7, low extinction region). Then, the features presented in this work: the narrow filaments could be the contact surfaces between the wind and the mini-spiral material. The "V"-shaped sources X3 and X7 are supporting the Sgr A* wind scenario (see section 4.4.3).

The main candidates for the source of the central outflow are the high-mass-losing stars at the center. Alternatively, the outflow could be due to a jet-like structure directly associated with the black hole at the position of Sgr A*. Some of the theoretical models that successfully fit the observational data include such a jet (e.g. Falcke & Markoff 2000; Yuan et al. 2002). In Section 4.5 we consider the possibility that the outflow could, in fact, be partially collimated.

4.4.2 Stars as the source of the outflow

Most of the above mentioned bright and massive He-stars are located within a single plane and most of them within a radius of 0.1 pc (2.5") from Sgr A*

(Genzel et al. 2000, 2003; Levin & Beloborodov 2003), forming a disk of clockwise rotating stars (CWS). Paumard et al. (2006) largely expand the sample of stars belonging to the CWS disk, and also propose the existence of a second, less populated stellar disk containing counter-clockwise rotating stars (CCWS; see also Genzel et al. 2003). According to Paumard et al. (2006) most of the bright stars in the IRS 16 complex are part of the clockwise system, including IRS 16C and IRS 16SW. Since the bright He-stars in the CWS are also those that show clear indications for P Cygni profiles we assume that the stars in this disk are also the predominant source of mass loss in the central parsec. Since the geometry of the CWS plane is such that the rotational axis is inclined towards the observer, the bright He-stars to the north and northeast of Sgr A* are located on the far side of the disk (i.e. IRS 16C, IRS 16CC, E29, E38; Beloborodov et al. 2006). Therefore they must be as close to the Northern Arm - which is passing by the IRS 16 cluster from behind - as the IRS 16 cluster is with respect to the mini-cavity. It is therefore likely that their stellar wind may have a similarly strong effect on the Northern Arm as it may have towards the mini-cavity.

4.4.3 Stellar probes of the wind from the direction of Sgr A*

A particularly interesting feature in this context is feature X7. Despite the high velocity component to the northwest, the cometary or bow-shock-like shape of the feature is pointing approximately toward Sgr A*. The wind from the direction of Sgr A* could be responsible for this shape. If the star is moving within an area with no significant amounts of ISM then any supersonic wind from the direction of Sgr A* could easily produce such a shape. If the amount of the ISM is not negligible then the wind should have a much higher velocity than the observed velocity of the feature. Taking into account the slight displacement of the line of symmetry of X7 from the line that connects it with Sgr A*, a simple calculation tells us that the velocity of the wind from Sgr A* should be at least one order of magnitude higher than the velocity of the feature. In addition, approximately along the same line that connects Sgr A* and X7, lies the feature X3 with a same type of a cometary appearance (see Fig. 4.7). The alignment of X3 and X7 with Sgr A*, and the shape of both features, give a strong support to the central outflow hypothesis. Recent VLT NACO K_S-band polarization measurements (Meyer et al. 2006b) have shown that source X7 is

also polarized by 30±5% along a position angle of -34^o±10^o. Assuming that the polarization is due to Mie scattering of a non-spherical dust distribution then an overall direction of the bow-shock's symmetry axis is 56^o±10^o. This includes the direction towards Sgr A* (see the description of data acquisition and calibration in Eckart et al. 2006 and Meyer et al. 2006b).

4.5 A partially collimated outflow?

4.5.1 H_2 emission from the CND lobes

Gatley et al. (1984, 1986); Burton & Allen (1992) and Yusef-Zadeh et al. (2001) report H_2(1-0) S(1) molecular hydrogen line emission from the CND that is concentrated on the northern and southern lobes (see Fig. 4.16). Based on HST NICMOS and ground based data and adopting a lower limit to the extinction toward the lobes of A_K=3 (Scoville et al. 2003), Yusef-Zadeh et al. (2001) derive the extinction-corrected peak line intensity from the lobes as approximately to be about a factor η_1=3-4 higher than the mean surface brightness of the CND. The source of excitation of the H_2 emission associated with the CND is unclear. Most commonly it is assumed that the ∼70^o inclination of the 0.5 pc thick CND torus toward the line of sight will produce the north and south lobes by limb brightening of the ∼0.5 pc torus (e.g. Gatley et al. 1986; Burton & Allen 1992; Yusef-Zadeh et al. 2001). As summarized by Yusef-Zadeh et al. (2001), neither the intense UV filed combined with the high densities, nor the shock processes due to isotropic wind originating from the hot stars at the central parsec, can explain such a high intensity of molecular hydrogen emission on the CND lobes. The latter consideration shows that the ram pressure of an isotropic wind from IRS 16 cluster would be at least a factor η_2=5 too low compared to what is required.

4.5.2 Model

In this section we consider the possibility that the outflow originating from the central part of the Galaxy, presumably from the cluster of high mass losing

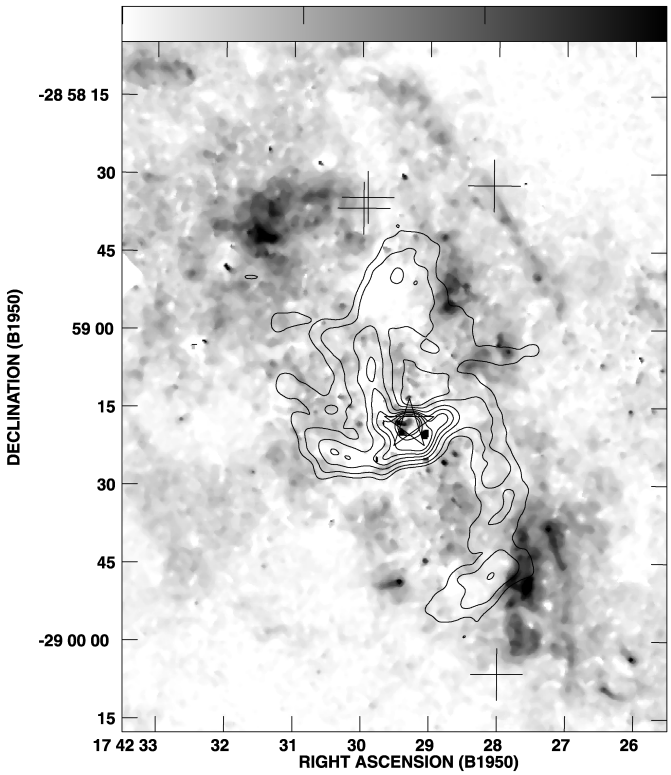

Figure 4.16: *Contours of 6 cm radio emission from the mini-spiral superimposed on a gray-scale NICMOS image of the H_2 1-0 S(1) line emission from the CND. The star shows the position of Sgr A*. Image from Yusef-Zadeh et al. (2001).*

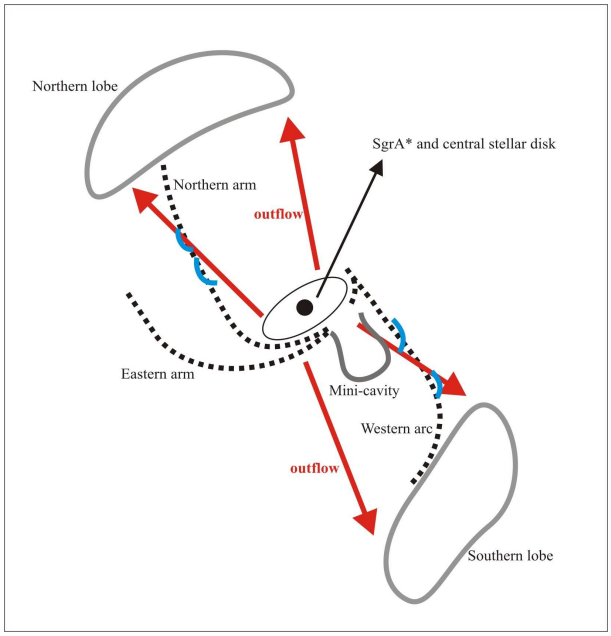

Figure 4.17: *Sketch of the outflow model. Collimated outflow originating from the mass-losing stars cluster and possibly the black hole at the position of Sgr A* could, in the interaction with the material of the mini-spiral, explain the geometry and motions of the thin filaments. This model suggests that northern and southern lobes of the CND are associated with the outflow.*

stars, with a possible contribution from the massive black hole itself, might actually be partially collimated. In the case of the existence of a wind from Sgr A*, the collimation would have to be seen as a consequence of the yet unexplained accretion process onto the black hole but could be linked to the plane in which the mass-losing He-stars are moving in. This motion within a single plane implies that the viscous friction of gas being blown into that plane is larger than that for gas being blown out perpendicular to it. On the one hand that results in a pressure gradient perpendicular to the plane, on the other hand it will result in an accretion flow within that plane onto the central black hole and may give rise to a corresponding outflow perpendicular to it. So both the ordered motion of the mass-losing stars as well as the resulting structured accretion flow may result in a combined, possibly collimated outflow.

This scenario would also explain the bow shock "tail" of the IRS 7 and

the northern and southern lobes within the CND to be associated with the outflow. If we assume that the H_2 line emission from the lobes is dominated by the interaction with a collimated wind rather than an approximately isotropic stellar wind from the central few arcseconds then - due to the limited size of the two lobes in the CND - a geometrical concentration of the outflow over an isotropic flow by a factor α∼50 has to be taken into account. We note that such an outflow could also have a grazing incident onto the CND (see Fig. 4.18). In this case the opening angle could be larger and the compression factor smaller. We also infer the lower limit on the collimated outflow velocity from the fact that NE1, the northern most filament, has an insignificant proper motion perpendicular to its extent and that filaments NE3 and NE4 which are likely to be more affected by the IRS 16 cluster wind have proper motion velocities of v_{pm}∼150 km s^{-1}. When generated in the Northern Arm at angular distances of 3 to 7 arcseconds from the IRS 16 cluster or Sgr A* and taking v_{pm} as an upper limit of the proper motion inferred by a collimated outflow, then a lower limit to the velocity of that flow with a total opening angle of α_{open}=20^o-30^o may be of the order of $v_f \sim v_{pm}/\tan(\alpha_{open}/2) \sim$ 500-900 km s^{-1}. The total required mass-loss carried by the collimated outflow is then

$$\dot{m}_{flow} = \frac{\eta_1 \eta_2}{\alpha} \frac{v_s^2}{v_f^2} \dot{m}_{stellar} \leq 10^{-3} M_{\odot} yr^{-1} \quad . \tag{4.4}$$

This implies that such an outflow can easily be driven from the mass loss wind of the stellar cluster, that is blown away from the stellar disk or Sgr A* itself, rather than being accreted onto Sgr A*.

Whether in the presence of the deep central potential provided by the 3.6×10^{6}M$_\odot$black hole the wind contribution is dominated by the stars or by Sgr A* has to be investigated via detailed hydro-dynamical model calculations. In the context of the mini-cavity such calculations have been carried out by Melia et al. (1996) and more recently by Cuadra et al. (2006). The authors have shown that the structure, kinematics, and luminosity of the mini-cavity are consistent with a model in which a few 10^{6}M$_\odot$black hole interacts with an ambient 500-700 km s^{-1} Galactic Center wind originating within the IRS 16 cluster. It accretes a small portion of it and then may expel the rest in form of a collimated flow toward the mini-spiral streamer (Melia et al. 1996). The filaments along the Northern Arm presented here, the shape of the Northern Arm, as well as the approximate alignments between the rotation axis of the

He-star disk and the connecting line between the northern and southern lobes in the CND (see references given above) present evidence for a similar collimated flow to the northeast.

4.5.3 3-Dimensional Orientation

In the following we discuss the space orientation of the main structures at the Galactic Center, as well as the orientation of the proposed outflow.

The observed geometry in the plane of the sky is such that the Northern Arm filaments and the mini-cavity are on almost opposite sides and on a well defined connection line through Sgr A*. This line also coincides with the strip of low extinction presented by Schödel et al. (2007). The wind that we consider responsible for the filaments along the Northern Arm and the formation of the mini-cavity as well, is strongly interacting with the gas in the gas disk (i) presented by Vollmer & Duschl (2000). This disk contains the Northern Arm and the part of the Bar, and connects well with the CND at an inclination of $\sim 30^o$ to the line of sight. The disk (i) is inclined $\sim 25^o$ to the line of sight and has the position angle of 28^o on the sky (N to E). Both CND and the Northern Arm are at a relatively low inclination to the plane of the Galaxy (Vollmer & Duschl 2000; Paumard et al. 2004). Thus we conclude that the wind could in fact be collimated with an opening angle of the order of 30^o or less. Another indication for an outflow to the northeast comes from the wavy structure of the Northern Arm. Here Yusef-Zadeh & Wardle (1993) already noted that the distortions of the arm are produced by ram pressure of the wind incident on the surface of the arm and inducing there Rayleigh-Taylor or Kelvin-Helmholtz instabilities.

The position angle of the outflow projected on the sky is close to that of the galactic plane. This would also be in good agreement with the extent of the northern and southern lobes in the H_2 emission of the CND. These lobes are located at the outer tips of the projected ellipse of the rotating CND. Therefore the lobes must be located approximately within the plane of the sky and within the Galactic plane.

This comparison also shows that the rotation axis of the hot He-stars (Genzel et al. 2000, 2003; Levin & Beloborodov 2003; Paumard et al. 2006) and the

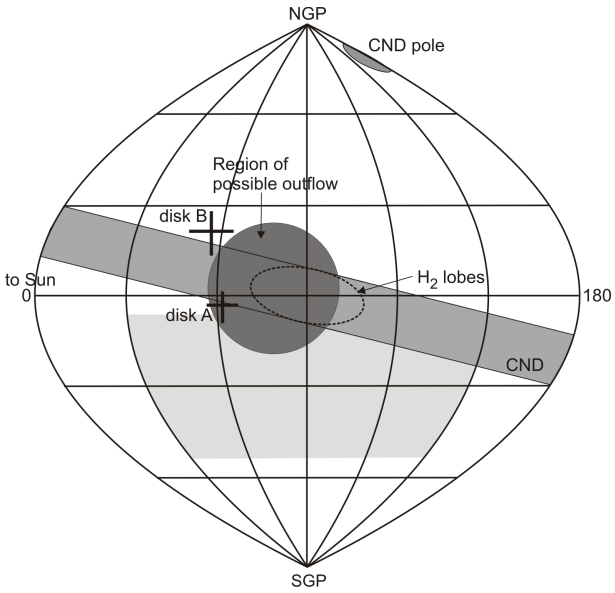

Figure 4.18: *Positions of main features at the Galactic Center as seen by an observer at the center of the Galaxy. Two crosses indicate the normal to the clockwise stellar disk plane: disk A as found by Levin & Beloborodov (2003) and disk B by Paumard et al. (2006). The large light-gray-shaded area south of the galactic plane represents the results from NIR polarization measurements as presented by Eckart et al. (2006) and Meyer et al. (2006a,b). Here we only show the direction towards the Northern Arm. The dark-gray-shaded area close to the center of the plot outlines the approximate direction of a possible collimated outflow that could explain our observations plus the H_2 results by Gatley et al. (1984, 1986); Burton & Allen (1992) and Yusef-Zadeh et al. (2001). Such an outflow would also be in agreement with mass-loss from the the stellar disks and the recent polarization data (see references above).*

axis of the outflow may in fact be aligned to within less then 30^o. Both results for the disk of clockwise-moving stars from Levin & Beloborodov 2003 (disk A) and Paumard et al. 2006 (disk B) are shown in the Fig. 4.18. The rotational axis of the disk A is closer to the direction of the postulated outflow than the axis of the disk B. The reason for this behavior could be the choice of the stellar sample in both measurements. The sample in Levin & Beloborodov (2003) includes 10 of the 13 brightest brightest He stars, most of them designated as Ofpe/WN9 stars by Paumard et al. (2006). Disk A therefore contains the largest number of heavily mass-loosing stars.

Eckart et al. (2006) obtained polarization measurements of Sgr A* at two observing epochs (July 2005 and June 2004) and report the mean position angle of the E-vector to be about 60^o with a swing in polarization angle of up to 40-50^o. Meyer et al. (2006a) find that the inclination of the possible accretion disk around Sgr A* has a lower limit of about 30^o. It is interesting to point out that the range over which polarization angle varies on the plane of the sky, centered on Sgr A* (see Fig. 8 in Eckart et al. 2006), approximately coincides with the opening angle of the central outflow proposed in this work. These two phenomena could be connected under the assumption that the accretion disk, or the possible jet, may be polarized and the E-vector is positioned perpendicularly to the accretion disk, or along the jet (see the discussion in Eckart et al. 2006 and Meyer et al. 2006a). Fig 4.18 shows the orientations of the discussed structures for an observer at the center of the Galaxy.

Chapter 5

The IRS13 cluster

In chapter 2 we shortly introduced the IRS 13 object, and the two closely spaced (in projection, at least) groups of sources IRS 13E and IRS 13N. In this chapter I present in more detail both clusters (sections 5.1 and 5.2). In sections 5.2.1 and 5.2.2 I present proper motion measurements of IRS 13N members and the orbital analysis. In section 5.3 the possible boundness of the cluster and its nature are discussed. The results obtained in sections 5.2 and 5.3 have been published in Mužić et al. (2008).

5.1 IRS 13E

IRS 13E (located ~ 3" west and ~ 1.5" south of Sgr A*) is the densest stellar association after the stellar cusp in the immediate vicinity of Sgr A* and contains several massive WR and O-type stars (Maillard et al. 2004; Paumard et al. 2006; Moultaka et al. 2005). It is generally considered to be associated with the mini-spiral material (Moultaka et al. 2005; Paumard et al. 2004) and probably bound, since four out of seven identified stars show highly correlated velocities (see Fig. 5.1; Maillard et al. 2004; Schödel et al. 2005). For both of the above mentioned scenarios of star formation at the GC there are several issues when dealing with IRS 13E. In principle, such a cluster could have been formed in an accretion disk (Milosavljević & Loeb 2004; Nayakshin & Cuadra

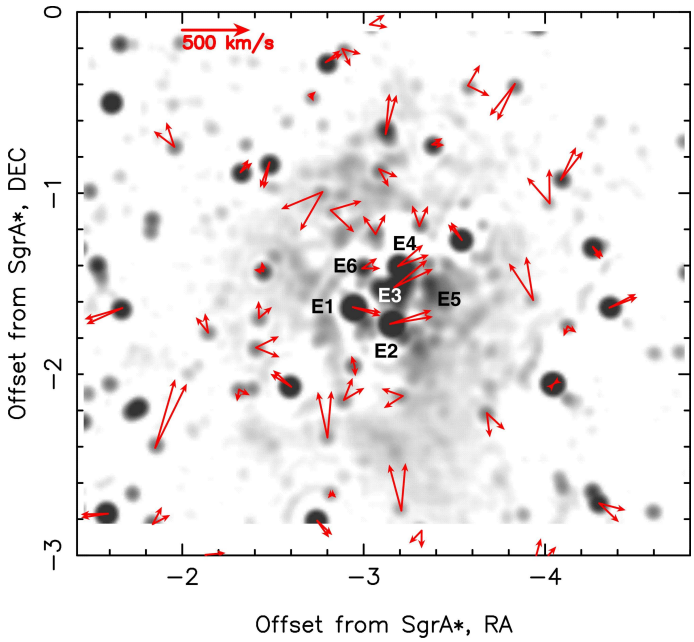

Figure 5.1: *Proper motions of stars in the vicinity of IRS 13E. The underlying NACO K-band image is LR-deconvolved and beam restored (60mas FWHM Gaussian beam). Two arrows are shown for each source, indicating the* $\pm 3\sigma$ *uncertainty of the direction of its proper motion. Image from Schödel et al. (2005).*

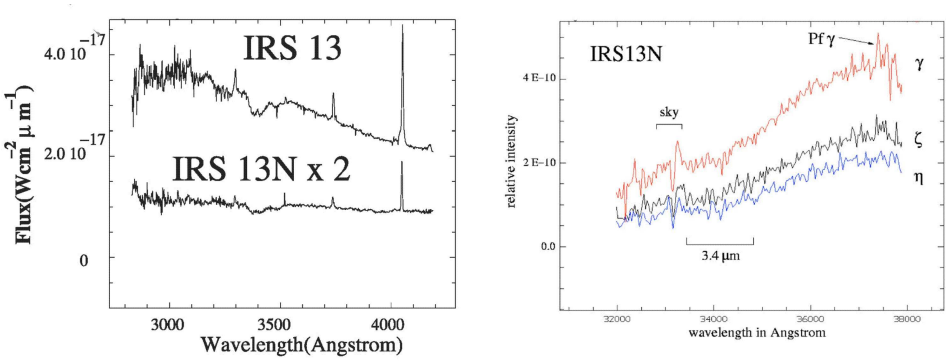

Figure 5.2: Left: *VLT/ISAAC spectra of IRS 13 region from Moultaka et al. (2004).* ***Right:*** *NACO L'-band spectra of the three resolved IRS 13N sources (Moultaka et al. 2005). The spectra of IRS 13N sources is consistent with the continuum emission by* $\sim$ *1000K dust.*

2005). However, in numerical simulations of star forming disks, a fragmentation of a disk cannot produce such a dominant feature (Nayakshin 2006b). In light of the cluster in-fall scenario, an intermediate-mass black hole (IMBH) was proposed to reside in the center of the cluster (Maillard et al. 2004). The existence of an IMBH makes the process of cluster in-spiral much more efficient in terms of increasing dynamical friction and thus allows the most massive stars that reside in the center of a very massive ($>10^6 M_\odot$) stellar cluster to reach the central parsec of the Galaxy within their lifetimes (Hansen & Milosavljević 2003; Berukoff & Hansen 2006; Portegies Zwart et al. 2006). However, the presence of the IMBH in IRS 13E is disputed. Schödel et al. (2005) analyze the velocity dispersion of cluster stars and derive that the mass of such an object should be at least 7000 $M_\odot$, making its existence implausible. Both the X-ray (Baganoff et al. 2003) and radio (Zhao & Goss 1998) source at the position of IRS 13E can be explained by colliding winds of high-mass losing stars (Coker et al. 2002; Zhao & Goss 1998), without the need for any unusual object. Paumard et al. (2006) suggest that, in case that IRS 13E is associated with the Bar of the mini-spiral, the mass of the stellar content would be high enough to keep the cluster from disruption.

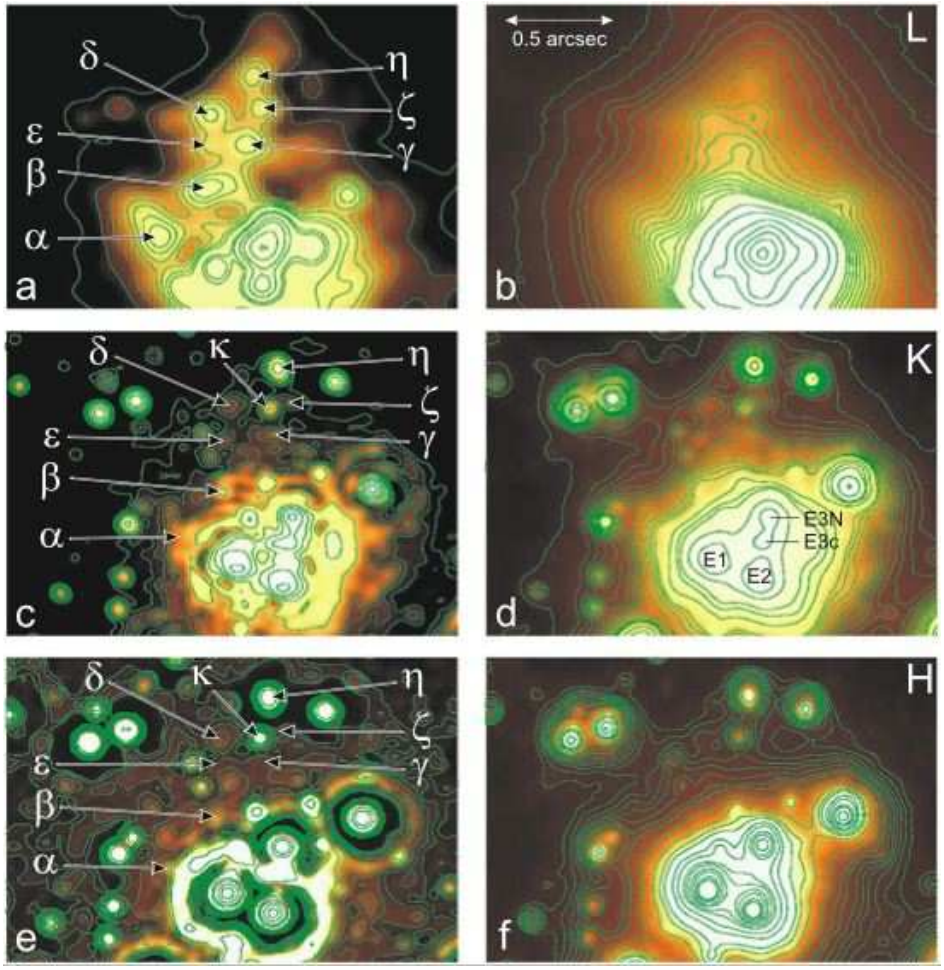

Figure 5.3: *Detailed view of IRS 13E and IRS 13N complexes with NAOS/CONICA in the L-band (a,b), K-band (c,d) and H-band (e,f). Images on the right are shift-and-add images of individual AO exposures, whereas images on the left are deconvolved and beam restored at the nominal angular resolution of the AO system. The ring-like structures around bright sources are artifacts of the deconvolution process. Image from Eckart et al. (2004).*

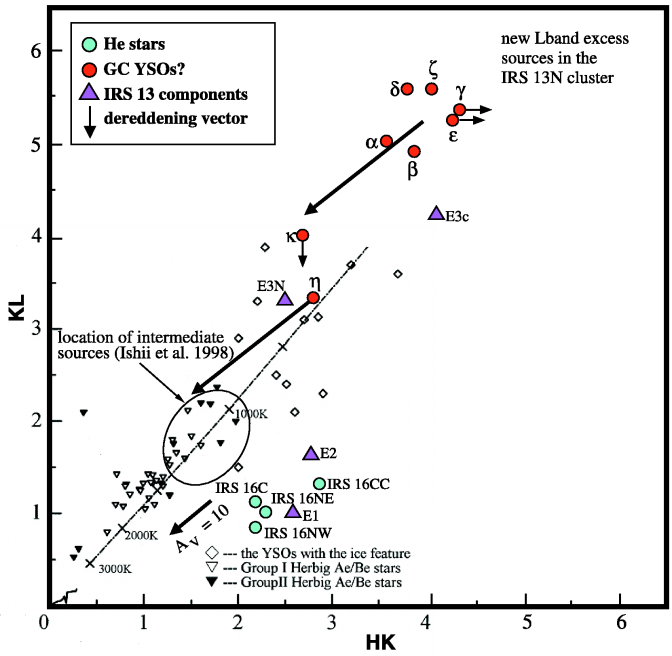

Figure 5.4: *Color-color diagram (Eckart et al. 2004) comparing the location of YSOs and Herbig Ae/Be stars to objects in the GC stellar cluster. Dashed lines show the colors of a single blackbody of different temperatures. A solid line in the lower left corner of the diagram represents the colors of main seqence stars. We show an extinction vector for a visual extinction of $A_V = 10$, as well as $A_V = 30$ vectors that shift the location of the L-band excess sources to the location of YSOs or the intermediate population introduced by Ishii et al. (1998).*

5.2 IRS 13N

Approximately 0.5" north of IRS 13E, a small cluster of unusually red compact sources was reported and named IRS 13N (Eckart et al. 2004). Eight sources have been resolved and labeled α through η as shown in Fig. 5.3. The spectra of IRS 13 components are shown in Fig. 5.2. A strong infrared excess is due to the emission of warm (T $\sim$1000 K) dust (Moultaka et al. 2005). Eckart et al. (2004) propose two possible explanations for the nature of IRS 13N: (1) objects older than few Myr and similar to bow-shock sources reported by Tanner et al. (2005) or (2) extremely young stars (0.1 - 1 Myr old). The latter scenario implies more recent star formation than what has been assumed so far for the GC environment.

Table 5.1 shows the photometry of the L-band excess sources and Fig. 5.4 shows an HKL two-color diagram comparing the locations of YSOs and Herbig Ae/Be stars to selected objects in the GC stellar cluster, both from Eckart et al. (2004). For the hot and dust-free sources like IRS 16NE, NW, C, and CC, an extinction correction can be applied. These objects are all well clustered in the two-color diagram and after taking into account the $\sim$30 mag of visual extinction toward the GC, these objects fall close to the location of hot and massive stars near the main sequence. However, after applying the extinction correction to the L-band excess sources, we see that they shift to the location of young stars. For the sources η and κ the K-L = 2-2.5 mag excess over the He star colors, as well as the L-, K-, and H-band flux densities at their positions are consistent with the colors and luminosities of young Herbig Ae/Be (Herbig group II) stars reddened by 30 mag of visual extinction. For the sources α to ζ the K-L = 4-5 mag excess over the He stars, as well as their flux densities, are consistent with the colors and luminosities of YSOs (Hillenbrand et al. 1992; Fuente et al. 2002; Ishii et al. 1998). With luminosities of $\sim 10^3$ $L_\odot$, IRS 13N sources are well within the expected luminosity range of 10^2-10^4 $L_\odot$ for 2-8 $M_\odot$Herbig group II sources and YSOs (e.g. Fuente et al. 2002). In this scenario, the L-band excess may be due to warm dust located in their circumstellar disks.

Table 5.1: *Positions, magnitudes and colors of IRS 13N sources*

name	$\Delta\alpha$ [a]	$\Delta\delta$ [a]	L' [b]	K_S	H	$K-L$	$H-K$
α	-2.70	-1.48	10.39	15.46	19.20	5.07	3.74
β	-2.89	-1.25	10.37	15.29	19.20	4.92	3.91
γ	-3.10	-0.99	10.63	16.11	>20.45	5.48	>4.35
δ	-2.92	-0.85	10.66	16.23	19.83	5.57	3.60
ϵ	-2.88	-1.02	10.91	16.34	>20.64	5.42	>4.30
ζ	-3.16	-0.82	10.82	16.42	20.54	5.60	4.12
η	-3.11	-0.66	10.85	14.20	17.07	3.35	2.87
κ	-3.09	-0.87	>11.28	15.35	18.06	<4.07	2.70

[a] relative to SgrA*, in arcseconds
[b] photometry from Eckart et al. (2004)

5.2.1 Proper motions

In tables 5.2 and 5.3 we list proper motions of IRS 13N and IRS 13E sources identified in L'-band, respectively. In Fig. 5.5 we show proper motions of all stars superposed on the L'-band image. Stars β through η show similar proper motions, revealing a new comoving group of sources at the GC. As shown in Eckart et al. (2004), only η can also be detected in the K-band. Paumard et al. (2006) give the full velocity information for this star: $v_{R.A.} = (-52\pm28)\mathrm{km\,s^{-1}}$, $v_{Dec.} = (257\pm28)\mathrm{km\,s^{-1}}$ and $v_r = (40\pm40)\mathrm{km\,s^{-1}}$. The authors identify it as a member of a possibly existing second stellar disk (CCWS).

Concerning IRS 13E, the obtained proper motion for E1 shows the biggest discrepancy with respect to previously published data (Paumard et al. 2006; Schödel et al. 2005). It also deviates significantly from the proper motions of the other three stars. It was already noted that E1 shows the largest deviation from the systemic proper motion of the cluster (Schödel et al. 2005). Paumard et al. (2006) argue that this star is possibly not bound to the cluster. This is supported by our result.

It is important to note that, in addition to a very dense stellar population in the region, a large amount of diffuse dust emission detected at 3.8 μm makes the

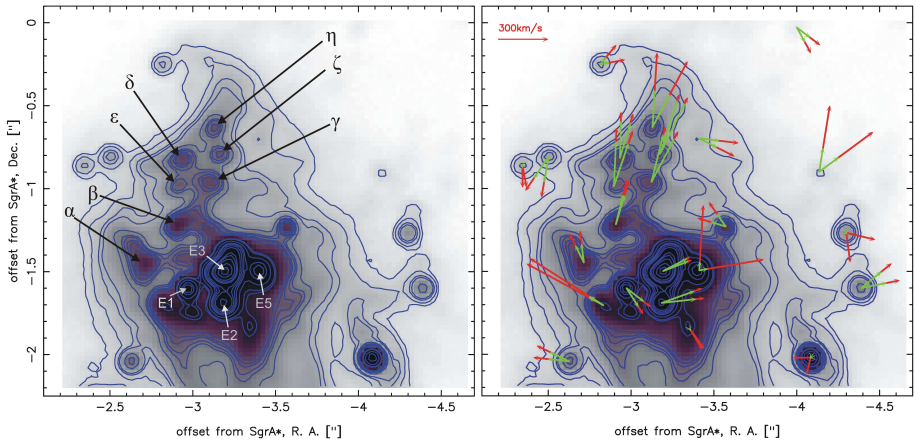

Figure 5.5: *Identification and proper motions of stars in IRS 13 complex. Four arrows are shown for each source, indicating the $\pm 3\sigma$ uncertainty of the value and direction of its proper motion.*

astrometry more challenging to perform than at shorter wavelengths. For this reason, StarFinder was not able to resolve all the previously reported K-band sources in the region. E3 is known to be at least a double source, while here we present it as a single one. E4 is located close to E3 but is much fainter in the L'-band. Therefore it could not be clearly identified by StarFinder. However, we were able to resolve the faint source E5 in all epochs and present the first proper motion measurement of this star. E5 was proposed to be a dusty WR star (Maillard et al. 2004), and it seems to exhibit a proper motion consistent with those of E2 and E3. This implies that it may be a cluster member.

From Tables 5.2 and 5.3 one can see that the average proper motions of the two clusters are significantly ($> 5\,\sigma$) different. Thus, it seems that two clusters do not belong to the same system.

5.2.2 Keplerian orbit fitting

In order to analyze our measurements we attempted to fit the positional data of IRS 13N stars showing similar proper motions (stars β to η) to Keplerian orbits[1], assuming that the gravitational potential is dominated by the SMBH at

[1]for more details of the fitting procedure see e.g. Eisenhauer et al. (2003)

Table 5.2: *Proper motions of IRS 13N sources observed in L'-band.*

name	$\Delta\alpha$ [a]	$\Delta\delta$ [a]	$v_{R.A.}$ [b]	$v_{Dec.}$ [b]
α	-2.70	-1.48	44 ± 8	147 ±13
β	-2.89	-1.25	- 6 ±20	228 ±15
γ	-3.10	-0.99	-114 ±14	298 ± 7
δ	-2.92	-0.85	-33 ±13	248 ± 9
ϵ	-2.88	-1.02	-58 ±15	306 ±13
ζ	-3.16	-0.82	-134 ± 9	333 ± 6
η	-3.11	-0.66	-91 ±22	323 ±39
13N[c]	-3.01	-0.93	-73 ± 7	289 ± 8

[a] relative to SgrA*, in arcseconds

[b] all velocities are in km s^{-1}; the uncertainties represent the 1σ uncertainty of the linear fit

[c] average proper motion of six comoving sources β-η

Table 5.3: *Proper motions of IRS 13E sources observed in L'-band.*

name	$\Delta\alpha$ [a]	$\Delta\delta$ [a]	$v_{R.A.}$ [b]	$v_{Dec.}$ [b]
E1	-2.95	-1.64	-107 ±11	-118 ± 6
E2	-3.16	-1.73	-228 ± 8	53 ± 9
E3	-3.17	-1.53	-158 ± 4	71 ± 3
E5	-3.39	-1.53	-175 ±45	140 ±72
13E [c]	-3.17	-1.61	-167 ±12	37 ±18
13E [d]	-3.24	-1.60	-187 ±15	88 ±24

[a] relative to Sgr A*, in arcseconds

[b] all velocities are in km s^{-1}; the uncertainties represent the 1σ uncertainty of the linear fit

[c] average proper motion of four IRS 13E sources

[d] average proper motion of IRS 13E without E1

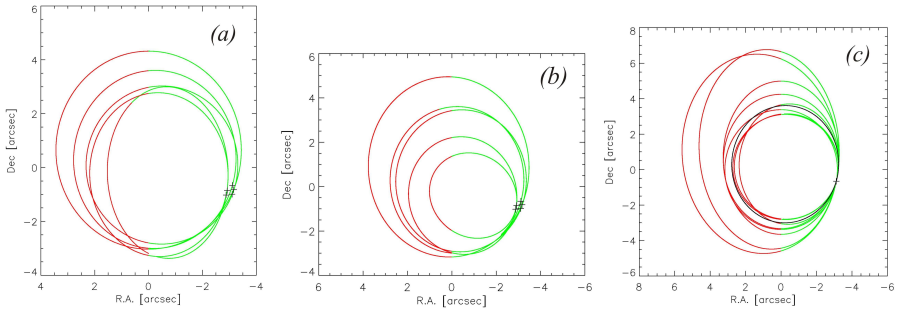

Figure 5.6: *(a) the best fit orbital solutions for five IRS 13N stars (γ – η); (b) orbital solutions for a single common plane (i=24^o, Ω=180^o), for stars γ – η ; (c) chosen 1σ orbits (see text for explanation) for η, with the best fit orbit colored black;*
NOTES: part of the orbit in front of the plane of the sky is colored red; crosses mark present positions of the stars; axes show the offset from Sgr A.*

the position of Sgr A*. The trajectory of a body of mass m in the gravitational field of a body of mass M ($m \ll M$) is an ellipse and can be described by the following parameters:

- semi-major axis a
- orbital period P
- numerical eccentricity e
- epoch of periastron passage t_0
- position angle of the ascending node, $0^o \leq \Omega \leq 180^o$; the nodes are the points of intersection of the orbit with the plane of the sky - the star recedes from us at the ascending node
- inclination i - the angle between the plane of the orbit and the plane of the sky, measured at the ascending node; $0^o \leq i \leq 90^o$ for counter-clockwise and $90^o \leq i \leq 180^o$ for clockwise rotation
- longitude of periastron, $0^o \leq \omega \leq 360^o$ the angle between the radius vector of the ascending node and that of the periastron in the orbital plane

Additional parameters that can be accounted for in the fitting procedure are the position, the velocity and the distance to the center of the orbit (Sgr A*). We assumed the distance and the mass of Sgr A* to be 7.6 kpc and 3.6×10^6 $M_\odot$, respectively. The velocity of Sgr A* was assumed to be zero (Reid & Brunthaler 2004). Under the assumption that the stars are really on bound orbits around Sgr A*, it is clear that our data cover only a small part of such an orbit. We also lack the radial velocity information for all of the stars. As a consequence, the χ^2 minimization gives a very wide span of orbital parameters for which $\chi^2<\chi^2{}_{min}+1$, even when fixing most of the free parameters (the mass of and the distance to Sgr A*, as well as the position and the velocity of the center of the orbit). Therefore we repeated the orbital fitting for each star introducing the radial velocity data as given in Paumard et al. (2006) for η. We varied the inclination angle i between 0^o and 90^o in steps of 1^o, Ω (position angle of the ascending node) between 0^o and 180^o in steps of 20^o and ω (longitude of periastron) between 0^o and 360^o with a step size of 20^o. The results are given in Table 5.4. We list the best fit parameters i and Ω, and give the 1σ range for the inclination. We also list the range in eccentricities (e) and semi-major axes (a) resulting from the fits for which there is some combination of angles (i, Ω, ω) that gives a fit better than 1σ ([2]). For all the stars except ζ, the best fit reduced χ^2 value ranges between 0.6 and 1.5. For ζ the best fit is obtained with χ^2=3.9, probably implying that either positional uncertainties are underestimated, or that assuming the radial velocity of η is a poor assumption. In the last three lines of Table 5.4 we give the best-fit parameters for the Keplerian orbits fitted onto the average positions of the stars within the IRS13N and IRS13E comoving groups. For IRS 13E we perform the fitting procedure twice: first including the star E1 and afterwards considering it a non-member.

Paumard et al. (2006) conclude that IRS 13E is on a fairly eccentric orbit, with $e\gtrsim0.5$, which we confirm. For all IRS 13N stars, with the exception of β, the range in eccentricities of 1σ orbits is restricted to fairly low values (<0.4), in agreement with the Paumard et al. (2006) value listed for η. Note that the corresponding semi-major axes also result fall within a restricted range of values. In contrast, both parameters (e and a) are poorly constrained for the star β. The size of the best fit orbit of β is an order of magnitude higher than those of the other five stars. Since the orbit of β is radically different from orbits

[2]a fit with $\chi^2<\chi^2{}_{min}+1$, for a corresponding star. For a convenience, we refer to all orbits that satisfy this condition as 1σ orbits.

Table 5.4: *Results of the Keplerian orbit fitting*

name	$i(^o)^a$	$\Omega(^o)^a$	$i(^o)^b$	e^c	$a('')^c$
β	79	180	53 - 80	0 - 0.9	4.0 - 180.0
γ	19	180	4 - 67	0.17 - 0.21	2.6 - 4.0
δ	48	180	39 - 71	0.15 - 0.4	2.7 - 15.0
ϵ	33	180	17 - 56	0.1 - 0.3	2.5 - 7.2
ζ	18	180	0 - 30	0.1 - 0.3	3.2 - 4.7
η	24	180	1 - 45	0.1 - 0.3	2.8 - 5.7
IRS 13N [d]	28	180	14 - 49	0.1 - 0.2	2.8 - 5.7
IRS 13E [d,e]	83	100	80 - 85	0.5 - 0.9	12.5 - 145.0
IRS 13E [d,f]	70	120	14 - 42; 58 - 80	0.5 - 0.8	2.3 - 66.0

[a] best fit parameters (χ^2=$\chi^2{}_{min}$)
[b] all inclination values for which χ^2<$\chi^2{}_{min}$+1
[c] calculated for (i, Ω, ω) combinations for which χ^2<$\chi^2{}_{min}$+1
[d] average orbit
[e] including E1
[f] not including E1

of all the other stars, we note that it probably should not be regarded as part of the co-moving group. Therefore we do not show its orbit in Fig. 5.6. Since η is the only star with known radial velocity, we took its orbital parameters and attempted to fit other stars onto the same orbit. We note that it is not possible to fit all other stars onto exactly the same orbit (same i, Ω and ω). Therefore we fix i and Ω and let ω vary. This confines the stars to the same plane, within which they can still have different orbits. For three stars (γ, ϵ, ζ) there exist 1σ orbits with given i and Ω, the star δ can be reasonably (but still not within 1σ) fitted, and β fails completely to be fitted onto this plane (Fig. 5.6*b*). To get a feeling about the uncertainties of our analysis, we plot several 1σ orbits for the same star (η) in Fig. 5.6*c*.

The implications of these results are further discussed in Section 5.3.2.

5.3 Discussion

5.3.1 3-dimensional position

Paumard et al. (2004) report the morphology and radial velocities of the mini-spiral gas based on He I and Br γ observations. At the position of the IRS 13 sources, the Northern Arm and the Bar of the mini-spiral are overlapping along the line of sight, with the Bar being placed further away from the observer. The authors suggest that IRS 13E must be either embedded in the Bar, or very close to it. Also, the radial velocities of the IRS 13E stars are similar to the radial velocities of the Bar material at this position (Paumard et al. 2004). Spectroscopic observations of the entire IRS 13 region (Moultaka et al. 2005) indicate a close spatial correlation between the stellar sources and the surrounding material. Higher water ice and hydrocarbon absorptions in the northern part of IRS 13, as well as a redder continuum emission, suggest that the IRS 13N sources are more embedded in the ISM than the rest of the complex. The radial velocity of η is consistent with the radial velocity of the Bar at this position (between 0 and 50 kms^{-1}, Paumard et al. 2004). If the northern sources that show similar proper motions also have correlated radial velocities, it would be reasonable to suggest that the entire complex is indeed associated with the Bar. According to our orbital fits, IRS 13N is located a few equivalent arcseconds behind Sgr A*, which nicely agree with the view of Paumard et al. (2004) about the Bar being located somewhat behind Sgr A*. This would imply that the IRS 13E and IRS 13N stellar complexes are spatially close. The existence of two comoving clusters, each moving in a completely different direction, poses a lot of challenges for star formation scenarios at the GC.

5.3.2 Is IRS 13N a bound system?

As can be seen from the orbital analysis, the best fit orbits for IRS 13N stars have rather different orbital parameters. Observing six stars on different orbits exactly at the moment when they appear to be very close in projection and to have similar proper motions is not very probable. There is no single orbit onto which all of the stars would fit with a good χ^2, but at least four of the stars can be confined to the same plane. In this case the stars are again on

different orbits and consequently have different orbital periods, spanning the range from 1000 to 3000 years. This again implies that the present arrangement is temporary. Also, it is curious that the moment at which we observe them coincides exactly with the presence of dense gas at their position. Interestingly, their most likely common plane seems to coincide with the plane of the counter-clockwise moving stars (CCWS; Paumard et al. 2006). The existence of the CCWS disk is still a matter of debate. According to Paumard et al. (2006), the disk is sparsely populated (12 stars), with η belonging to it. The assumption that all IRS 13N stars belong to the CCWS significantly increases the population of the disk, and at the same time weakens the claim that the CCWS is essentially in non-circular motion. In the analysis of Paumard et al. (2006), seven out of twelve CCWS stars are on eccentric orbits (e>0.4), three of those belonging to IRS 13E system. We find that five of the IRS 13N stars are on low-eccentricity orbits.

The analysis of 1σ orbits for one star (Fig. 5.6*c*) shows that the uncertainty of semi-major axes (a), as well as that of orbital periods (P), is of the same order as the differences between a and P of each star. Therefore, at this point we still cannot exclude that IRS 13N stars are indeed orbiting together. In the following we consider the possibility that the cluster is bound. We calculate the velocity dispersion of stars as

$$\sigma^2 = \sigma_{pm}^2 - \sum_{i=1}^{N} [error^2(v_{x,i}) + error^2(v_{y,i})]/[2(N-1)] \tag{5.1}$$

where σ_{pm} is the dispersion of the measured proper motions and the second term removes the influence of the proper motion measurement uncertainties.

The mass estimate from the velocity dispersion of stars gives $\sim$3300 $M_\odot$, an unrealistically high mass for such a cluster. For a comparison, we note that Paumard et al. (2006) estimate the total stellar mass of IRS 13E to be $\sim$1000 $M_\odot$. We note that even if the uncertainties in proper motion measurements were underestimated, the final mass of the cluster calculated from the velocity dispersion would remain high. For instance, a hypothetical underestimation of our uncertainties of 30% would result in $\sim$8% lower velocity dispersion and the mass of 2700 $M_\odot$.

The Hill radius

$$r_{Hill} \approx a(1-e)\Big(\frac{m}{3M}\Big)^{\frac{1}{3}} \tag{5.2}$$

for a cluster of $m = 3300\,\mathrm{M}_{\odot}$, with $a = (2.8\text{-}5.7)$" and $e = 0.1\text{-}0.3$ is $r_{Hill} \approx 0.17\text{" - }0.34$", with the average value remarkably close to the observed cluster radius of ~ 0.25". The other way around, if we set $r_{Hill} \sim 0.25$", the maximum a and minimum e, the minimum mass needed to keep the cluster from disruption would be $1250\mathrm{M}_{\odot}$.
The relaxation time for a system of N stars with the mean mass m_* is given by

$$t_{relax} \approx \frac{N}{8ln\Lambda} \times t_{cross} \tag{5.3}$$

where $t_{cross}=R/v$ and $\Lambda=R\mathrm{v}^2/\mathrm{Gm}_* \approx N$ (Binney & Tremaine 1987). Also, it is important to note that tidal interactions tend to shorten relaxation timescales. A cluster with the IRS 13N velocity dispersion would have a t_{relax} of the order of the IRS 13N orbital period only if it was consisted of 500-1000 stars. For $\mathrm{m} \sim 3300\mathrm{M}_{\odot}$contained in 500-1000 main sequence stars we get that stars should be as bright as m_K=17-18 (assuming the extinction $A_K \approx 3$, Schödel et al. 2007). These stars would be observed. For a lower mass limit of $1250\mathrm{M}_{\odot}$, we get m_K=19-21, exactly at the limit of NACO K-band data. Therefore it seems that the system could hardly be bound and survive for a significant time in the orbit around Sgr A*.

If IRS 13N stars are not bound, the observed velocity dispersion probably indicates that the cluster is in the process of dissolution. The velocity dispersion will subsequently diminish the stellar surface number density of the cluster, which would within only a few hundred years reach the background value given by Schödel et al. (2007).

5.3.3 The nature of IRS 13N

The detailed discussion about the nature of IRS 13N sources is presented in Eckart et al. (2004). Among other possibilities, the authors argue that infrared excess sources IRS 13N could represent objects that have colors and luminosities consistent with YSOs and Herbig Ae/Be stars. Dusty envelopes that usually surround those objects would then give rise to the observed strong infrared excess. It is striking that six of the sources that are very close in projection,

also show very similar proper motion values. In the previous section we argue that IRS 13N could hardly survive in the present arrangement for a significant amount of time. The indication of a dynamically young stellar system concurs with the Eckart et al. (2004) hypothesis of IRS 13N stars being extremely young objects. But why then does this object exist at all? Timescales for its disruption seem to be much shorter than any timescales within which stars normally form. Here we must take into account that the Galactic Center is an extremely complex environment and that any star formation process that takes place there is completely different from the "normal" star formation via the fragmentation of a molecular cloud. Timescales for star formation could be significantly shorter. The free-fall time in a collapsing cloud at the distance of the young stars in the central half parsec around Sg rA* is of the order of 100-1500 yr. Also, simulations of star formation in a gaseous disk around Sgr A* by Nayakshin et al. (2007) indicate that the timescales for star formation are fairly short, of the order of several thousand years. This is comparable to the orbital timescale of IRS 13N.

A serious obstacle for forming stars at the GC is that the gas densities in the central parsec are way too low for the gas to be able to form stars. Even the highest density estimates for the circumnuclear disk (CND; Christopher et al. 2005) are several orders of magnitude lower than required to fulfill the criterion for Jeans instability. However, with the aid of shocks and collisions, a small clump of gas in-falling to the center could be highly compressed and star formation within it triggered. As a matter of fact, the mini-spiral is a short-lived feature (t_{dyn}~10^4 yr) and is in-falling right now. Furthermore, the material of the mini-spiral is susceptible to shocks, as discussed by e.g. Mužić et al. (2007). A possibility of forming stars in small associations has never been discussed so far for this region. Star formation in small groups definitely would not be able to account for the young co-eval stellar population in the central parsec, but could, in general, be possible and result in small associations like IRS 13N.

However, it is clear that we still must be very careful when drawing a conclusion that IRS 13N cluster contains very young stars. In case that the cluster is indeed a part of the CCWS disk and that the stars were formed simultaneously with other CCWS stars, then they must be several Myr old. The fact that they are apparently strongly extincted may then indicate that

they are similar to the mini-spiral bow-shock sources (Tanner et al. 2005), but many times less massive and luminous (see discussion in Eckart et al. 2004). The question remains: why are they clustered?

Chapter 6

Summary and conclusions

In this chapter I summarize the results obtained in this work and also give an outlook towards the future observations that could clarify the issues concerning the real nature of the objects of concern.

6.1 Narrow filaments

In chapter 4 we have presented L'-band (3.8 μm) adaptive optics observations of an approximately 18×18 arcsec^2 (0.7×0.7 pc^2) region around Sgr A*. The images reveal a large number of thin filaments associated with the mini-spiral, that could be due to the interaction of a fast wind with an ambient ISM. The previous detection of some of the filaments in the radio regime, as well as in Br γ and Pa α lines, shows that the filaments are not only associated with the continuum emission by dust, but also with the ionized gas component of the ISM. We performed proper motion measurements of these features on the time basis of approximately 4 years. The filaments located west from Sgr A* are curved with their convex sides westwards and show a significant proper motion to the west. The comparison with the Keplerian orbit fitting of the Northern Arm presented in Paumard et al. (2004), tells us that the process that drives the motion of the filaments cannot be purely due to the gravitational potential of the supermassive black hole at the center.

We propose the following scenario: An at least partially collimated outflow is emanating from a combination from the disk of high mass-losing He-stars and an outflow associated with the black hole at the position of Sgr A*. This scenario represents a unified model that would explain the mini-cavity, the two cometary shaped sources X3 and X7, as well as the northern and southern lobes in the NIR H_2 emission. It would also be in agreement with the NIR polarization data that is indicative for a temporal accretion disk around Sgr A* and would be supportive for a collimated outflow that is often invoked to explain the properties of Sgr A*.

Future directions

High-resolution spectroscopy that could show if there are shock-diagnostic lines coming primarily from the filaments is needed in order to confirm our interpretation. Identifying (some of) the narrow filaments as shocks would provide compelling evidence for the existence of strong outflows from the region near the supermassive BH SgrA*. Furthermore, constraining the strength of the shocks could help us to distinguish between their causes, i.e., stellar winds and/or a fast jet-like outflow from Sgr A*. As we have seen in section 1.3, the ro-vibrational H_2 lines are one of the most significant tracers of shock interactions in the ISM. Therefore, mapping of the central 0.5 pc of the Galaxy in the NIR H_2(1-0)S(1) line at 2.12 μm is optimal to solve this problem. The observations should be accompanied by observations of another molecular hydrogen line, 2.25 μm H_2(2-1)S(1), in order to distinguish between fluorescent and shock excitation. The gas in the central parsec is mostly ionized. However, the H_2(1-0)S(1) line can clearly be seen in our ISAAC/VLT medium resolution spectra of the central cluster (slit of 0.6"). The mini-spiral streamers also contain dust and they are, after all, no static features. Therefore it seems reasonable to search for emission from molecular hydrogen in the narrow filaments. Here high resolution observations are necessary in order to be able to distinguish the individual features. From this point of view NACO/VLT is well suited, but unfortunately its drawback is the lack of the second H_2 narrow band filter. Keck NIR instruments NIRC and NIRC2 are equipped with both of the required filters.

6.2 IRS 13N

In chapter 5 we have presented the proper motion measurements of IRS 13N, a newly discovered co-moving group of red sources at the GC. We discuss the boundness of a cluster and a possibility that these stars are the youngest stellar object ever observed in this environment. Ongoing star formation in the GC would have significant implications on our understanding of this particular environment, and star formation in galactic nuclei in general. It has been assumed that the star formation in the GC occurred in two star bursts, ∼100 Myr and ∼7 Myr ago (e.g. Krabbe et al. 1995). The existence of objects younger than 1 Myr would imply that in-situ star formation in the GC and near massive black holes in general is possible. Furthermore, this would also mean that star formation in the GC must not necessarily be related to star bursts and that, in fact, a continuous star formation could be ongoing.

Future directions

Although our findings strongly support the hypothesis of IRS 13N stars being very young, the question of the real nature of the IRS 13N cluster still remains open. More imaging and especially high resolution spectroscopic data that could reveal features attributed to YSOs will be necessary to confirm our hypothesis. Here we have a restriction in the wavelength regime suitable for the observations: most of the IRS 13N members are not observable in the K-band and in the MIR the possibility to resolve individual stars is limited by the resolution. Ishii et al. (1998) investigate a sample of 58 YSO candidates with the intention to further classify them on the basis of spectral features - 3.1μm H_2O ice absorption and 3.3μm UIB emission. The H_2O ice feature occurs in high-density interstellar clouds that are protected from UV radiation. It is ubiquitously found in spectra of YSOs deeply embedded in molecular clouds. The UIB feature is often found in regions where dust is exposed to UV radiation, such as planetary nebulae, H II regions, reflection nebulae, and external galaxies. Ishii et al. (1998) suggest that these two features can be used as diagnostics of interactions between radiation fields and dust around YSOs. In about 70 % of the spectra in their sample at least one of the two features was detected. However, H_2O feature should also appear whenever molecular clouds lie between the source and the observer. Therefore it could be very difficult to distinguish spectral features that are of real stellar origin. Also, in the present spectra of IRS 13N complex (Moultaka et al. 2005; Eckart et al.

2004), no H_2O absorption can be identified with certainty. However, the disk material will very likely be affected by the intense radiation field at the GC (Lutz et al. 1996). In this case the ices in the disk may become either tenuous and/or destroyed by hard-UV photons. It is therefore not clear how deep an H_2O absorption feature one can expect from YSOs in the GC environment.

Bibliography

Aitken, D. K., , Gezari, D., et al. 1991, ApJ, 380, 419

Aitken, D. K., Smith, C. H., Moore, T. J. T., & Roche, P. F. 1998, MNRAS, 299, 743

Alexander, T. 2005, Physics Reports, 419, 65

Allen, D. A. & Sanders, R. H. 1986, nat, 319, 191

Baganoff, F. K., Maeda, Y., Morris, M., et al. 2003, ApJ, 591, 891

Beloborodov, A. M., Levin, Y., Eisenhauer, F., et al. 2006, ApJ, 648, 405

Berukoff, S. J. & Hansen, B. M. S. 2006, ApJ, 650, 901

Binney, J. & Tremaine, S. 1987, Galactic Dynamics (Princeton University Press)

Blandford, R. & Begelman, M. 1999, MNRAS, 303, L1

Blum, R. D., DePoy, D. L., & Sellgren, K. 1995, ApJ, 441, 603

Bower, G. C., Wright, M. C. H., Falcke, H., & Backer, D. C. 2003, ApJ, 588, 331

Brandner, W., Rousset, G., Lenzen, R., et al. 2002, Messenger, 107, 1

Burton, M. & Allen, D. 1992, PASAu, 10, 55

Chiar, J. E., Tielens, A. G. G. M., Whittet, D. C. B., et al. 2000, ESA SP, 456, 45

Christopher, M. H., Scoville, N. Z., Stolovy, S. R., & Yun, M. S. 2005, ApJ, 622, 346

Clénet, Y., Rouan, D., Gendron, E., et al. 2004, A&A, 417, L15

Clénet, Y., Rouan, D., Gendron, E., et al. 2001, A&A, 376, 124

Coker, R., Melia, F., & Falcke, H. 1999, ApJ, 523, 642

Coker, R., Pittard, J. M., & Kastner, J. H. 2002, A&A, 383, 568

Cuadra, J., Nayakshin, S., Springel, V., & Di Matteo, T. 2006, MNRAS, 366, 358

Diolaiti, E., Bendinelli, O., Bonaccini, D., et al. 2000, A&AS, 147, 335

Dopita, M. A. & Sutherland, R. S. 2003, Astrophysics of the Diffuse Universe (Springer, Berlin)

Draine, B. T. 1989, in Infrared Spectroscopy in Astronomy, ESA SP-290, ed. B. Kaldeich, 93

Draine, B. T. 2003, Ann. Rev. Astron. Astrophys., 41, 241

Draine, B. T. & McKee, C. F. 1993, Ann. Rev. Astron. Astrophys., 31, 373

Draine, B. T., Roberge, W. G., & Dalgarno, A. 1983, A&AS, 264, 485

Eckart, A. & Duhoux, P. R. M. 1990, in ASP Confrence Series, Volume 14, Astrophysics with Infrared Arrays (San Francisco: ASP), ed. R. Elston, 336

Eckart, A. & Genzel, R. 1996, in ASP Confrence Series, Volume 102, The Galactic Center, ed. R. Gredel, 196

Eckart, A., Genzel, R., Hofmann, R., Sams, B. J., & Tacconi-Garman, L. E. 1995, ApJ, 445, L23

Eckart, A., Genzel, R., Krabbe, A., et al. 1992, Nature, 355, 526

Eckart, A., Genzel, R., Ott, T., & Schödel, R. 2002, MNRAS, 331, 917

Eckart, A., Moultaka, J., Viehmann, T., Straubmeier, C., & Mouawad, N. 2004, ApJ, 602, 760

Eckart, A., Ott, T., & Genzel, R. 1999, A&A, 352, L22

Eckart, A., Schödel, R., Meyer, L., et al. 2006, A&A, 455, 1

Eckart, A., Schödel, R., & Straubmeier, C. 2005, The black hole at the center of the Milky Way (London:Imperial College Press; Hackensack, NJ: Distributed by World Scientific Pub. Co.)

Eisenhauer, F., Genzel, R., Alexander, T., et al. 2005, ApJ, 628, 246

Eisenhauer, F., Schödel, R., Genzel, R., et al. 2003, ApJ, 597, L121

Falcke, H. & Markoff, S. 2000, A&A, 362, 113

Fuente, A., Martín-Pintado, J., Bachiller, R., Rodrǵuez-Franco, A., & Palla, F. 2002, A&A, 387, 977

Gatley, I., Beattie, D., Lee, T., Jones, T., & Hyland, A. 1984, MNRAS, 210, 565

Gatley, I., Jones, T., Hyland, A., Wade, R., & Geballe, T. 1986, MNRAS, 222, 299

Genzel, R., Eckart, A., Ott, T., & Eisenhauer, F. 1997, MNRAS, 291, 219

Genzel, R., Pichon, C., Eckart, A., Gerhard, O. E., & Ott, T. 2000, MNRAS, 317, 348

Genzel, R., Schödel, R., Ott, T., et al. 2003, ApJ, 594, 812

Genzel, R., Thatte, N., Krabbe, A., Kroker, H., & Tacconi-Garman, L. E. 1996, ApJ, 472, 153

Gerhard, O. 2001, ApJ, 546, L39

Ghez, A. M., Klein, B. L., Morris, M., & Becklin, E. E. 1998, ApJ, 509, 678

Ghez, A. M., Morris, M., Becklin, E. E., Tanner, A., & Kremenek, T. 2000, Nature, 407, 349

Ghez, A. M., Salim, S., Hornstein, S. D., et al. 2005, ApJ, 620, 744

Gibb, E. L., Whittet, D. C. B., Boogert, A. C. A., & Tielens, A. G. G. M. 2004, ApJS, 151, 35

Glass, I. S. 1999, Handbook of Infrared Astronomy (Cambridge University Press)

Goodman, J. & Tan, J. C. 2004, ApJ, 608, 108

Güsten, R., Genzel, R., Wright, M. C. H., et al. 1987, ApJ, 318, 124

Hansen, B. M. S. & Milosavljević, M. 2003, ApJ, 593, L77

Hartigan, P., Raymond, J., & Hartmann, L. 1987, ApJ, 316, 323

Herrnstein, R. & Ho, P. 2002, ApJL, 579, L83

Hillenbrand, L. A., Strom, S. E., Vrba, F. J., & Keene, J. 1992, ApJ, 397, 613

Hollenbach, D. J. & McKee, C. F. 1979, ApJ Supplement Series, 41, 555

Hollenbach, D. J. & McKee, C. F. 1989, ApJ, 342, 306

Ishii, M., Nagata, T., Sato, S., et al. 1998, AJ, 116, 868

Jackson, J. M., Geis, N., Genzel, R., et al. 1993, ApJ, 402, 173

Kim, S. S., Figer, D. F., & Morris, M. 2004, ApJ, 607, L123

Kim, S. S. & Morris, M. 2003, ApJ, 597, 312

Krabbe, A., Genzel, R., Eckart, A., et al. 1995, ApJ, 447, L95

Krishna Swamy, K. S. 2005, Dust in the Universe - Similarities and differencies (World Scientific Series in Astronomy and Astrophysiscs Vol. 7)

Lacy, J. H., Achtermann, J. M., & Serabyn, E. 1991, ApJL, 380, L71

Lee, S., Pak, S., Lee, S.-G., et al. 2005, MNRAS, 361, 1273

Léna, P., Lebrun, F., & Mignard, F. 1998, Observational Astrophysics (Springel-Verlag Berlin Heidelberg)

Lenzen, R., Hofmann, R., Bizenberger, P., & Tusche, A. 1998, in Proc. SPIE Vol. 3354, Infrared Astronomical Instrumentation, ed. A. M. Fowler, 606

Levin, Y. & Beloborodov, A. 2003, ApJL, 590, L33

Lissauer, J. J. 1987, Icarus, 69, 249

Lucy, L. B. 1974, AJ, 79, 745

Lutz, D., Feuchtgruber, H.and Genzel, R., Kunze, D., et al. 1996, A&A, 315, 269

Lutz, D., Krabbe, A., & Genzel, R. 1993, ApJ, 418, 244

Maillard, J. P., Paumard, T., Stolovy, S. R., & Rigaut, F. 2004, A&A, 423, 155

Markoff, S. & Falcke, H. 2003, Astron.Nachr., 324, 3

Marrone, D. P., Moran, J. M., Zhao, J.-H., & Rao, R. 2006, ApJ, 640, 308M

Mathis, J. S. 1990, Ann. Rev. Astron. Astrophys., 28, 37

McKee, C. F. & Hollenbach, D. J. 1980, Ann. Rev. Astron. Astrophys., 18, 219

McMillan, S. L. W. & Portegies Zwart, S. F. 2003, ApJ, 596, 314

Melia, F., Coker, R., & Yusef-Zadeh, F. 1996, ApJL, 460, L33

Melia, F. & Falcke, H. 2001, Ann. Rev. Astron. Astrophys., 39, 309

Menten, K. M., Reid, M. J., Eckart, A., & Genzel, R. 1997, ApJ, 475, L111

Meyer, L., Eckart, A., Schödel, R., et al. 2006a, A&A, 460, 15

Meyer, L., Schödel, R., Eckart, A., et al. 2006b, A&A, 458, 25

Milosavljević, M. & Loeb, A. 2004, ApJ, 604, L45

Morris, M. & Maillard, J.-P. 2000, in ASP Confrence Series, Volume 195, Imaging the Universe in Three Dimensions: Astrophysics with Advanced Multi-Wavelenght Imaging Devices., ed. W. van Breugel & J. Bland-Hawthorn, 196

Moultaka, J., Eckart, A., Schödel, R., Viehmann, T., & Najarro, F. 2005, A&A, 443, 163

Moultaka, J., Eckart, A., Viehmann, T., et al. 2004, A&A, 425, 527

Mužić, K., Eckart, A., , Schödel, R., Meyer, L., & Zensus, A. 2007, A&A, 469, 993

Mužić, K., Schödel, R., Eckart, A., Meyer, L., & Zensus, A. 2008, A&A, 482, 173

Najarro, F., Krabbe, A., Genzel, R., et al. 1997, A&A, 325, 700

Nayakshin, S. 2006b, in Journal of Physics: Conference Series, Volume 54, ed. R. Schödel, G. C. Bower, M. P. Muno, S. Nayakshin, & T. Ott, 208

Nayakshin, S. & Cuadra, J. 2005, A&A, 437, 437

Nayakshin, S., Cuadra, J., & Springel, V. 2007, MNRAS, 379, 21

Nayakshin, S., Dehnen, W., Cuadra, J., & Genzel, R. 2006a, MNRAS, 366, 1410

Ott, T., Eckart, A., & Genzel, R. 1999, ApJ, 523, 248

Paumard, T., Genzel, R., Martins, F., et al. 2006, ApJ, 643, 1011

Paumard, T., Maillard, J.-P., & Morris. 2004, A&A, 426, 81

Paumard, T., Maillard, J.-P., Morris, M., & Rigaut, F. 2001, A&A, 366, 466

Portegies Zwart, S. F., Baumgardt, H., Hut, P., Makino, J., & McMillan, S. L. W. 2004, Nature, 428, 724

Portegies Zwart, S. F., Baumgardt, H., McMillan, S. L. W., et al. 2006, ApJ, 641, 319

Portegies Zwart, S. F. & McMillan, S. L. W. 2002, ApJ, 576, 899

Pott, J.-U., Eckart, A., Glindemann, A., et al. 2008, A&A, 480, 115

Quataert, E. 2003, Astron. Nachr., 324, 3

Reid, M. J. 1993, Ann. Rev. Astron. Astrophys., 31, 345

Reid, M. J. & Brunthaler, A. 2004, ApJ, 616, 872

Reid, M. J., Menten, K. M., Genzel, R., et al. 2003, ApJ, 587, 208

Richardson, W. H. 1992, J. Opt. Soc. Am., 62, 55

Rieke, G. H. & Lebofsky, M. J. 1985, ApJ, 288, 618

Rieke, G. H., Rieke, M. J., & Paul, A. E. 1989, ApJ, 336, 752

Roberts, D. A. & Goss, W. M. 1993, ApJ.Suppl., 86, 133

Roberts, D. A., Yusef-Zadeh, F., & Goss, W. M. 1996, ApJ, 459, 627

Rosenthal, D., Bertoldi, F., & Drapatz, S. 2000, A&A, 356, 705

Rousset, G., Lacombe, F., Puget, P., et al. 1998, in Proc. SPIE Vol. 3353, Adaptive Optical System Technologies, ed. D. Bonaccini, 516

Schödel, R., Eckart, A., Alexander, T., et al. 2007, astro-ph/0703178, accepted by A & A

Schödel, R., Eckart, A., Iserlohe, C., Genzel, R., & Ott, T. 2005, ApJ, 625, L111

Schödel, R., Ott, T., Genzel, R., et al. 2003, ApJ, 596, 1015

Schödel, R., Ott, T., Genzel, R., et al. 2002, Nature, 419, 694

Scoville, N. Z., Stolovy, S. R., Rieke, M., Christopher, M., & Yusef-Zadeh, F. 2003, ApJ, 594, 294

Simon, M., Chen, W.-P., Forrest, W. J.and Garnett, J. D., et al. 1990, ApJ, 360, 95

Stahler, S. W. & Palla, F. 2004, The Formation of stars (WILEY-VCH Verlag GmbH & Co. KGaA)

Starck, J.-L. & Murtagh, F. 2006, Astronomical Image and Data Analysis (Springer-Verlag Berlin Heidelberg)

Stolte, A., Ghez, A. M., Morris, M., et al. 2007, arXiv:0706.4133v1

Tanner, A., Ghez, A. M., Morris, M. R., et al. 2002, ApJ, 575, 860

Tanner, A., Ghez, A. M., Morris, M. R., & Christou, J. C. 2005, ApJ, 624, 742

Tielens, A. G. G. M. 2005, The Physics and Chemistry of the Interstellar Medium (Cambridge University Press)

Viehmann, T., Eckart, A., Schödel, R., et al. 2005, A&A, 433, 117

Viehmann, T., Eckart, A., Schödel, R., Pott, J.-U., & Moultaka, J. 2006, ApJ, 642, 861

Vollmer, B. & Duschl, W. 2000, New Astronomy, 4, 581

Vollmer, B. & Duschl, W. 2001, A&A, 367, 72

Weingartner, J. C. & Draine, B. T. 2001, ApJ, 548, 296

Whittet, D. C. B., Martin, P. G., Fitzpatrick, E. L., & Massa, D. 1993, ApJ, 408, 573

Wright, M., Coil, A., McGary, R., Ho, P., & Harris, A. 2001, ApJ, 551, 254

Yuan, F. 2006, in Journal of Physics: Conference Series, Volume 54, Issue 1, ed. R. Schödel, G. C. Bower, M. P. Muno, S. Nayakshin, & T. Ott, 427

Yuan, F., Markoff, S., & Falcke, H. 2002, A&A, 383, 854

Yusef-Zadeh, F. & Melia, F. 1992, ApJL, 385, L41

Yusef-Zadeh, F., Morris, M., & Ekers, R. D. 1990, Nature, 348, 45

Yusef-Zadeh, F., Roberts, D. A., & Biretta, J. 1998, ApJL, 499, L159

Yusef-Zadeh, F., Stolovy, S. R., Burton, M., Wardle, M., & Ashley, M. C. B. 2001, ApJ, 560, 749

Yusef-Zadeh, F. & Wardle, M. 1993, ApJ, 405, 584

Zhao, J.-H. & Goss, W. 1998, ApJL, 499, L163

Zylka, R., Mezger, P., Ward-Thompson, D., Duschl, W. J., & Lesch, H. 1995, A&A, 297, 83

List of Figures

List of Tables

List of Acronyms

AK	extinction in K-band
ADAF	Advection Dominated Accretion Flow
ADIOS	Adiabatic inflow-outflow solution
AGB	Asymptotic Giant Branch
AGN	Active Galactic Nucleus
AO	Adaptive Optics
BH	Black Hole
CND	Circum Nuclear Disk
CONICA	High Resolution IR Camera and Spectrometer
CCWS	Counter-clockwise rotating stellar disk
CWS	Clockwise rotating stellar disk
ESO	European Southern Observatory
FOV	Field of view
FUV	Far-ultraviolet
FWHM	Full Width at Half Maximum
GC	Galactic Center
HST	Hubble Space Telescope
IMBH	Intermediate-mass black hole
IMF	Initial mass function
IR	Infrared
ISAAC	Infrared Spectrometer and Array Camera (at the VLT)
ISM	Interstellar medium
LBV	Luminous blue variable
LGS	Laser guide star
LR	Lucy-Richardson
LTE	Local Thermodynamic Equilibrium

MBH	Massive Black Hole
MIR	Mid-infrared
NA	Northern Arm of the mini-spiral
NACO	NAOS/CONICA adaptive optics device/near-infrared camera at the VLT
NAOS	Nasmyth Adaptive Optics System
NGS	Natural guide star
NICMOS	Near Infrared Camera and Multi-Object Spectrometer (on board of the HST)
NIR	Near-infrared
OMC	Orion Molecular Cloud
PAH	Polycyclic aromatic hydrocarbon
PDR	Photo-dissociative region
PSF	Point Spread Function
RIAF	Radiatively Inefficient Accretion Flow
SED	Spectral energy distribution
Sgr A*	Sagittarius A*
SMBH	Supermassive Black Hole
UIB	Unidentified infrared emission band
UV	Ultraviolet
VLA	Very Large Array
VLBA	Very Long Baseline Array
VLT	Very Large Telescope
VISIR	VLT spectrometer and imager for the mid–infrared
WFS	Wavefront sensor
WR	Wolf-Rayet
YSO	Young stellar object

Acknowledgements

There are several people to whom I would like to express my gratitude:
First of all, the biggest "thank you" goes to my supervisor Andreas Eckart for all the support during the last few years.
Another big one is for Rainer Schödel who carefully watched and corrected my steps from the beginning – although sometimes making me go crazy with the amount of comments (I know it's only for my good:)
I would like to thank the entire aegroup for the enjoyable working atmosphere and help. Just to name some of them: Christian Straubmeier and Thomas Bertram for solving computer problems; Leo and Jörg-Uwe for being great as they are (alter!); my fellow citizens of the Republic of Montenegro, Mohammad and Devi, for everything.
I am grateful to all the Ph1 secretaries for making my life easier.

This work was financially supported by the International Max Planck Research School (IMPRS) at the Universities of Bonn and Cologne. I would like to thank my co-referee Prof. Dr. Anton Zensus for his support, and to Mrs. Gabi Breuer and Dr. Eduardo Ros for the fantastic job they are doing.

Many thanks to my Cologne-time friends Nadia, Nina, Chiara and Edouard.

Na kraju, hvala mami i tati, Davi i mojoj nadasve šesnoj braći.

Erklärung

Ich versichere, daß ich die von mir vorgelegte Dissertation selbständig angefertigt, die benutzten Quellen und Hilfsmittel vollständig angegeben und die Stellen der Arbeit – einschließlich Tabellen, Karten und Abbildungen –, die anderen Werken im Wortlaut oder dem Sinn nach entnommen sind, in jedem Einzelfall als Entlehnung kenntlich gemacht habe; daß diese Dissertation noch keiner anderen Fakultät oder Universität zur Prüfung vorgelegen hat; daß sie – abgesehen von unten angegebenen Teilpublikationen – noch nicht veröffentlicht worden ist sowie, daß ich eine solche Veröffentlichung vor Abschluß des Promotionsverfahrens nicht vornehmen werde. Die Bestimmungen dieser Promotionsordnung sind mir bekannt. Die von mir vorgelegte Dissertation ist von Prof. Dr. Andreas Eckart betreut worden.

Köln, 18. 04. 2008

Teilpublikationen

Mužić, K., Schödel, R., Eckart, A., Meyer, L., & Zensus, A.:
"IRS 13N: a new comoving group of sources at the Galactic Center", Astronomy & Astrophysics, 482, 173, 2008

Mužić, K., Eckart, A., Schödel, R., Meyer, L. & Zensus, A.:
"First proper motions of thin dust filaments at the Galactic Center", Astronomy & Astrophysics, 469, 993, 2007

Mužić, K., Eckart, A., Schödel, R., Meyer, L., & Zensus, A.:

"Proper motions of thin filaments at the Galactic Center", Proceedings of IAU Symposium No. 238, Cambridge University Press, pp. 415, 2007

Mužić, K., Eckart, A., Schödel, R., Meyer, L., & Zensus, A.:
"Thin filaments at the Galactic Center: identification and proper motions", JoP: Conf. Series, Volume 54, Issue 1, pp. 311, 2006

Weitere Publikationen

Eckart, A., Baganoff, F. K., Zamaninasab, M., Morris, M., Schödel, R., Meyer, L., **Mužić, K.**, Bautz, M. W., Brandt, W. N., Garmire, G. P., Ricker, G, R., Kunneriath, D., Straubmeier, C., Duschl, W., Dovciak, M., Karas, V., Markoff, S., Najarro, F., Mauerhan, J., Moultaka, J., & Zensus, A.:
"Polarized NIR and X-ray Flares from Sgr A"*, Astronomy & Astrophysics, 479, 625, 2008

Perger, M., Moultaka, J., Eckart, A., Viehmann, T., Schödel, R. & **Mužić, K.**:
"Compact mid-IR sources east of Galactic Center source IRS5", Astronomy & Astrophysics, 478, 127, 2008 Schödel, R., Eckart, **Mužić, K.**, Meyer, L., Viehmann, T., & Bower, G. C.:
"The possibility of detecting Sagittarius A at 8.6 μm from sensitive imaging of the Galactic Center"*, Astronomy & Astrophysics, 462, L1, 2007

Meyer, L., Eckart, A., Schödel, R., Duschl, W. J., **Mužić, K.**, Dovciak, M. & Karas, V.:
"Near-infrared polarimetry setting constraints on the orbiting spot model for Sgr A flares"*, Astronomy & Astrophysics, 460, 15, 2006

Eckart, A., Schödel, R., Meyer, L., Trippe, S., Ott, T., Genzel, R., **Mužić, K.**, Moultaka, J., Straubmeier, C., Baganoff, F. K., Morris, M., & Bower, G. C.:
"Multi-wavelength and polarimetric observations of Sagittarius A"*, JoP: Conf. Series, Volume 54, Issue 1, pp. 391, 2006

Eckart, A., Schödel, R., Straubmeier, C., Bertram, T., Pott, J.-U., **Mužić, K.**, Meyer, L., Moultaka, J., Viehmann, T., Rost, S., & Herbst, T.:

"Interferometric observations of the Galactic Center: LBT and VLTI", Advances in Stellar Interferometry, Proceedings of the SPIE, Volume 6268, pp. 62681J, 2006

Eckart, A., Schödel, R., Meyer, L., **Mužić, K.**, Pott, J., Moultaka, J., Straubmeier, C., Dovciak, M., Karas, V., Genzel, R., Ott, T., Trippe, S., Najarro, F., Morris, M, & Baganoff, F.:
"The Galactic Centre: The Flare Activity of Sgr A and High-Resolution Explorations of Dusty Stars"*, ESO Messenger, volume 125, pp. 2, 2006